The University of Maine

DigitalCommons@UMaine

Electronic Theses and Dissertations

Fogler Library

Spring 5-5-2023

Efficient Sintering of Lunar Soil using Concentrated Sunlight

Diprajit Biswas
University of Maine, diprajit.biswas@maine.edu

Follow this and additional works at: https://digitalcommons.library.umaine.edu/etd

Part of the Ceramic Materials Commons, Energy Systems Commons, Heat Transfer, Combustion Commons, Manufacturing Commons, Structural Engineering Commons, Structural Materials Commons, Thermodynamics Commons, and the Transport Phenomena Commons

EFFICIENT SINTERING OF LUNAR SOIL USING CONCENTRATED SUNLIGHT

By

Diprajit Biswas

B.S. Ahsanullah University of Science and Technology, 2018

A THESIS

Submitted in Partial Fulfillment of the

Requirements for the Degree of

Master of Science

(in Mechanical Engineering)

The Graduate School

The University of Maine

May 2023

Advisory Committee:

Justin Lapp, Assistant Professor of Mechanical Engineering, Advisor

Richard Kimball, Professor of Mechanical Engineering

Bashir Khoda, Associate Professor of Mechanical Engineering

EFFICIENT SINTERING OF LUNAR SOIL USING CONCENTRATED SUNLIGHT

By Diprajit Biswas

Thesis Advisor: Dr. Justin Lapp

Construction material is one crucial need for long-term habitation on the moon. When concentrated for high heat flux, solar radiation can heat lunar soil or regolith until it sinters at temperatures above 900°C. The solid, sintered soil simulant can be used as construction material. This work explores the conditions leading to effective lunar soil sintering for both direct and indirect irradiated sintering. Lunar soil simulants were sintered using concentrated light from a xenon-arc lamp with varying heat flux intensity. During direct sintering of LHS-1, a sintering range of 860°C-1140°C corresponding to a peak heat flux of 105-120 kW/m^2 was identified which sinters a 4 mm thick lunar brick. A higher heat flux of up to 225.6 kW/m^2 has been experimented with, which melts the top surface of the simulant, but an 8 mm thick lunar brick is achieved. Different direct sintering techniques are experimented with to sinter thick and large lunar soil bricks. A time series experiment is conducted taking LHS-1 and JSC-1A lunar soil simulant to find the sintered mass at different experiment duration. Comparative sintering behavior of LHS-1 and JSC-1A lunar soil simulant is also studied. One exciting thing is the central thickness for JSC-1A is initially higher, but with time, the central thickness of LHS-1 surpasses the central thickness of JSC-1A. Indirect sintering with silicon carbide (SiC) plate is studied by varying input irradiation, which sintered similar thick LHS-1 lunar soil brick without melting at higher irradiation. Indirect sintering increases the size as well. It provides

possibility to sinter different shaped lunar bricks using molds. Limited compressive strength data showed higher strength for indirect sintering. Special indirect sintering experiments were conducted to reach the sintering temperature faster with higher incoming irradiation, which reduces processing time. A thermodynamic analysis is also conducted for a closed system furnace to sinter lunar soil and extract byproduct water for oxygen production. The study shows that 0.35 gm of oxygen can be produced from 1 kg of LHS-1 lunar soil simulant, with a hydrogen mole to oxygen mole ratio of four at 2000°C system temperature. The thermodynamic analysis considers all the energy input and output to find the required solar energy to raise the system temperature at a particular operational temperature to sinter lunar soil. It gives a future to develop a model furnace to run the sintering operation at the moon.

DEDICATION

To my parents, my brother, and my teachers, who are the reason behind where I am today.

ACKNOWLEDGEMENTS

I'd like to thank my supervisor, Dr. Lapp, for his help and support. It would not have been possible to finish this thesis without his invaluable constructive criticism and guidance. I would also like to thank my colleagues, Angel Loredo, Thomas Cox, and Alireza Kianimoqadam, for their help throughout my research.

TABLE OF CONTENTS

LIST OF TABLES

LIST OF FIGURES

NOMENCLATURE

Q_{solar} = Solar irradiation

E_{solar} = Solar energy

Q_{rerad} = Radiated heat through aperture

E_{rerad} = Radiated energy through aperture

Q_b = Heat loss through boundary wall

E_b = Energy loss through boundary wall

E_{LS} = Energy entered the system with lunar soil simulant

$E_{H2,in}$ = Energy entered the system with hydrogen

E_{H2O} = Energy leaving the system with water

$E_{H2,out}$ = Energy leaving the system with hydrogen

E_{SLS} = Energy of sintered lunar soil simulant leaving the system

E_{SLS} = Energy of ilmenite reduction reaction

I = Solar flux on the lunar surface

C = Concentration Ratio

A_b = Area of the system boundary

A_{ap} = Area of aperture

T_a = Ambient Temperature

T_b = Temperature of the system boundary

T_s = Temperature of the system

n_{LS} = Moles of lunar soil simulant

n_{H2} = Moles of hydrogen

n_{H2O} = Moles of water

n_{IL} = Moles of ilmenite reacted

$\bar{h}_{LS}$ = Specific enthalpy of Lunar soil simulant

$\bar{h}_{H2}$ = Specific enthalpy of hydrogen

$\bar{h}_{H2O}$ = Specific enthalpy of water

$\bar{h}_{react}$ = Enthalpy of ilmenite reduction

Δt = experiment duration

R_c = Insulator's conduction resistance

K = Insulator's heat conductivity

X = Boundary wall thickness

ε_i = Emissivity of the insulating material

R_r = Resistance of irradiation

Q_r = Radiation heat loss from the boundary wall

R_t = Total boundary insulation

M = Mass of lunar soil simulant

C_p = Specific heat of lunar soil simulant

ξ = moles of hydrogen atoms/moles of oxygen atoms

σ = Stefan–Boltzmann constant = 5.6703×10^{-8} (W/m^{2}K^4)

CHAPTER 1

INTRODUCTION

Humans are always curious to learn about outer space. The nearest space object is the moon, formed through a giant impact between the proto-earth and Theia, a mars-sized impactor [1]–[3]. Exploring the moon will provide scientists with new views of early Earth and how the Earth-Moon and solar systems formed and evolved. The role of asteroid impacts in influencing Earth's history and possible future lunar exploration can be studied. Lunar soil simulant, the delicate, abrasive particulate material that makes up the immediate surface of the moon, has a significant impact on lunar exploration. At elevated temperatures and for applications in space environments, it is a potential candidate for in-situ resource utilization (ISRU) which means collecting, processing and using the present resources at lunar environment to replace earth's resources for exploration. Since scientists are trying to find new ways to explore outer space, techniques of ISRU, like utilizing the lunar soil simulant, are convenient and economical because of the availability of lunar soil simulant at lunar surface and reduction of transportation cost of the raw materials. Lunar soil can be harnessed in various ways to provide materials and products necessary for long-duration human exploration of the moon. This lunar soil is resistant to cosmic ray irradiation and corrosion and is thermally stable over a range of temperatures from near-absolute-zero to several hundred degrees Celsius [4]. The lunar soil can serve as a feedstock for many essential supplies for human exploration on the moon [5]. It contains water and other low-temperature volatiles. When heated to high temperatures, metal oxides, which make up most of the lunar soil, can be separated to retrieve oxygen, aluminum, iron, and other metals. Finally, the lunar soil can be sintered or melted at high temperatures to form solid structures for construction materials. These ISRU techniques are convenient and economical by reducing the mass necessary to transport from Earth.

1.1. Necessity to Produce Sintered Lunar Bricks

Concentrated sunlight can reliably heat materials above the necessary sintering temperature and represents an effective means of directly harnessing the only readily available energy source on the moon. Since lunar space has plenty of lunar soil and solar power, lunar soil can be sintered with solar energy by concentrating solar irradiation to achieve required sintering temperature to make lunar brick. Sintered construction material from lunar soil has been suggested for several functions. The sintered lunar soil will form construction material which can be used to construct solid surfaces, berms, and other structures. The formed lunar bricks can be utilized to make space stations for lunar landings and launching. Due to less gravity on the lunar surface, lunar soil takes longer compared to earth to settle down, which can spoil mechanical interfaces and can easily penetrate through space suits. Sintering lunar soil would mitigate free-flowing lunar soil and reduce the disturbance to astronauts [6]. Arrangements made with sintered lunar soil will also protect astronauts from dangerous solar radiation in the vacuum environment [7]. Construction materials developed by sintering of lunar soil can further space research to flourish. This method is advantageous and economical to launch additional space exploratory vehicles from the lunar base. Spaceships will require less energy to escape lunar gravitational field because it is 1/6th times of earth's gravitational field. Also, they do not have to travel the distance from earth to moon which will reduce the cost of travel. Therefore, space stations constructed with sintered lunar soil at lunar surface will save lots of energy and expense [8]. Hence, the best solution is to utilize the in-situ resources to produce the required construction materials for a sustainable lunar exploration platform to support human habitation and to create further space research facilities [9], [10]. Cost-effective ISRU-produced dust protection and structural materials will enable permanent stations on the lunar surface to be used as a launching point for further exploration [8]–[10].

1.2. Production of Construction Materials and Oxygen from the Same Process

Oxygen is another essential material available on the lunar surface in metallic oxides for space missions. Astronauts use oxygen to oxidize the fuel in spaceships and for inhalation. However, the transportation cost is very high from earth to the moon, which varies between 3000$ to 55000$/kg [11]. That is why it would be beneficial to produce oxygen from the existing materials on the moon by ISRU technology. Since lunar soil is mainly mixed with metallic oxides, oxygen can be extracted from these oxygen-concentrated compounds as a byproduct during sintering and metal or alloy extraction [12]–[18]. Both the construction material and oxygen can be extracted from the same lunar soil simultaneously from a single process which will be economical [18]. Oxygen reduction requires a high temperature (800-1000°C) to break the oxide components and large amounts of energy are needed to heat the lunar soil from ambient to 800°C. The lunar soil can be sintered using solar energy at this temperature to make solid construction materials, and oxygen can be extracted from the same process. A given quantity of oxygen and sintered material can be produced with far less energy by heating the lunar soil once rather than heating two separate masses of lunar soil in individual processes. At high temperatures during the sintering of lunar soil in a hydrogen atmosphere, water is released as a byproduct of the process, which can be electrolyzed to produce oxygen for further use [14].

1.3. Fundamental Processes of Sintering

The sintering process is a thermal process through which particles of material, heated to below the bulk melting temperature, are bonded through surface diffusion and constituent melting to form a coherent, typically porous solid object of improved strength through mass transport [19], [20]. It is one of the ancient processes of achieving strengthened material where the powder particles are bonded below the bulk melting temperature through diffusion and different atomic transport mechanisms [21]. On a microstructural scale, sinter bonding is

evident as cohesive necks grow between contacting particles. Smaller particles have high surface areas and more energy per unit volume, called surface energy, which promotes faster sintering. The grain boundaries, important to atomic motion, are defective regions with high atomic mobility. For many materials, the preferred path for atomic transport during sintering is along the grain boundaries through grain boundary diffusion. Other active mass transport mechanisms include flow over free surfaces and through the crystal lattice, vapor transport, plastic flow, viscous flow, and dislocation climb. All particles have an inherent driving force for mass flow, termed the sintering stress, estimated from the surface energy divided by the particle size. The sintering stress is more significant with smaller particles, and the atomic mobility increases with higher temperatures [19]. For sintering, temperature and time variables of are highly influential, whereas pressure, atmosphere, heating, and cooling rate have comparatively lower influences [21], [22]. The rate of the sintering mechanism generally increases with the increased temperature [23]. The particle shape, size, distribution as well as fineness of particles also strongly influence the sintering mechanism. In addition, if the density of the compacted powder is high, the contact area between the particles will become high, which makes the bonding process more efficient [22].

1.4. Typical Methods of Sintering

Several methods for sintering exist, including some which have been applied to simulants of lunar soil. Some of them are discussed below.

1.4.1. Selective Laser Sintering

Selective laser sintering is one of the most prominent technologies, where a directed laser beam melts powdered metal particles to form complex 3D parts layer by layer. Here the sintering temperature increases significantly with the increased laser power[24]. During consecutive melting and re-solidification, the energy transport is strongly influenced by the melting front's propagation [25]. Sintering also can be done layer by layer, where the loose

powder is sintered on top of a sintered layer. A significant density change occurs with increasing temperature, which causes the top layer to mesh with the bottom one. By sintering the top layer's loose powder entirely with a combination of different processing parameters, it can be joined with the existing layer where the thickness of the top loose powder layer has a significant effect [26]. Since the melted powder grains stick to each other via surface tension forces, forming a series of spheres with diameters approximately equal to the diameter of the laser beam is known as balling phenomenon. To overcome this, another material with a significantly different melting point needs to be mixed with lunar soil, which is not economical [24], [25].

1.4.2. Microwave Sintering

Microwave sintering is used mainly for ceramics, where the specimen materials interact with the microwaves to heat at a very high heating rate. Since microwave heating does not rely entirely on thermal conductivity, the energy produced by the microwave source can be wholly spent on heating the subject without heating the insulation and air in the furnace. Within the material, the electromagnetic energy converts into heat energy, which takes the material to a sintering temperature to sinter. Here the sintered product improves in quality compared to conventional sintering processes [27], [28]. In some advanced cases, an injection molding technique is used to shape the material before sintering with microwaves [29], [30]. A high temperature is required to sinter the soil to create a solid part from lunar soil particles. Microwave sintering is used extensively to sinter lunar soil [9], [10], [31], [32]. Lunar soil can be sintered using a normal kitchen-type microwave. Here, the major problem is to measure the exact temperature of the sintering process. Microwave heating also generates a high-temperature gradient and creates micro-cracks inside sintered part. The complicated dielectric properties of lunar soil, which change with varying temperature, reduces the efficiency of the heating process[33]. In addition, the penetration depth of different microwave frequencies and

variation in lunar soil composition makes the sintering process uncertain [33]. Furthermore, the pre-formation of blocks is necessary to give a shape which requires extra work and energy [34]. Some materials, like titanium powder, interact weakly with microwaves, so they are unable to be heated effectively to reach the sintering temperature [28]. Therefore, this technique is ineffective in properly sintering titanium-contained lunar soil specimens.

1.4.3. Spark Plasma Sintering

Spark plasma sintering is a pressure-assisted low-voltage DC pulsed current-activated rapid sintering technique [35]. In this process, the heating rate exceeds 100°C/min. Spark discharge through the combined effect of external fields such as force and electricity could activate the particles to improve densification [36]–[38]. The applied pressure to the surface during sintering contributes to the diffusion rate, enhances phase transformation and homogeneity, and increases the sintered material's strength about ten times that of typical plain concrete [4]. This technique is mostly used for extremely refractory materials, metastable phases or dense nanostructured materials, non-equilibrium or functionally graded alloys, and composites that are hard to sinter [35], [39]. Higher sintering temperature generates high-density solid materials by gradually eliminating pores between grains by enhancing necking and diffusion between particles, improving the mechanical properties and particle packing density [40]. Hybrid spark plasma sintering, combined with an additional resistance or inductive heating, provides a homogeneous heat distribution within and across the material during sintering. The advantages are- high relative density, improved hardness, and microstructures compared to other sintering techniques[41], [42]. During SPS, rapid contraction occurs for rapid and non-uniform heating/cooling, which increases significant internal stresses to form intergranular cracks and fragmentation of sintered solids [43]. This uneven temperature distribution thus affects the uniform microstructure and properties of the material [41], [42]. During SPS, pressure can substantially lower the sintering temperature for

lunar soil, and the density of sintered lunar soil can be increased by increasing the sintering temperature [4], [33]. Since SPS is a water-free and rapid sintering process, it is a promising technique for space applications. The effect of SPS conditions on lunar soil, sintering process, microstructure evolution, phase transformation, and mechanical properties still needs to be studied well, which is required for successful space application [4].

1.4.4. Sintering through Extrusion 3D Printing

Additive manufacturing is a well-established method extensively used in research and manufacturing. Through additive manufacturing, lunar soil can be 3D printed. Liquid inks containing lunar soil are used for direct extrusion 3D printing. Though the ink is liquid, it can be 3D-printed rapidly by following a pre-defined architecture where it can withstand different extrusion pressure during printing through different diameter nozzles [44]. Sometimes the printed material is sintered in a hydrogen atmosphere where the material becomes tougher but does not gain any increased peak strength. But sintering in the hydrogen atmosphere assists in extracting oxygen from lunar soil during sintering [45]. The energy required to fuse the lunar soil for ink could be harnessed from solar power, a promising alternative to the laser melting process [8].

1.5. Utilizing Concentrated Solar Power for Sintering

It is noted that the prior methods primarily use electrical energy for sintering which is not available on the moon. Solar energy is the only source of energy there. Solar energy can be used with PV panels or through concentration of solar radiation. Concentrating solar power is more efficient in reaching the desired high temperature to sinter lunar soil. In some methods, like the 3D-printing process, an additive is required to give proper shape before sintering [6]. These are not economical in sintering lunar soil on the moon, taking additives from the earth, or using instruments to generate electricity. So, there is a vast scope for updating the technology to make it economical and straightforward to install concentrated solar stations for sintering

lunar soil. Using concentrated solar power, the temperature can rise in the sintering range to make construction materials using in-situ lunar sand, which will minimize the transportation cost and amount of resources from the earth [7]. In addition, electrical energy, stored from solar energy, can be used to operate the assisting mechanism, and run the whole process. A layer of lunar soil can be printed through additive manufacturing technology, also known as 3D printing. Through a high flux solar furnace, the concentrated light can be focused upon the printed layer to sinter the material after printing each layer. The strength of the sintered material is improved by reducing the thermal gradient and reducing the cooling time between the sintering of successive layers. But for concentrated solar light, the sintered layer becomes inhomogeneous due to fluctuations of flux density. A steady flux can be achieved using xenon light, which can be used for sintering without any change of energy, leading to a uniform layer-by-layer sintering of lunar soil. However, there is a weak layer-to-layer bond with high porosity level, which causes a much lower compressive strength for actual application [6]. Therefore, improved technology is required to use concentrated solar power uniformly to form a strengthened material for lunar application purposes.

Using concentrated solar energy as the source of heat helps avoid a low-efficiency energy conversion step and transportation of bulky equipment. Through concentration, solar radiation can raise the lunar soil temperature well into the sintering range to make construction materials [7]. Solar energy has been applied to demonstrate the sintering of lunar soil in several examples. Sperl et al. (2018) performed the sintering of lunar soil simulants using concentrated light from a xenon-arc lamp and a moving bed to demonstrate the 3D printing of sintered structures. It was found that the layer bond was weak, leading to lower compressive strength in multi-layer parts [6]. A possible explanation is a need for more understanding of the sintering depth for specific process parameters. Similar experiments were performed by Fateri et al. with lunar soil supplied continuously through a feeder during the 3D printing proc [46]. Urbina et

al. conducted sintering experiments in a similar manner [47]. Imhof et al. developed technologies for the fabrication of "building block" elements by solar sintering of lunar soil. The technology was demonstrated using concentrated sunlight in a solar furnace [7]. Using a steady flux from simulated sunlight leads to a uniform layer-by-layer sintering of lunar soil. To make construction-size bricks, the thickness of each layer of the sintered piece is essential to the time and energy requirements for fabrication.

Solar sintering has also been applied in several studies to sinter the lunar soil directly on the lunar surface to fabricate landing pads or roads. Experimental demonstrations were performed by simulating a mobile solar concentrator to heat a lunar soil simulant (JSC-1A) bed. With stationary focus, the sintering depth reached 6 mm, while only 2 mm was reached when the focal point was rastered across the bed. In both cases, the top surface was melted, and the authors noted the need for deeper sintering and more control to avoid melting [48]. Experiments using an optical fiber-based solar concentrator were used to demonstrate surface stabilization by sintering a 15 in by 15 in single layer pad [49]. Understanding the conditions and time to sinter to a specific depth is critical for this application.

Structural materials from lunar soil may be efficiently produced with concentrated sunlight. Still, the exact conditions leading to robust, high-quality parts need to be clarified from the limited number of demonstrations of solar sintering of lunar soil. The present study aims to describe the range of thermal conditions which should be targeted to sinter lunar soil and how variations in those parameters affect the sintering depth and compressive strength of the resulting material. An experimental campaign was performed, focusing on producing and testing small-scale samples at various thermal conditions.

The goal of the research is to sinter highly nonconductive lunar soil with Concentrated Solar Power (CSP) to find optimal heating condition for different sintering approach. Another direction is to analyze the prospects of extracting oxygen during sintering operation from the

biproduct water during sintering reaction between the compounds of lunar soil and hydrogen. Processes will be discussed to combine sintering and oxygen extraction, to determine the exact conditions of the sintering and the right conditions to run a reactor for oxygen extraction. The energy transfer of the whole process will also be addressed. The thermal analysis will include the energy balance and the heating condition based on different parameters like input energy, radiation level, operational time etc.

CHAPTER 2

EXPERIMENTAL METHODS

NASA's Artemis plan is currently focused on developing a long-duration habitat at the lunar south pole. The goal is to utilize in-situ resources to build a lunar foundation habitation module and power systems to support more extended expeditions on the lunar surface [50]. The objective of the experiments is to sinter lunar soil with Concentrated Solar Power (CSP) for building lunar bricks of high strength. The physical parameters and radiation conditions that will cause lunar soil to sinter using CSP were found. The radiation level was varied by changing the energy supplied and the distance between the lunar soil simulant's top surface and the energy source. An appropriate heating condition was found to reduce the required time to sinter the lunar soil without melting, maintaining a constant temperature. Experiments were conducted to find ways to sinter lunar soil into larger pieces by direct and indirect heating. Different heating conditions by changing heating parameters was studied experimentally to find an appropriate combination of parameters, heat flux, temperature, time, etc., for a large and thick sintered lunar brick.

2.1. Material Used

Since NASA's Artemis plan is based on the lunar south pole, primarily surrounded by highlands regions, LHS-1 Lunar Highlands Simulant is mainly used in most experiments. The Exolith Lab has developed the LHS-1 at the University of Central Florida to provide a chemical and particle size analog to Apollo samples taken from lunar highlands regions. The simulant is made from 74.4% anorthosite, 24.7% glass-rich basalt, 0.4% ilmenite, 0.3% pyroxene, and 0.2% olivine, by weight [51]. Bulk chemistry is primarily silicon oxide, aluminum oxide, and calcium oxide.

NASA Johnson Space Center developed a new lunar soil simulant named JSC-1A with similar bulk chemistry to Apollo 14 soil 14163[52] and Apollo 17 [53]. JSC-1A is mined from

the volcanic ash of basaltic composition with geochemical and physical properties within the ranges of lunar mare soil samples [52]. The chemical composition and mineralogy are similar to Apollo 14 soil 14164 with equal particle size distribution to Apollo 15 soil 1553 [54]. It contains 49.3% glass, 37.1% plagioclase, 9.0 % olivine, 1.1% Cr-spinel, and some other minerals [55].

Table 2.1. Comparative properties of LHS-1 and JSC-1A lunar soil simulants

Property	LHS-1	JSC-1A
Bulk Density (g/cm^3)	1.30 [51]	1.5-1.7 [52]
Void Ratio	1.477 [56]	0.61-1.18 [57]
Porosity (%)	59.6 [56]	30.9 – 46.7 [58]
Particle size (µm)	<0.04 – 1000 [51]	10-1000 [58]
Angle of Repose	39.58° [59]	37° [60]
Cohesion (kPa)	0.311 [61]	0.2-1.8 [57]
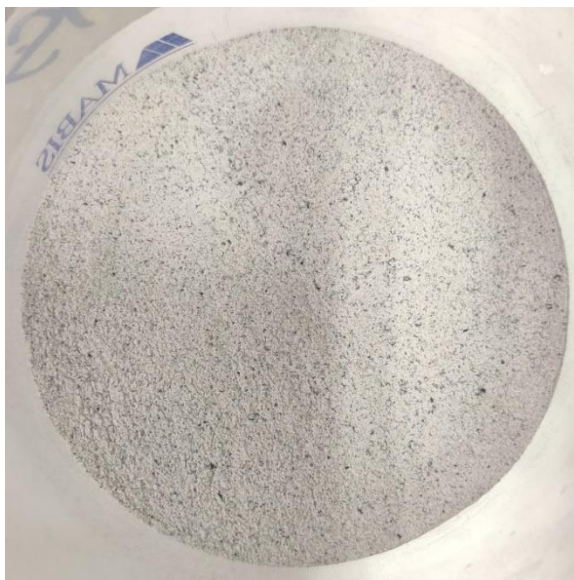
(A)   (B)

Figure 2.1. (A) LHS-1 and (B) JSC-1A lunar soil simulants

Both the simulants were used for some experiments to find comparative performance between LHS-1 and JSC-1A. Some properties of both the lunar soil simulants are listed in Table 2.1.

Table 2.2. Bulk chemistry of LHS-1 and JSC-1A lunar soil simulants

Serial	Oxides	LHS-1 (wt.%)	JSC-1A (wt.%)	Melting Point (°C)
1.	SiO_2	51.20	47.4	1713
2.	TiO_2	0.60	1.56	1855
3.	Al_2O_3	26.60	16.10	2030
4.	Fe_2O_3	-	11.40	1565
5.	FeO	2.70	-	1377
6.	MgO	1.60	7.72	2800
7.	CaO	12.80	10.50	2613
8.	Na_2O	2.90	2.94	1275
9.	K_2O	0.50	0.80	740
10.	MnO	0.10	0.18	1840
11.	P_2O_5	0.10	0.59	562
12.	Cr_2O_3	-	0.03	2435
Total		99	99.60	-

Table 2.2 represents the bulk chemistry of LHS-1 [51] and JSC-1A [52], [62] along with the melting temperature of each element. Total wt.% is less than 100%, considering loss on ignition and excluding volatiles and trace elements. Both contains high amount of silica. Amount of titanium dioxide is three times for JSC-1A compared to LHS-1 simulant. Another noticeable difference is- LHS-1 contains ferrous oxide but JSC-1A does not and JSC-1A contains ferric oxide while KHS-1 does not. Fig. 2.1 shows both the simulants where JSC-1A is relatively darker due to the presence of decent percentage of ferric oxide in it. .

2.2. Experimental Setup

For controlled sintering experiments, an apparatus was constructed to expose samples of lunar soil simulant to simulated concentrated sunlight. Light emits from a 7-kW xenon-arc lamp placed at focus of an elliptical reflector with a focal length of 825 mm. The assembly model is Proyecson Xenoluxe XL-7000. The xenon arc lamp produces light similar to the spectrum of the sun, and the lamp current can be adjusted from 60 to 200 A by manual control. The light be concentrated and directed to the surface of an insulated crucible filled with lunar soil simulant. The concentrated thermal radiation level can be varied by changing the arc lamp's current or the crucible's position relative to the focus of the concentrated light. An image of the experimental apparatus is shown in Fig. 2.2.

A test frame holds a flat reflector and the crucible base at easily referenced positions relative to the solar simulator. The flat glass reflector is placed at 45° relative to the oncoming solar radiation to direct it vertically onto the crucible. Two fans are incorporated into the test stand to cool the reflector during experiments. The frame has index marks to measure the distance between the focal point and the crucible. The cylindrical crucible is made from a non-combustible, high-temperature calcium silicate insulation board to ensure unidimensional heat transfer and low heat loss from the particles through the side wall of the crucible. The outer radius of the crucible is 90 mm, and the height is 50.8 mm. The inner cylinder inside the

crucible, where the simulant will be poured, is of a radius of 30 mm and a depth of 26 mm. The cylindrical cavity of the crucible holds about 30 g of simulant.
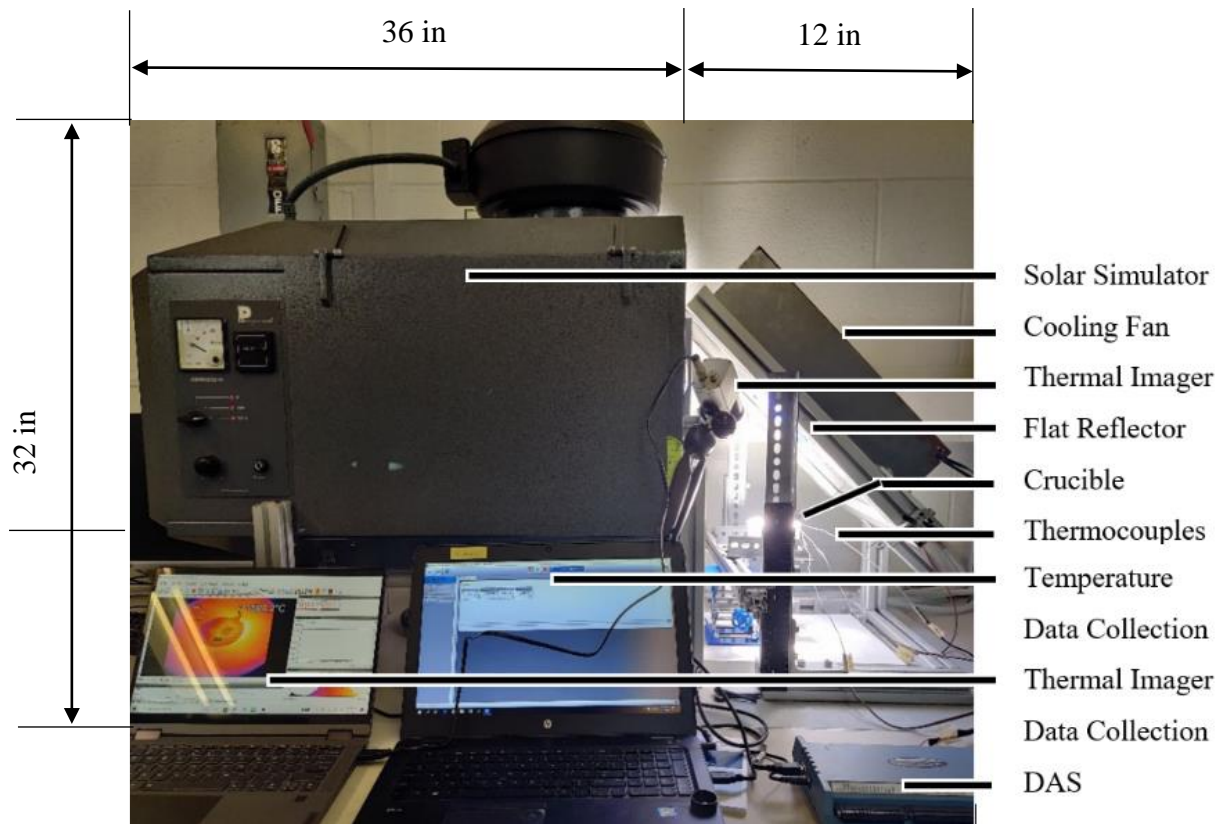
Figure 2.2. Experimental setup for sintering experiments

A thermal imager (Optris PI 1M) measures the top layer temperature of the simulant during the experiment. The temperature range of the thermal imager is 450°C - 1800°C. Three K-type thermocouples are fixed to the crucible and placed with junctions in the simulant. The three thermocouples are all along the central axis of the crucible, at 2 mm, 4 mm, and 6 mm below the top surface, and connected with a data acquisition system (DAS). At each vertical crucible height, a representative heat flux measurement is made by placing a 3 mm x 3 mm piece of silicon carbide (SiC) at the center of the flux distribution. It is heated until steady state, and the thermal imager measures the temperature. Modeling this as the stagnation temperature at the peak flux of the distribution and assuming the SiC is a gray surface, the heat flux is calculated. A computer record data from the thermocouples through the DAS and the thermal

imager separately. The thermal imager records 12 frames of images in each second, whereas the DAS is configured to save one data each second to the computer.

2.3. Experimental Procedure

Lunar soil simulant was weighed to 30 gm for each experiment and used to fill the crucible. Then the crucible was placed on the crucible holder of the test stand and adjusted to a pre-determined position relative to the reflector's focal point. The three thermocouples were secured inside the lunar soil simulant through the crucible sidewall. The solar simulator was turned on. A shutter on the solar simulator enclosure was kept close for a short period to allow for lamp output to stabilize. Data collection of the thermocouples and thermal imager were started, and the shutter was opened instantly, signifying time zero of the experiment. The experiment proceeded with constant irradiation until a steady state temperature was reached. Fig. 2.3 shows an image of the simulant bed under direct irradiation.

Figure 2.3. LHS-1 bed of 30 mm radius under direct concentrated irradiation

Thermocouples provided continuous data throughout the experiment but were limited to positions well into the depth of the bed to avoid direct irradiation on the thermocouple. The maximum temperature of the simulant occurred at the surface, as the simulant is nearly opaque. A thermal imager was used to measure the top surface temperature of the simulant.

In some concepts of using solar thermal energy to make solid sintered parts, solar energy can be used to heat a mold or crucible from the outside while lunar soil is contained on the inside. Solar heat is transferred indirectly to the soil simulant. This may provide an advantage of final surface finish and complex geometry for the part, but also creates challenges of an additional heat transfer step and separating the sintered part from the material. The heat transfer limitation can be overcome by a highly thermally conductive material, such as SiC.
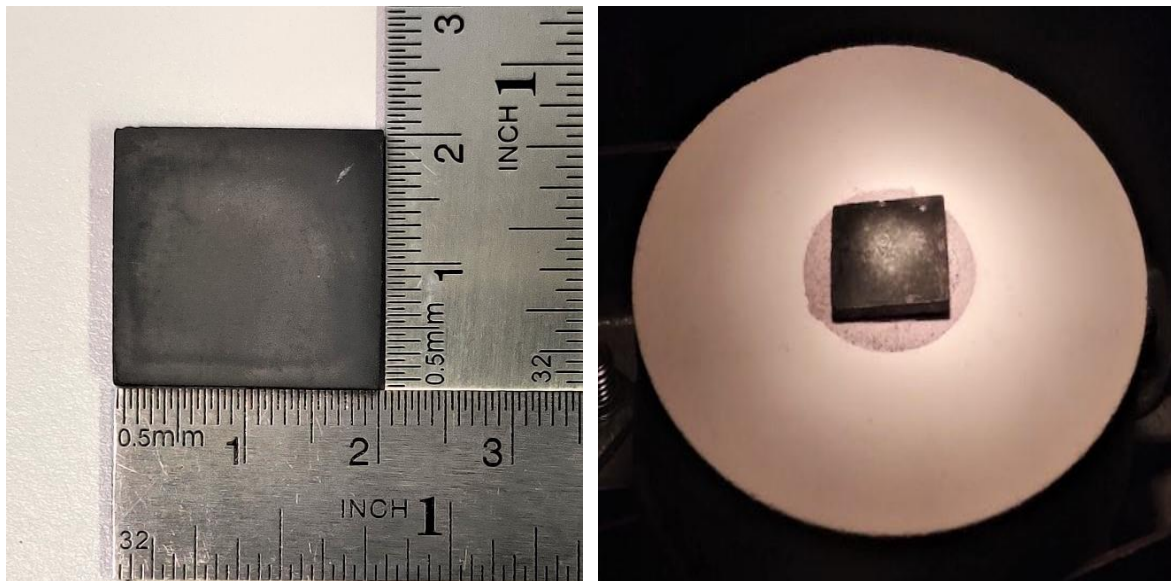
Figure 2.4. SiC plate and simulant under indirect irradiation

Indirect sintering experiments are conducted in a similar way to direct sintering, with a SiC plate placed over top of the particle bed, as shown in Fig. 2.4. The SiC is used as a heat transfer medium to transport heat uniformly throughout the lunar soil simulant surface touched with the SiC plate. In practice, this simulates the use of a solid mold for a sintered part heated by irradiating the outside of the mold. Thanks to its high thermal conductivity, the SiC diffuses the radiated heat more uniformly on the top surface of the lunar soil simulant bed. The size of

the SiC plate is 20 mm × 20 mm, and the thickness of the plate is 2 mm. Stanford Advanced Materials supplied the SiC plates, and manufacturer specifications list the material to have a thermal conductivity of 130 W/m.K at 25°C and an emissivity of 0.9. The circular crucible was filled the same way as direct sintering, and experiments proceeded following the same method.

A representative heat flux is measured at each vertical crucible height. The flux measurement is done without experimenting with lunar soil simulant. A solid calcium silicate disc of same height as the crucible is used instead of the lunar soil simulant at the center. A 3 mm x 3 mm piece of silicon carbide (SiC) is placed on top of the calcium silicate disc at the center of the flux distribution as shown in Fig. 2.5. It is heated until steady state, and the temperature is measured from the thermal imager.
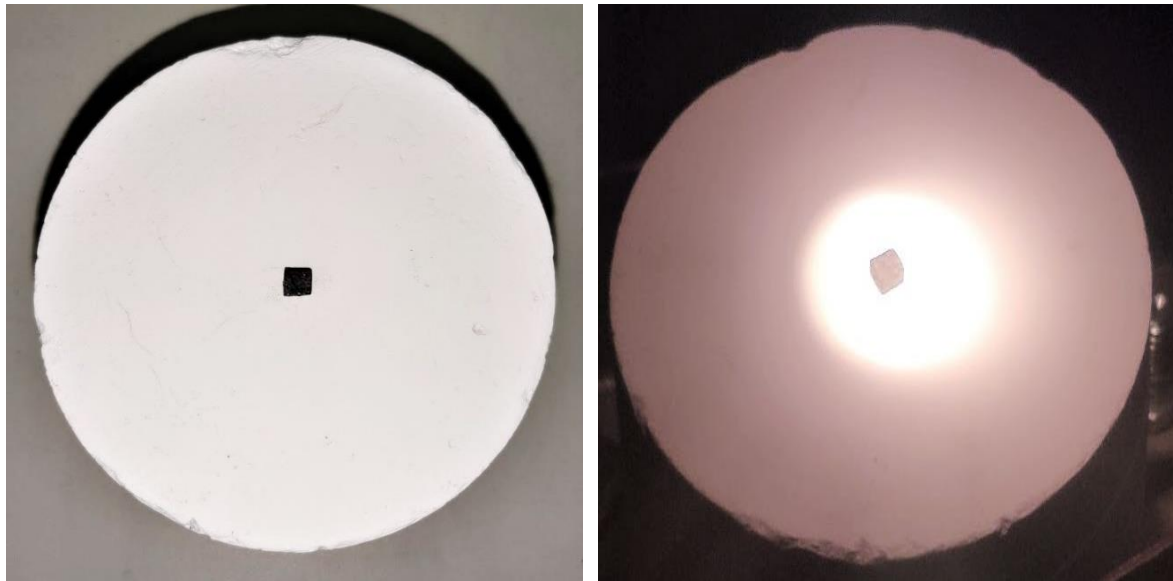
Figure 1.5. 3 mm × 3 mm piece of silicon carbide (SiC) plate

Thermal imager readings can only be taken in the absence of incident radiation. The procedure was to briefly close the solar simulator shutter, record a thermal video where each frame is of 1/12th second duration, then re-open the solar simulator shutter as shown with the sequence in Fig. 2.6.
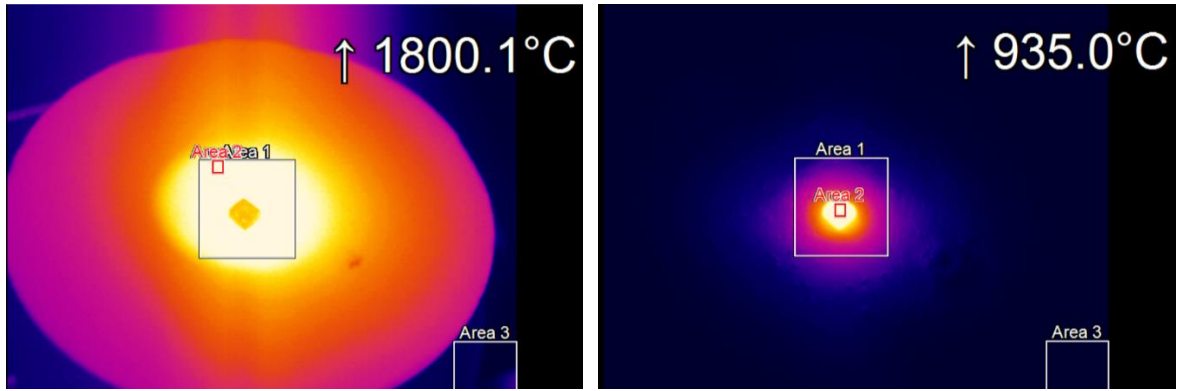
(A)   **(B)**

Figure 2.6. Thermal imager window when the shutter is (A) open and (B) close

This does have a small, temporary cooling effect on the simulant bed which changes the overall heating rate slightly, but it provides a reliable measure of maximum simulant temperature as experiments go to steady state. Thermal video data was recorded at times of 2, 4, 6, 8, 10, 15, 20, 25, 30, 35, and 40 minutes for directly irradiated experiments. Temperatures at these times from the thermal imager were taken from the maximum average temperature over a 3 mm square area of the SiC plate from thermal image maps. Modeling this as the stagnation temperature at the peak flux of the distribution and assuming the SiC is a gray surface, the heat flux was calculated with Stefan–Boltzmann equation.

$$q^* = \epsilon \sigma T^4$$

…………………………. (2.1)

Where emissivity of SiC plate, $\varepsilon = 0.9$ (from the manufacturer's manual) and Stefan–Boltzmann constant, $\sigma = 5.67 \times 10^{-8}$ W/m^{2}K^4.

CHAPTER 3

DIRECT SINTERING

3.1. Preliminary Experiments

Two approaches were taken to sinter the lunar soil simulant: direct and indirect. In direct sintering experiments, the concentrated sunlight was directed to the top surface of the lunar soil simulant for sintering without an intermediate heating medium. NASA's Artemis plan is based on the lunar south pole, primarily surrounded by highlands regions. Therefore, the direct sintering experiments were planned primarily with LHS-1 lunar soil simulant.
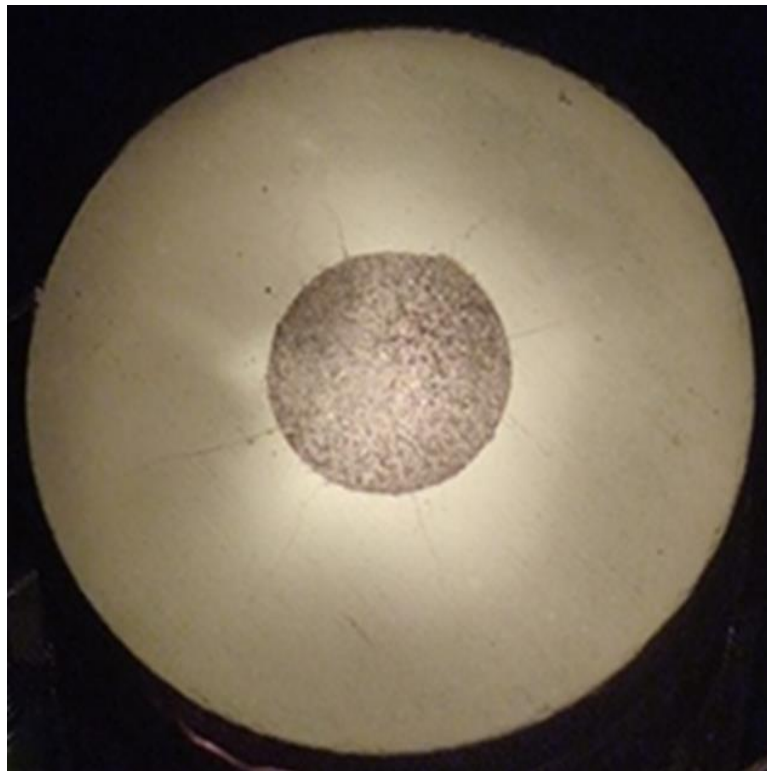
Figure 3.1. LHS-1 lunar soil simulant under direct irradiation

The first objective was to determine the experimental input current of the simulator and the distance between the focal point and the top surface of the lunar soil bed, which leads to sintering. After measuring 30 gm of LHS-1, the simulant was put inside the crucible and hand-pressed until all the simulant compactly packed inside. Then the crucible with the simulant was placed on the test stand. The simulator was turned on with an input current of 60 A, and the

shutter was opened. The mirror reflected the incoming irradiation from the solar simulator, and the top surface of the crucible and lunar soil simulant were irradiated. The irradiation was refocused at each distance to achieve concentrated irradiation by moving the lamp relative to the reflector, and the crucible was repositioned as required to direct the concentrated irradiation toward the center of the lunar soil simulant. Fig. 3.1 shows the lunar soil simulant under direct irradiation during the validation of the setup and experimental procedures.

In the experimental setup, the crucible holder is attached to the test stand. The crucible holder is vertically movable. The distance between the focal point of the incoming irradiation and the top surface of the lunar soil can be varied by moving the crucible holder vertically. Moving upwards reduces the distance, whereas moving downwards increases the distance between the focal point and the top surface. When the crucible holder was at the bottom of the test stand, the maximum distance between the top surface of the lunar soil simulant and the reflector focal point was measured as 173 mm. This is the maximum achievable distance for the experimental setup. The maximum temperature achieved on the top thermocouple at this distance was 736°C for 60 A current. After about 15 minutes, the temperature increased very slowly and came to steady state after about 20 minutes. In this case, no sintering occurred. Keeping the input current fixed at 60 A, the distance was reduced by 13 mm to 160 mm. In this case, no sintering occurred as before. No visible impact of temperature on the top surface of the lunar soil was noticed.

At 150 mm, a small black sintering point evolved at 650°C top thermocouple temperature. Since LHS-1 lunar soil simulant is a poor heat conductor and the top thermocouple is 2 mm beneath the top surface of the packed LHS-1, this measured temperature was lower than the top surface temperature. With time, the top surface temperature increased and went to a steady state along with the system, but the sintered mass did not increase. During the steady

state, the top thermocouple temperature was 794°C. At 140 mm, a similar black point was seen, and no visible impact of temperature on the top surface of the lunar soil simulant was noticed.
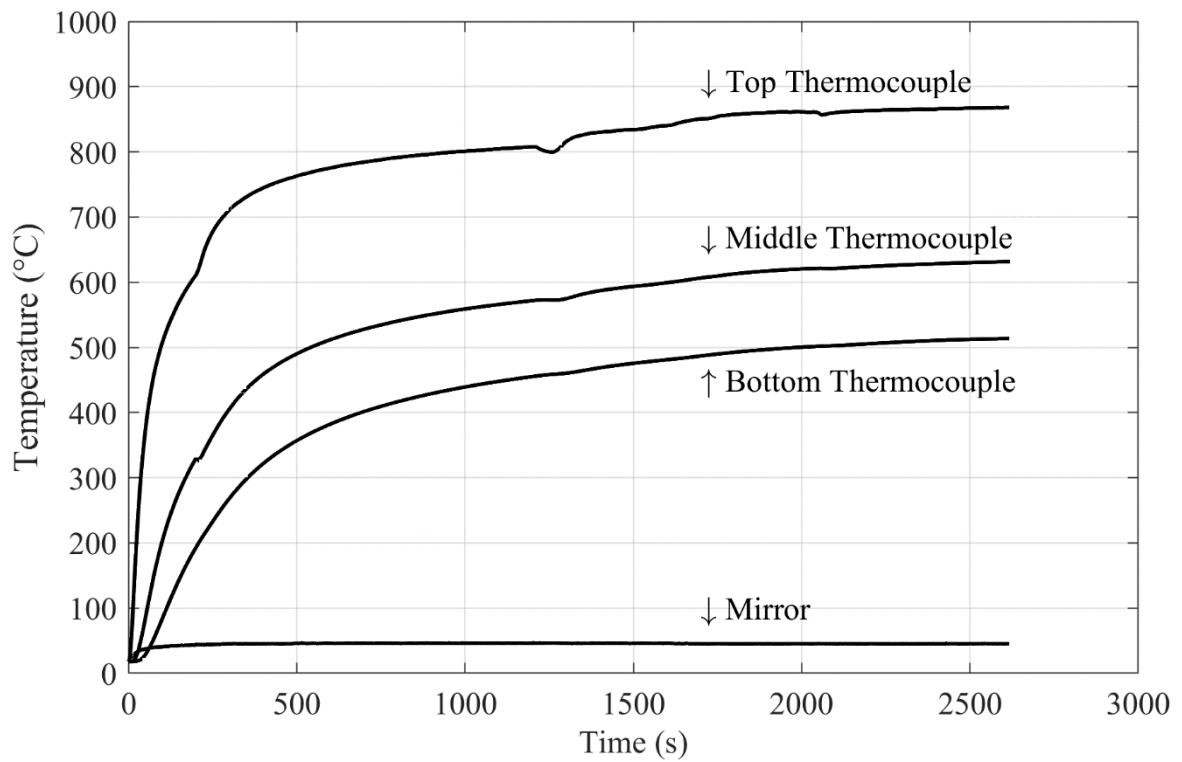
Figure 3.2. Temperature profile at 60 A current and 130 mm distance

Figure 3.3. Sintered LHS-1 on the simulant bed at 130 mm distance and 60 A current

At 130 mm distance, sintering started at 600°C top thermocouple temperature, and the system went to steady state at 868°C top thermocouple temperature. About 0.2 gm of sintered material was measured. Fig. 3.2 shows the temperature profile for all three thermocouples over time, including the mirror temperature and Fig. 3.3 shows the first sintered piece inside the simulant bed. Experiments between 130 mm and 80 mm were done for every 10 mm, and all resulted in sintered pieces of increased size, tabulated in Table 3.1.

At 80 mm distance, sintering started at 550°C top thermocouple temperature, and melting started at 800°C top thermocouple temperature for concentrated regions. The system came to a steady state at 1155°C top thermocouple temperature. The sintered/melted material was 1.4 gm. Fig. 3.4 shows the melted simulant under direct irradiation and the final product with a slight glacial zone formed due to melting. At this point, balling phenomena were noticed where the molten LHS-1 tended to create a canal to separate the melted part from the sintered part forming a ball. Creating the narrow channel, balling phenomena disturbed the uniformity of the top surface of the sintered part, separating the melted zone from the sintered zone.

Figure 3.4. Melted simulant at 80 mm distance and 60 A current

Figure 3.5. Melted lunar soil simulant and broken sintered part at 60 mm distance

At 70 mm distance, sintering started when the top thermocouple temperature was 500°C. With increased heat flux, the top surface began to sinter shortly after the experiment started. Since the heat conductivity of LHS-1 is very low, it takes time to heat the top thermocouple. Therefore, the temperature of the top thermocouple did not reflect the top surface temperature. Melting was noticed at 700°C top thermocouple temperature for the distributed flux, which came at a steady state at about 1100°C top thermocouple temperature. The maximum temperature rise for the concentrated region was 1202°C for the top thermocouple. The mass of sintered and melted material was 1.8 gm. The top thermocouple was attached to the sintered material after the experiment. At 60 mm distance, the values were taken only for the steady state temperature with distributed focus. At this distance concentrated irradiation was not experimented since it would cause more melting. In this distributed focus experiment, the mass of sintered and melted material was 2.3 gm. The top thermocouple went inside the sintered material and was attached during the experiment. It was challenging to separate the top thermocouple from the sintered piece, and the sintered material broke, as shown in Fig. 3.5.

Table 3.1. Direct sintering data of LHS-1 lunar soil simulant to find sintering condition with the variation of focus to obtain maximum irradiation at each distance

Distance (mm)	Sintering Temperature (°C)	Melting Temperature (°C)	Steady State Temperature (°C)	Time to Reach Steady State (min)	Sintered Mass (gm)
173	_	_	736.24	20:11.1	_
160	_	_	721.19	22:22.7	_
150	650.23	_	794.70	33:50.5	> 0
140	_	_	795.28	23:00.4	_
130	600.36	_	868.01	35:00.3	0.2
120	670.27	_	924.63	32:15.8	0.4
110	800.58	_	1027.56	39:53.3	0.4
100	600.86	_	989.01	30:32.3	0.9
90	600.74	_	1085.06	30:12.2	0.8
80	549.11	800.30	1155.05	30:16.2	1.4
70	500.94	700.48	1202.14	36:04.5	1.8
60	459.73	700.57	1193.72	33:01.5	2.3
50	651.23	1000.11	1260.32	31:40.5	2.1

At 50 mm distance, all the data were taken for a distributed flux. No significant melting happened because the light was well distributed over the lunar soil simulant top surface without a specific concentrated point. Sintered material found was 2.1 gm. During this experiment, to avoid melting, the light was distributed over a broad region of the simulant. It resulted in the sintering of a vast chunk of particles, but again the top thermocouple was attached to the sintered material. For this low distant position and for focusing over the whole top surface, the heat transfer and volume of the sintered material increased.
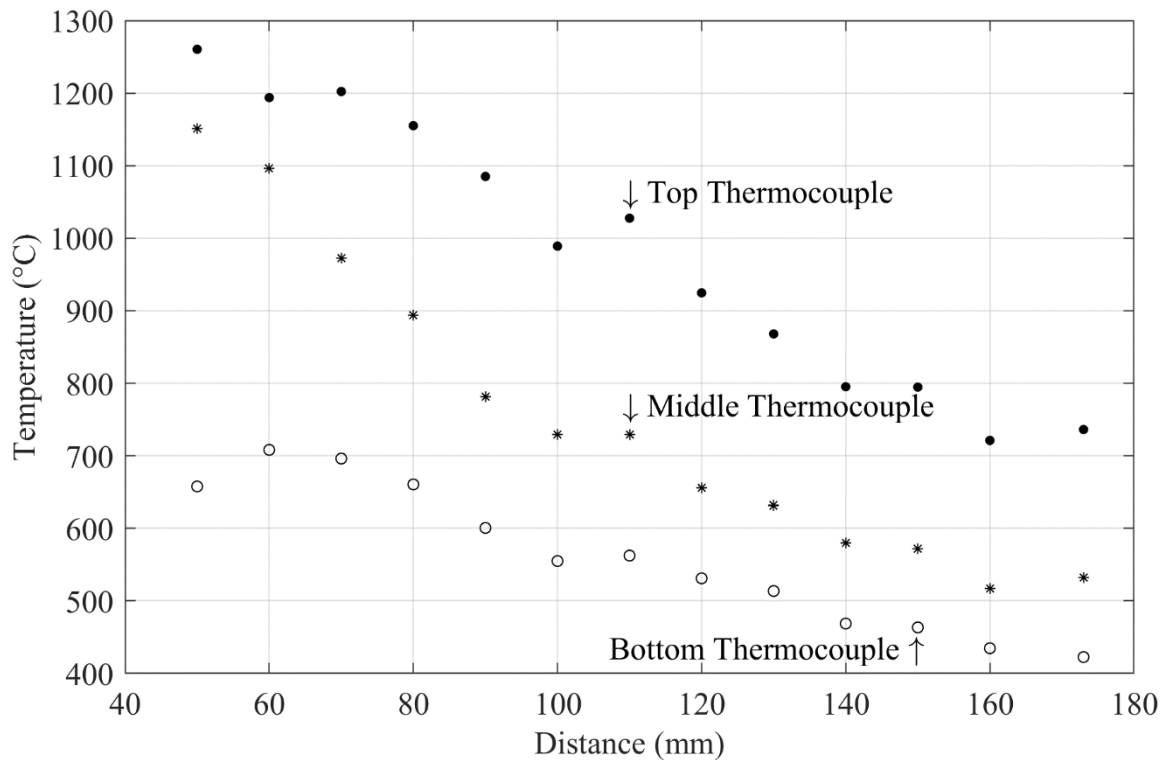
Figure 3.6. Temperature of all three thermocouples at steady state

In Fig. 3.6, the steady state temperature of all three thermocouples is plotted for all distances between the focal point of irradiation and the top surface of the lunar soil bed. The results are only sometimes consistent. It is seen from Fig. 3.6 that with a distance reduction, the rise of all three thermocouple temperatures is not uniform. One reason could be the change of focus to vary the irradiation distribution to achieve the highest peak irradiation at the center of the sample by concentrating, or distribute the irradiation uniformly all over the crucible. Also, the density of packing the simulant inside the crucible was sometimes different.

Fig. 3.7 represents the mass of sintered material during the experiments. It is clear that moving the crucible closer to the focus leads to higher temperatures and achieved more sintered/melted material. The inconsistency of temperature rises and sintered mass with reduction of distance is a result of nonuniform packing of simulant, error in thermocouple tip position, and nonuniform distribution of irradiation during experiments.
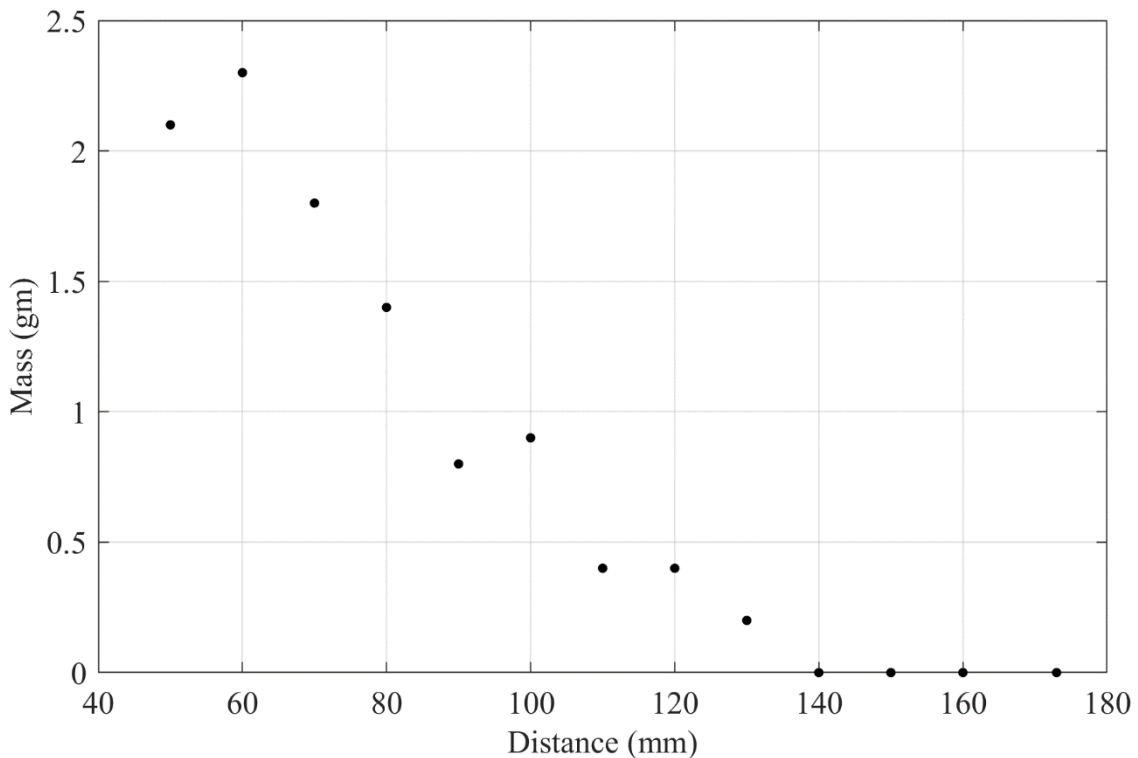
Figure 3.7. Mass of sintered LHS-1 with distance and variation of focus

3.2. Experiment Verification with Varying Focus

The previous set of experiments gave an idea of the sintering zone in terms of distance and input current. Another set of experiments was run to verify the outcomes with better control. This time the sintering experiment started from 160 mm and the distance was reduced by 5 mm to see the effect of the distance reduction more precisely. In this set, at every distance, the irradiation was concentrated by varying the focus and changing the position of the xenon arc lamp inside the simulator. Therefore, the irradiation was concentrated at each height. Since the input current was fixed at 60 A, at a reduced distance, higher irradiation was noticed with a higher top thermocouple temperature.

For 135 to 95 mm distance, a small black sintering point evolved, as shown in Fig. 3.8 for 135 mm distance. During experiments at heights between 90 and 80 mm, sintering occurred, with a melting region, as shown in Fig. 3.9. At 60 mm height, the sintered material was attached to the thermocouple, as shown in Fig. 3.10, which caused the sintered sample to break while removing.

Figure 3.8. Sintering started at 135 mm distance for 60 A current
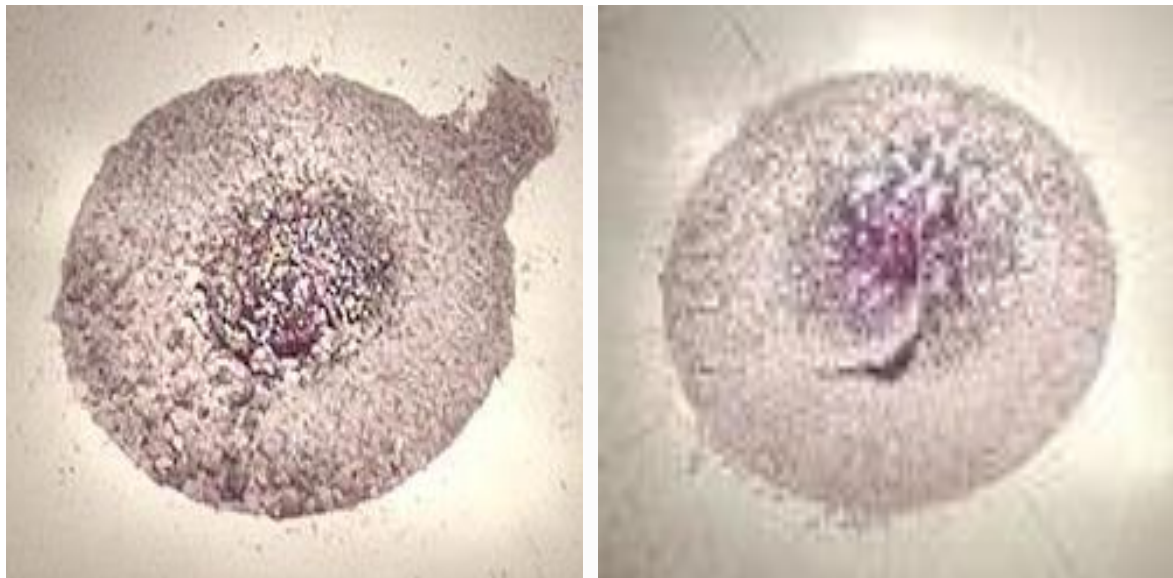
(A)   **(B)**

Figure 3.9. With 60 A input current (a) small melting zone at 90 mm distance

and (b) crack on sintered part at 80 mm distance

It is worth mentioning that if the height is reduced more, the lunar soil starts melting very early, creating balls, and attaching to the top thermocouple, which destroys the sintered particle and the thermocouple to separate them, which was not desired. So, the experiment was limited to 70 mm distance, where the melting was not prominent.

Figure 3.10. Attached sintered material with top thermocouple at 70 mm distance and 60 A input current

With decreased height and increased top thermocouple temperature, the mass of sintered material was increased, as listed in Table 3.2. Table 3.2 also presents the sintering start time, melting start time, and time to reach the system's steady state. It is noticeable that, as the thermal irradiation increased with reduced height, sintering and melting start time was reduced.

Fig. 3.11 shows the steady state temperature rise with the reduction of distance between the top surface of the LHS-1 and the focal point of the simulator. It can be noticed that the top thermocouples' steady-state temperature increases with the reduction of heights. The trend is uniform, following a linear increment for each 5 mm distance reduction. With increased thermal irradiation for reduced distance, the mass of sintered material increased, as shown in Fig. 3.12. Here an increased mass of sintered material is plotted with the steady-state temperature of the top thermocouple. As the steady-state temperature increases for the increased radiation level with reduced distance, more LHS-1 lunar soil simulant is sintered. This occurs due to the higher heat flux with increased radiation level, which transmits more heat through conduction into the particle's bed. The central thickness of the sintered pieces also increased due to higher heat flux with increased steady-state temperature.

Table 3.2. Direct sintering experiment data where the focus was concentrated for maximum irradiation at each distance

Distance (mm)	Sintering Start Time (min)	Melting Start Time (min)	Steady State Time (min)	Top Thermocouple Temperature at Steady State (°C)	Sintered Mass (gm)
160	-	-	30	750	0
155	-	-	30	780	0
150	-	-	30	810	0
145	-	-	30	830	0
140	-	-	40	838	0
135	04:00.0	-	35	860	0.01
130	04:00.0	-	45	890	0.1
125	03:30.3	-	34	900	0.1
120	03:00.6	-	32	920	0.2
115	02:00.4	-	44	930	0.3
110	02:00.4	-	47	984	0.4
105	02:00.4	-	49	1062	0.5
100	02:00.4	-	51	1075	0.6
95	01:20.3	-	34	1095	0.8
90	01:10.6	04:00.0	45	1120	0.9
85	01:00.2	04:00.0	29	1150	1
80	01:00.2	04:00.0	42	1195	1.2
75	00:45.7	03:30.3	38	1200	1.4
70	00:45.7	03:30.3	40	1235	1.5
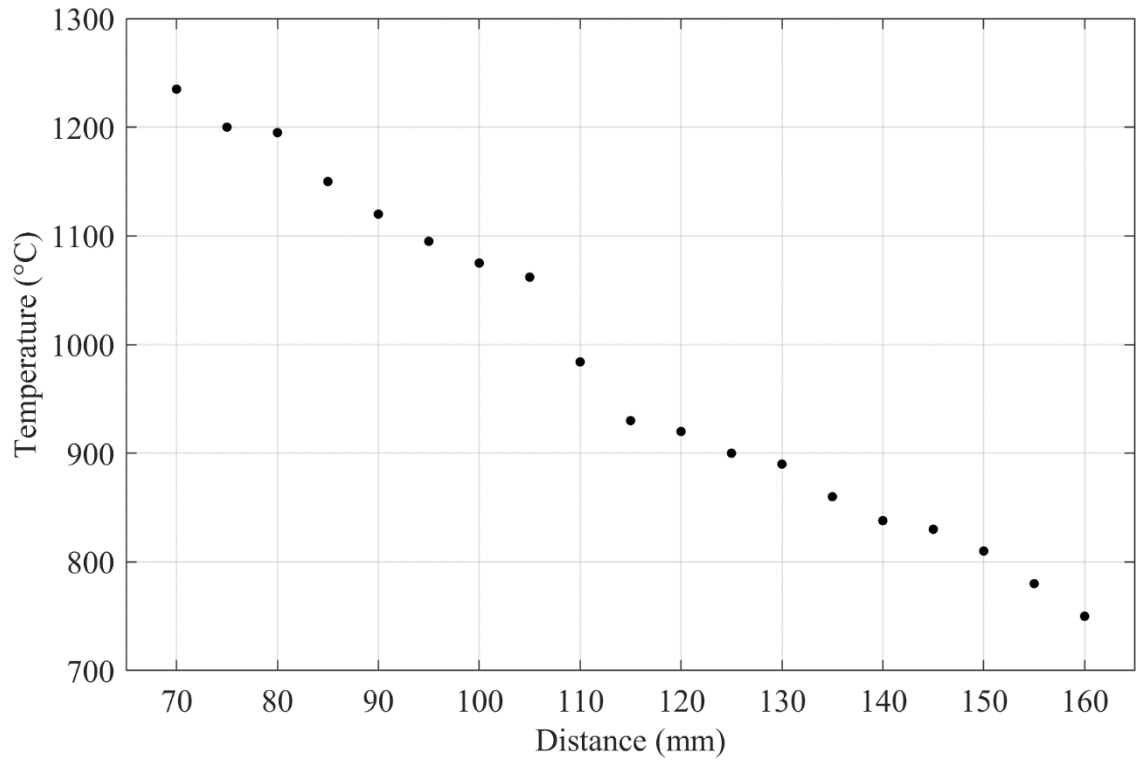
Figure 3.11. Top thermocouple steady state temperature with distance with varying focus and 60 A input current
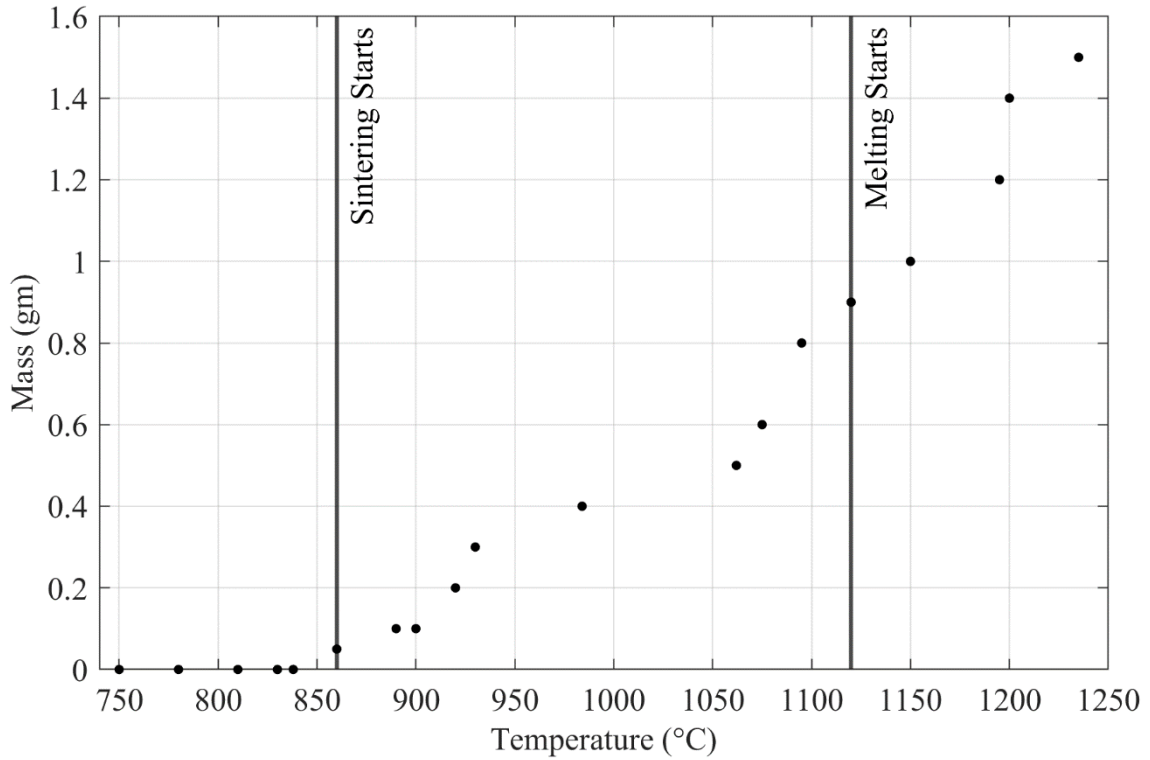
Figure 3.12. Variation of sintered mass with steady state temperature of top thermocouple for varying focus

Fig. 3.12 also denotes the sintering and melting start points in terms of the steady-state temperature of the top thermocouple. Sintering was noticed at top thermocouples steady state temperatures from 860°C to 1095°C. The mass of sintered material increased linearly with increased steady-state temperatures. The initial data set does indicate some temperature ranges and measurements of the sintered material. Still, they primarily serve as a learning set for the equipment, and detailed discussion is kept brief because a better set of data is presented later.

Unlike previous experiments from section 2.1, in this set of experiments of section 2.2, the top surface temperature was measured with a thermal imager along with the top thermocouple temperature. The thermal imager was available in the lab for the first time which was used to measure the top surface temperature. The experiments with the thermal imager were done for the distance of 70 mm to 100 mm. This is the distance at which significant amount of sintered material was achieved in preliminary experiments. Following the same procedure, the crucible was filled with 30 gm of LHS-1 lunar soil simulant and placed on the test stand.
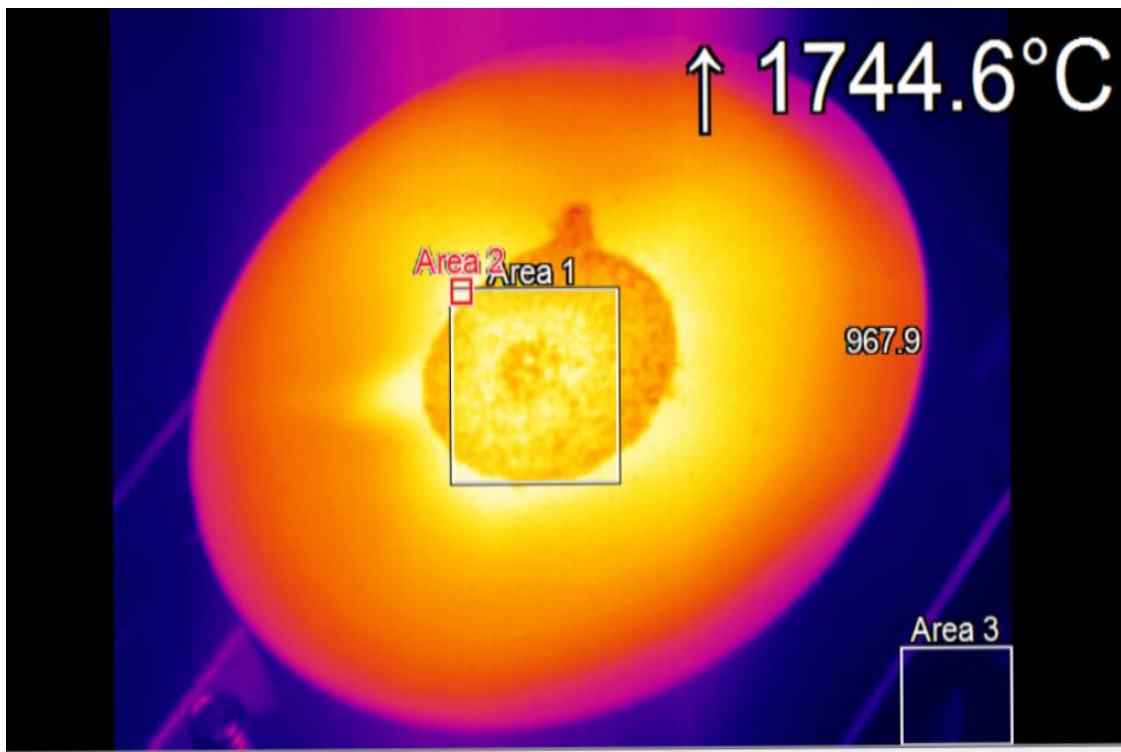
Figure 3.13. Thermal imager image focused on the top surface of LHS-1 bed

The thermal imager was focused on the top surface of the lunar soil simulant bed shown in Fig. 3.13. Thermal video data is recorded at times 2 min, 4 min, 6 min, 8 min, 10 min, 15 min, 20 min, 25 min, 30 min, 35 min, and at 40 min by closing the shutter of the solar simulator for a short time. With the maximum top surface temperature, a smaller area represents the top surface temperature for a tiny point, like a thermocouple tip. Temperatures at these times from the thermal imager were taken from the maximum average temperature over a 3 mm square area from the thermal image map.

Fig. 3.14 shows a plot of thermal imager and thermocouple measured temperatures for 100 mm distance between the LHS-1 lunar soil simulant surface and the solar simulator focal point. The top dotted points present the thermal imager data of the top surface temperature for the previously mentioned intervals. The top thermocouple temperature profile represents the temperature 2 mm beneath the top surface of the simulant. Temperature drops are seen in only the top thermocouple at each time when the shutter is closed.
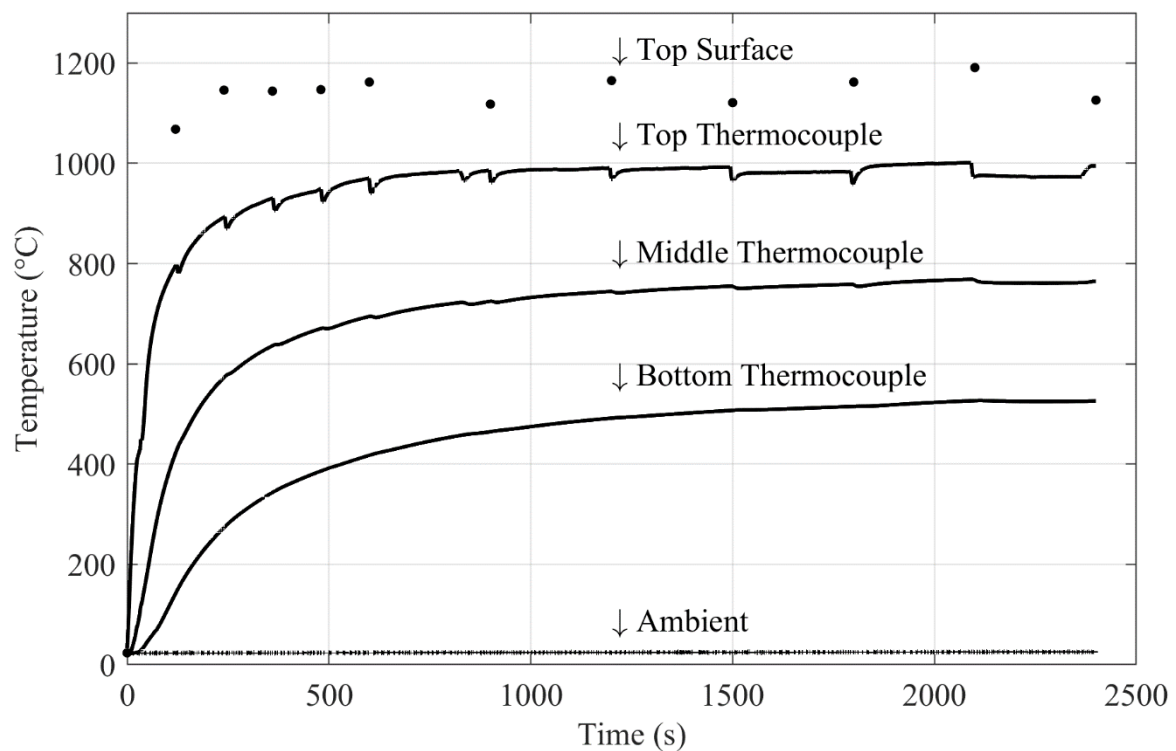
Figure 3.14. Temperature profile of a direct sintering experiment with the thermal imager and three thermocouples for 100 mm distance and 60 A current
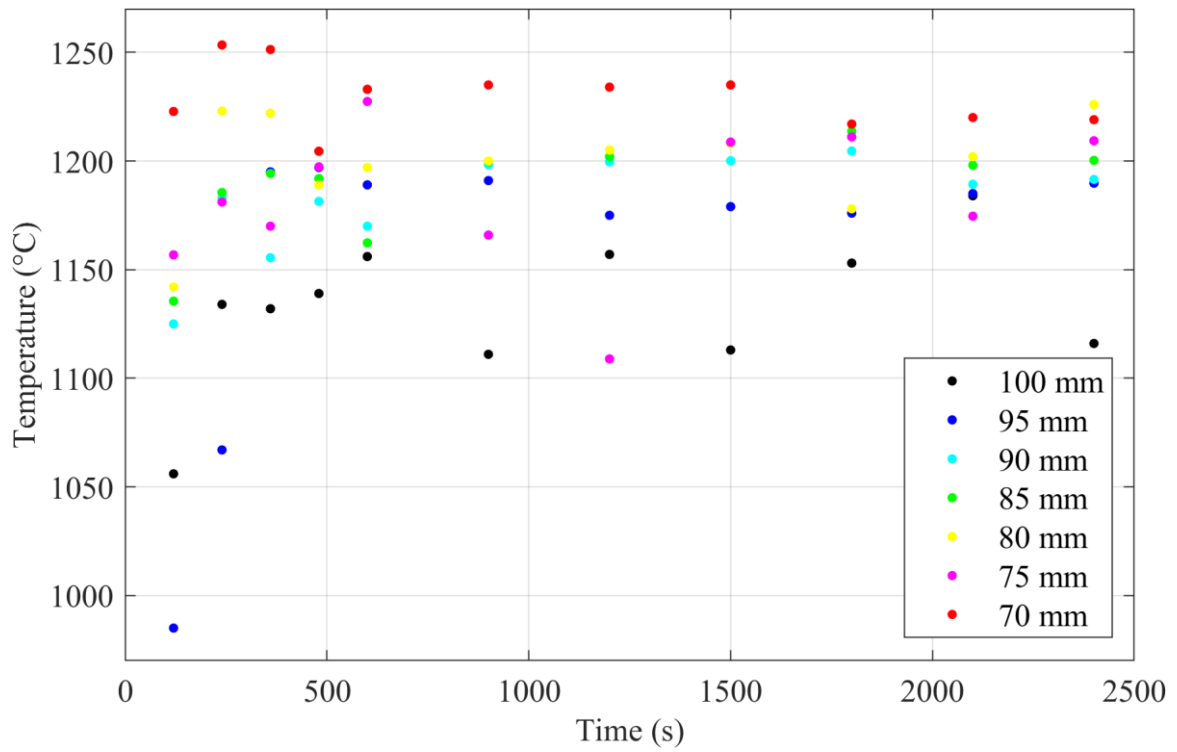
Figure 3.15. Top surface temperature of LHS-1 over time
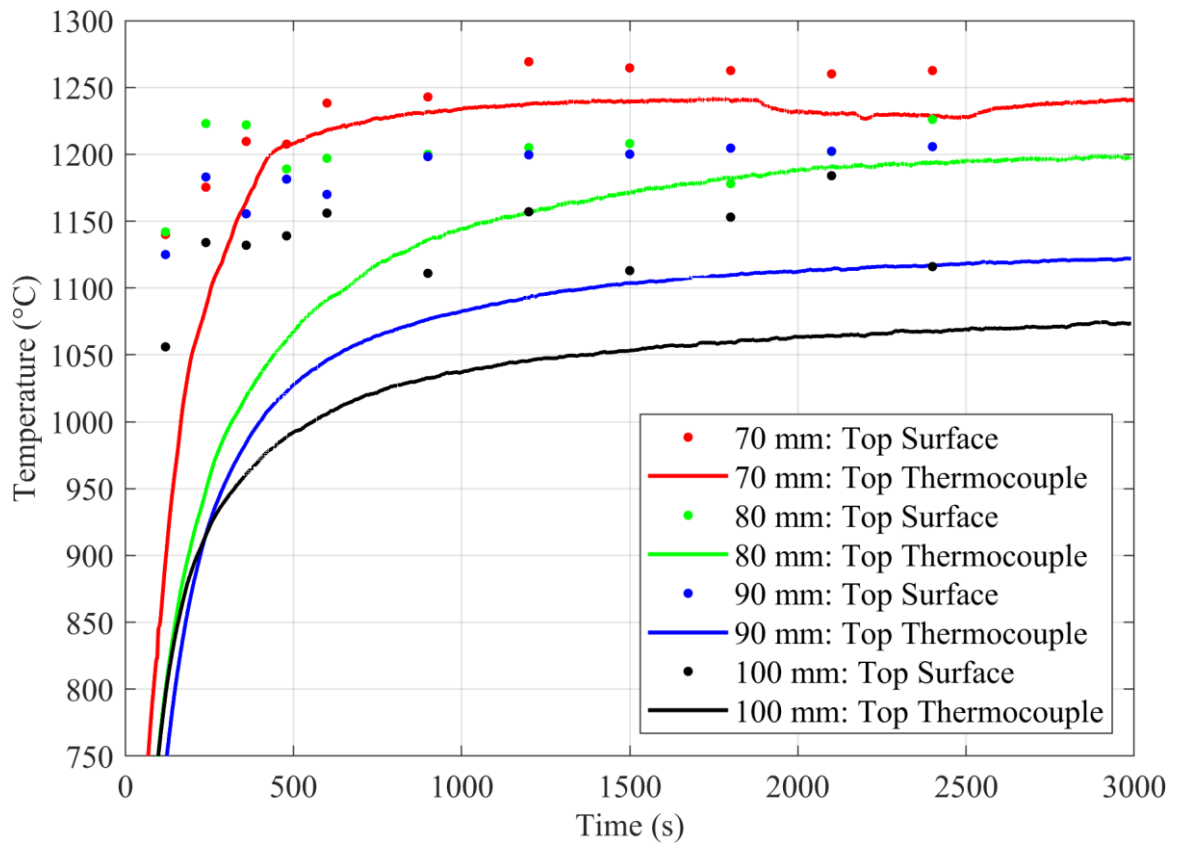
Figure 3.16. Comparison of the top surface and top thermocouples temperature profile

for different radiation levels with distance

34

Experiments were run for distances from 70 mm to 100 mm at the same conditions of lamp current and lamp focus. The top surface temperature of the lunar soil simulant bed at 2 min, 4 min, 6 min, 8 min, 10 min, 15 min, 20 min, 25 min, 30 min, 35 min, and 40 min were recorded. The top surface temperature of the lunar soil simulant bed at different distances is plotted over time in Fig. 3.15.

Fig. 3.16 shows the progression of the top thermocouple temperature along with the top surface temperature with time for different distances representing radiation level. To understand the progression, data was taken twice. Once without the thermal imager to obtain a continuous temperature profile for the top thermocouple without any temperature drop due to shutter closure and another with the thermal imager only to detect the top surface temperature. The dotted points represent the top surface temperature at the previously mentioned time interval, whereas the constant line represents the top thermocouple temperature profile. The same color in the graph represents data for the same distance between the top surface of the lunar soil simulant and the mirror's focal point. From the top thermocouple temperature profiles, it is visible that, with reduced distance and increased thermal irradiation, the rise of temperature is rapid, and the lunar soil simulant reaches steady state temperature faster. This defines the increased heating rate with an increased slope for higher thermal irradiation. Another noticeable factor is that the top surface goes to the steady state earlier than the top thermocouple. The increased heat flux increases the heat conduction for reduced distance and the top thermocouple temperature profile slope increases.

Fig. 3.17 shows that the top surface temperature for each distance is much higher than the top thermocouple temperature. As explained before, with reduced distance, the heat transfer increased through the lunar soil simulant bed. Some possibilities are that the higher temperatures lead to better heat transfer in the bed due to radiation helping to transfer heat and more particles contact when sintering begins so the thermal conductivity of the bed increases.

The temperature difference between the top surface and the top thermocouple is reduced at steady state.
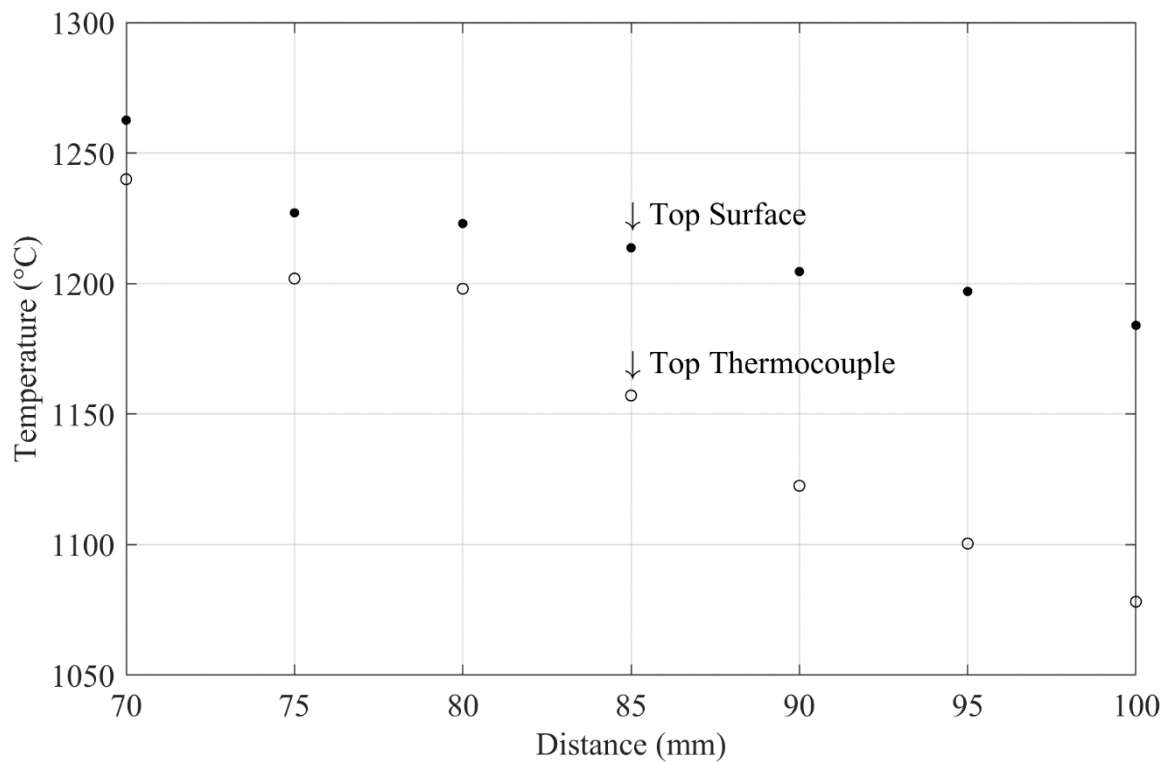
Figure 3.17. Comparison of maximum top thermocouple temperature and maximum top surface temperature with distance at steady state

Figure 3.18. Sintered sample for 70 mm distance

Fig. 3.18 shows a sintered sample for 60 A current input and 70 mm distance before and after cutting a rectangular sample for compressive strength testing. It would also be more suitable to use the rectangular sample for constructional use than the non-uniform sintered pieces.

3.3. Experiments Fixing the Focus at Focal Point

The previous two sets of experiments were conducted using an aluminum mirror. The reflected flux distribution was repeatable but not as uniform as required. The aluminum mirror was replaced with a glass mirror used explicitly in solar simulators. The new glass mirror reflected the solar irradiation more uniformly than the previous one, as shown in Fig. 3.19. Also, during the earlier experiments, the focus of the irradiation was changed at each distance to concentrate the irradiation by changing the bulb position relative to the reflector. To make the experiment uniform, the irradiation was concentrated at 50 mm distance. The following experiments were conducted without changing the bulb position and focus, only by increasing the distance.

(A)   **(B)**
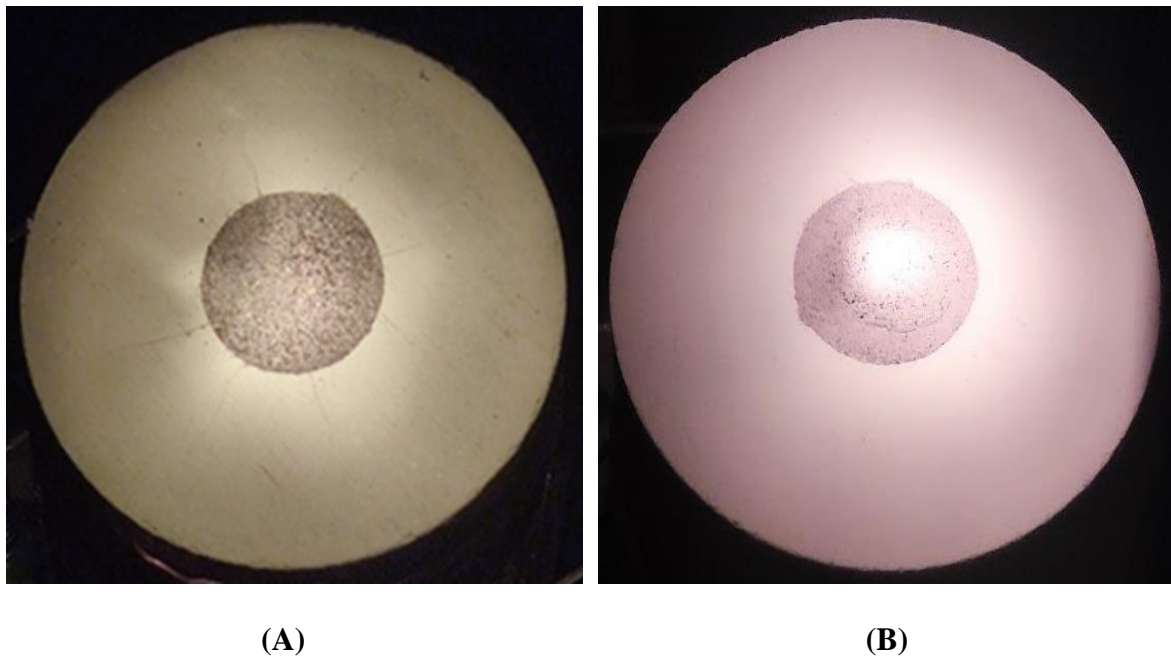
Figure 3.19. Concentrated irradiation with (A) aluminum mirror and (B) glass mirror

In addition, a new batch of LHS-1 lunar soil simulant was used, Fig. 3.19 (A), finer than the previous batch used in earlier experiments, as seen in Fig. 3.19 (A). The new batch was more uniform in terms of grain size. SiC plate was another addition to the experimental procedure to find the heat flux by measuring stagnant temperature as explained earlier. With all the updates in the lab, the following sets of direct sintering experiments were conducted.

In this set of experiments, all the experiments were conducted for 50 minutes, with 60 A input current to the xenon-arc lamp. All experiments began at time zero when radiation was first introduced to the bed of simulant at ambient temperature. The distance between the top surface of the simulant bed and the focal point varied from 90 mm to 50 mm. A piece of SiC plate was used to measure the top surface temperature using the new thermal imager to capture a maximum temperature and calculate a heat flux. The conversion of top surface temperature to heat flux was done with the Stephen-Boltzmann equation as described in Chapter 2. Table 3.3 shows the conversion of different distances to irradiated heat flux.

Table 3.3. Conversion of distance to heat flux

Distance (mm)	SiC Temperature (°C)	Flux (kW/m^2)
90	863	85.0
85	898	96.0
80	927	105.8
75	948	113.4
70	988	129.0
65	1039	151.2
60	1055	158.7
55	1111	187.2
50	1177	225.6

Following the same heating condition corresponding to the flux measurement experiments, sintering experiments were run with LHS-1 lunar soil simulant at each distance. During the experiments, keeping the irradiation concentrated at 50 mm distance, achieved experimental data are listed in Table 3.4.

Table 3.4. Experimental data with concentrated irradiation fixed at 50 mm distance with 60 A input current

Distance (mm)	Sintering Start Time (min)	Melting Start Time (min)	Top Thermocouple Steady State Temp (°C)	Top Surface Temperature (°C)	Flux (kW/m^2)
90			830	861.8	85.0
85			900	1008.3	96.0
80	7:00		915	1121.6	105.8
77.5	3.30		990	1135.0	109.6
75	1:30		1045	1250.1	113.4
72.5	1:10		1109	1255.0	121.2
70	0:50	1:55	1166	1261.8	129.0
65	0:35	1:15	1240	1310.0	151.2
60	0:26	0:55	1270	1362.3	158.7
55	0:20	0:40	1340	1417.0	187.2
50	0:15	0:30	1325	1435.3	225.6

Similar to section 3.2, with the thermal imager, the top surface temperature of LHS-1 was measured at 2 min, 4 min, 6 min, 10 min, 15 min, 20 min, 25 min, 30 min, 35 min, 40 min, 45 min, and 50 min. Fig. 3.20 compares the top thermocouple and top surface temperatures recorded with the thermal imager for 50 minutes. The heating rate is significantly higher for

higher heat flux with reduced distance. At 50 mm height and a heat flux of 225 kW/m^2, the heating rate over the first time constant of the response is 13.9°C/s, compared to 6.0°C/s at 80 mm and a heat flux of 105.8 kW/m^2. Between the top thermocouple and the top surface temperatures, the top surface goes to steady state earlier than the top thermocouple, as conduction through the simulant causes a delay. Top thermocouples generally read 30-40°C below the top surface temperature at steady state, with differences of 100°C typical during transient heating periods.
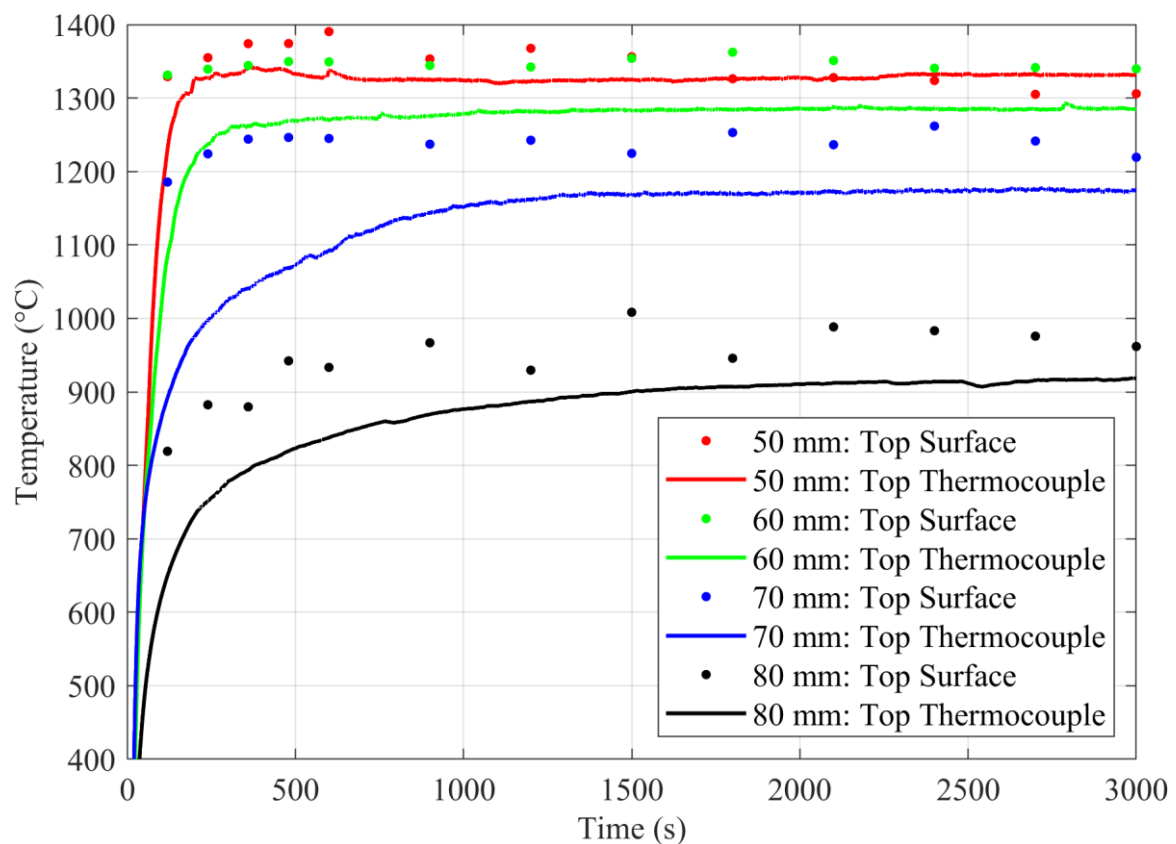
Figure 3.20. Comparison of top thermocouple temperature profiles with distance

The top thermocouple temperature increases for the increase of heat flux with reduction of the crucible distance. The rate of this increase decreases with increasing heat flux, as shown in Fig. 3.21, displaying the typical behavior as thermal losses become more radiatively dominant. As the crucible height increases, the flux decreases by the square of the distance,

and radiative losses scale with the fourth power of temperature. Higher heating rates at higher

flux levels lead to an earlier start of sintering and melting.
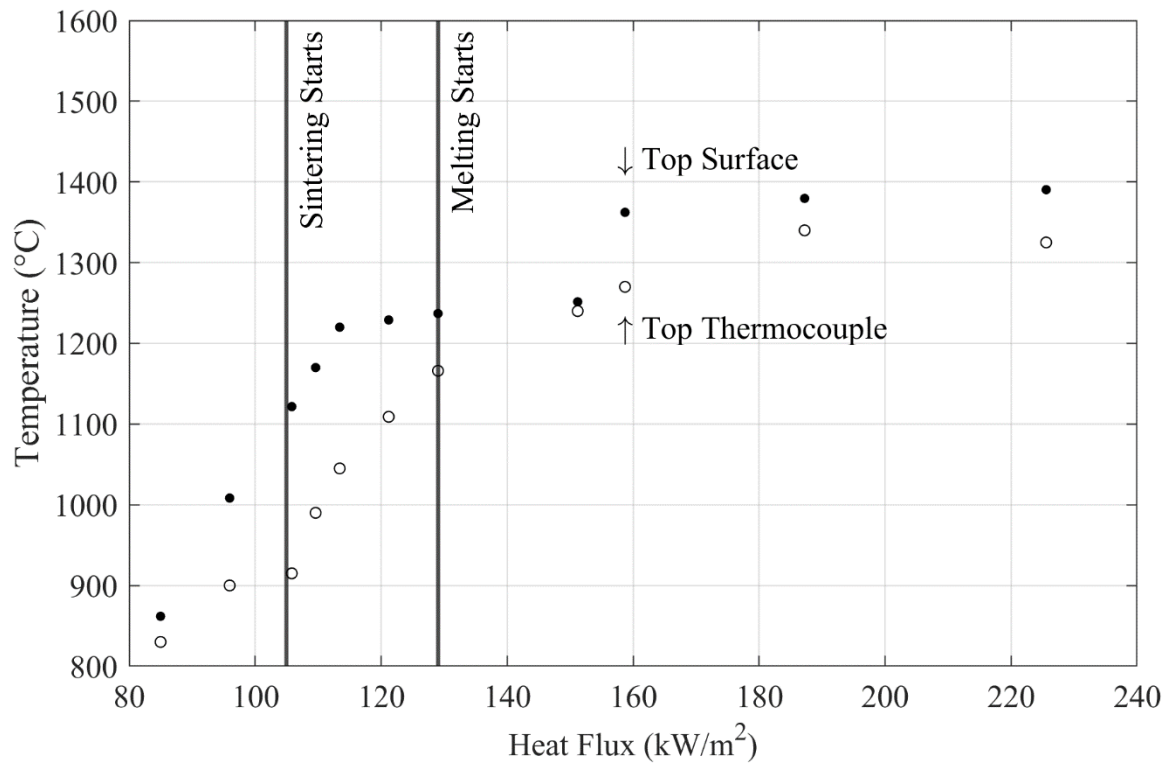
Figure 3.21. Top thermocouple and top surface temperature with heat flux

(A)

(B)
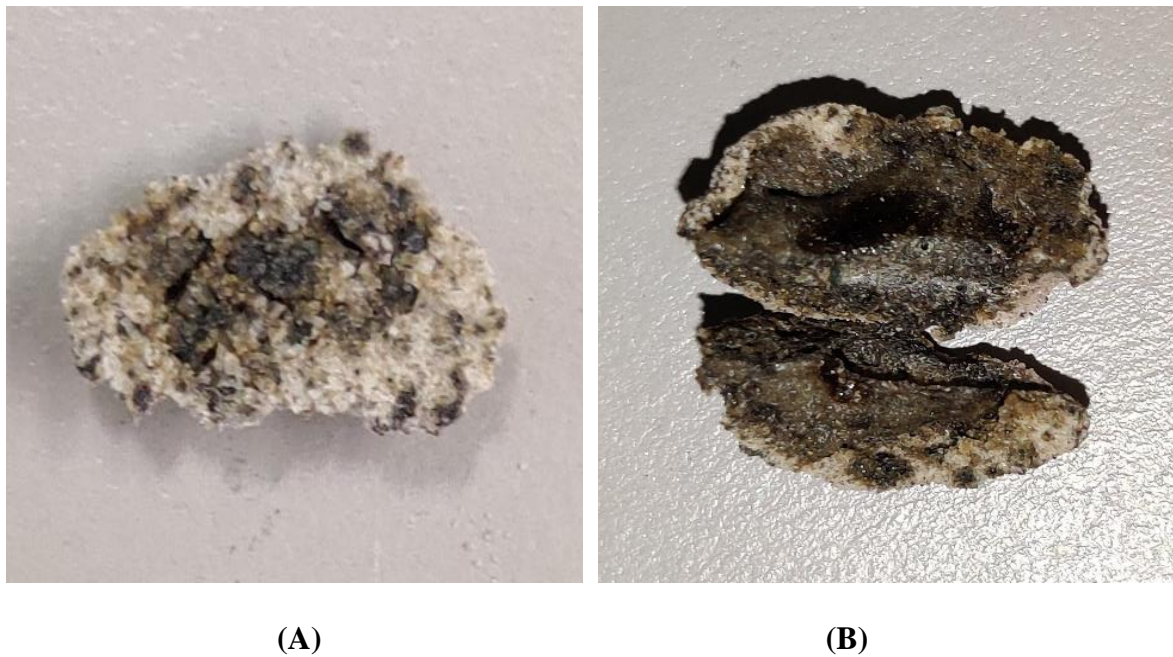
Figure 3.22. Sintered pieces at (A) 105 kW/m² and (B) 151.2 kW/m²

Sintering occurred for samples taken to steady state at heat fluxes greater than 105 kW/m^2, while melting occurred at heat fluxes greater than 129 kW/m^2 [63]. Sintered samples are shown in Fig. 3.22. Solar concentrators commonly produce heat flux between 200 and 1000 kW/m^2 [64], so even a low-quality concentrator can sinter or melt lunar soil simulant. However, these are minimum values of flux that require several minutes to produce a negligible amount of sintered material. It would be recommended to use higher levels of flux in practice. With time the flux can be carefully controlled to achieve the level of sintering desired. For example, at a flux of 225 kW/m^2, sintering begins within 15 seconds and melting begins within 30 seconds, providing some level of sintering and a window to reduce or stop solar irradiation before melting occurs.

In Fig. 3.23, the mass of sintered material is plotted with heat flux and steady-state temperature of the top thermocouple. As steady-state temperature increases with the increased heat flux, the mass of sintered soil simulant increases, as expected. Fig. 3.24 shows the central thickness of the sintered pieces also increased due to higher heat flux and increased steady-state temperature. The maximum central thickness achieved is 8 mm with direct sintering at 225 kW/m^2 heat flux.

Because the simulant was held at near-steady temperatures for several minutes, the mass of sintered material and the thickness could not be increased simply by additional time. Experiments show that the upper limit of sintering thickness without melting the surface of the material is approximately 4 mm using the LHS-1 simulant. Greater sintering depth is possible when the surface is allowed to melt. Such experiments with higher temperatures were not attempted because melt pools with the diffusive flow and considerable thickness occur at temperatures above 1300°C, which would be undesirable for structural applications.
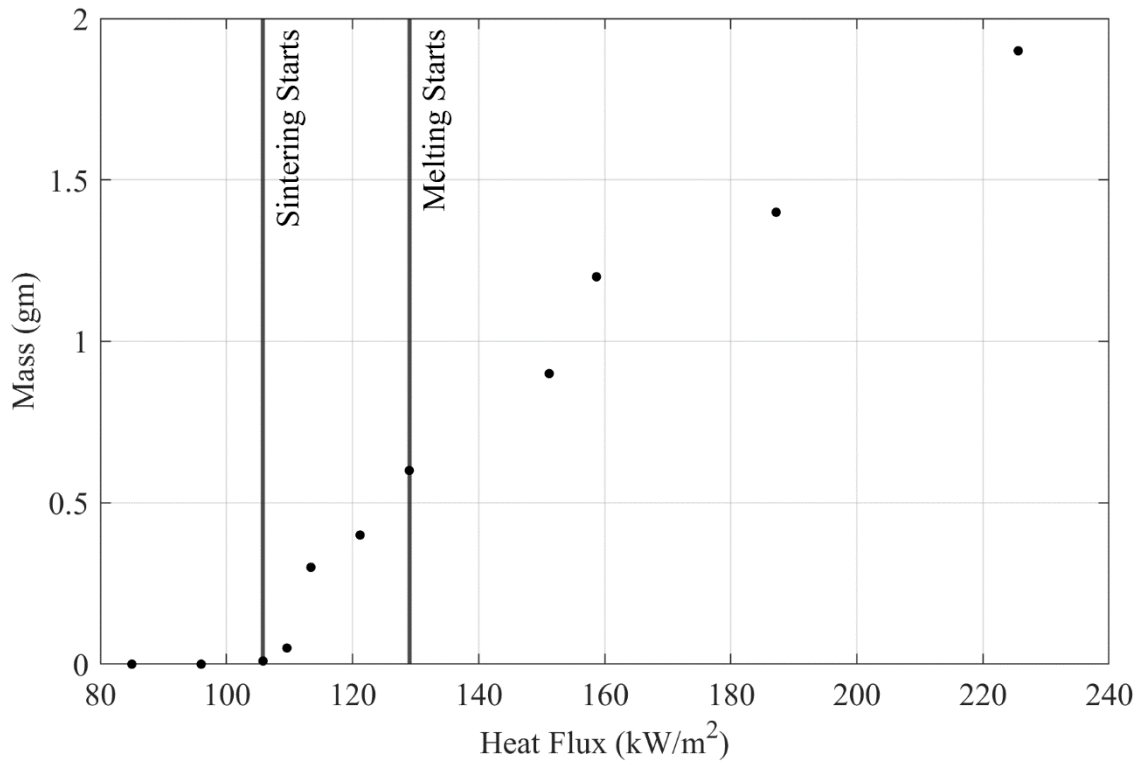
(A)
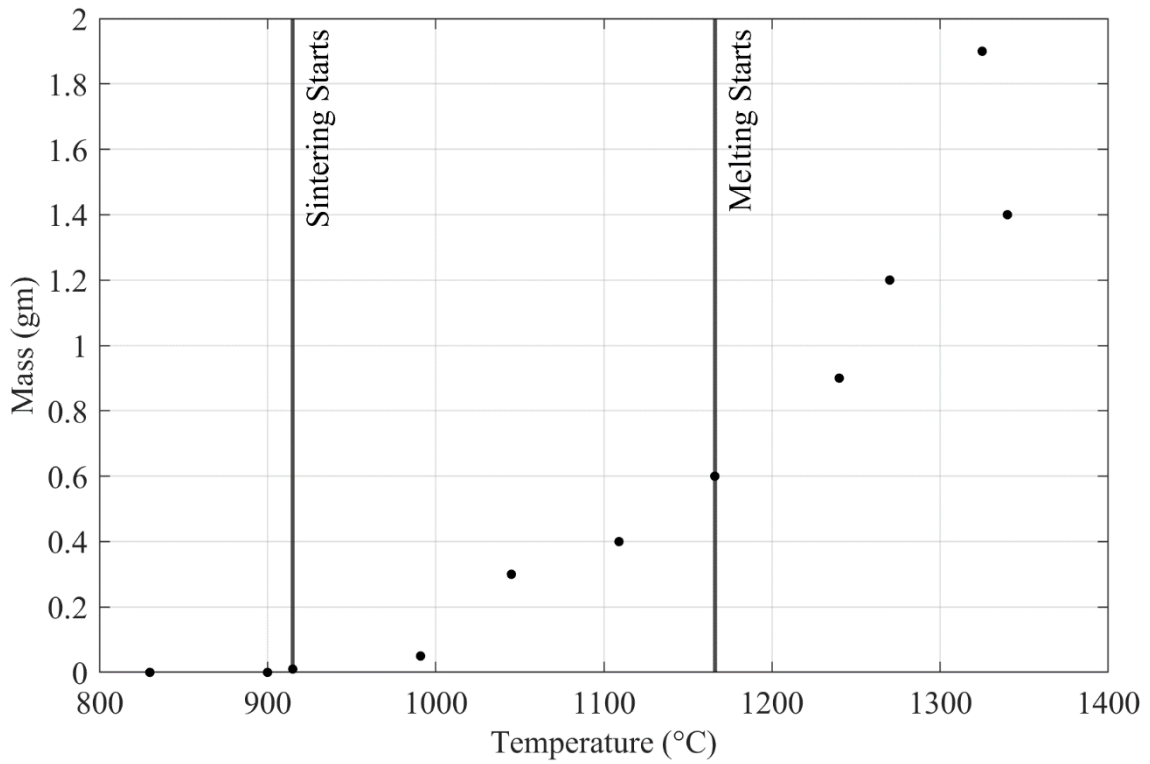
(B)

Figure 3.23. Variation of sintered mass with (A) heat flux and

(B) steady state temperature of top thermocouple
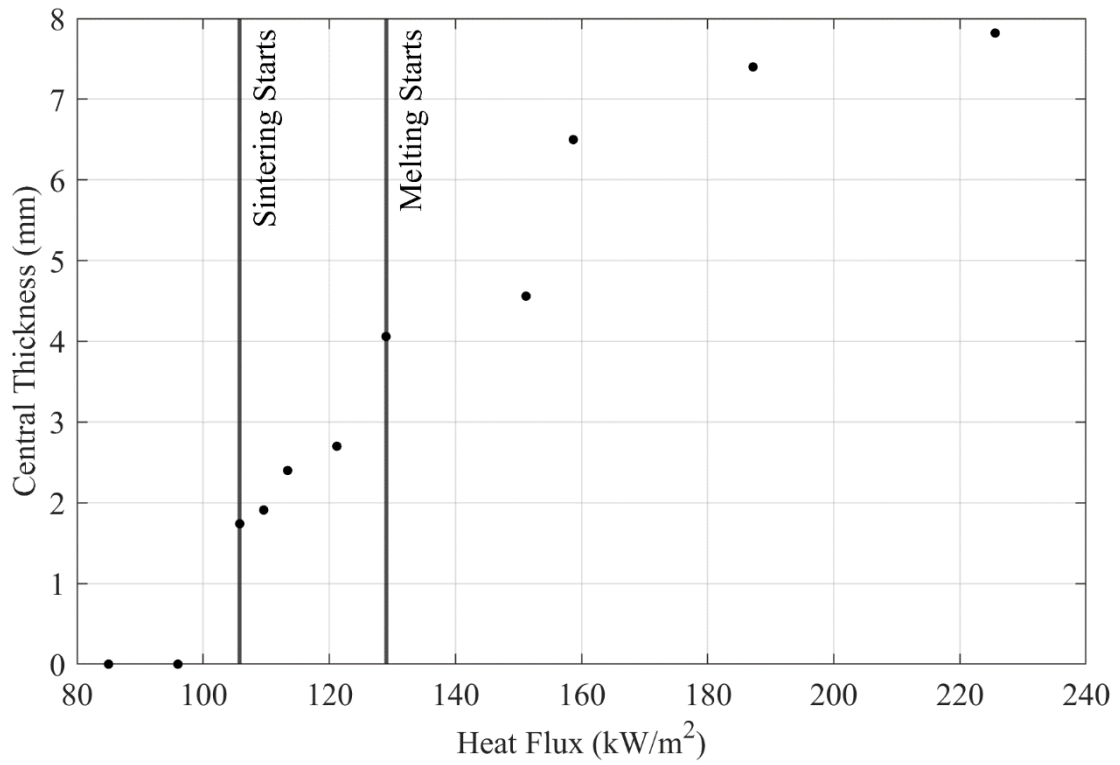
(A)
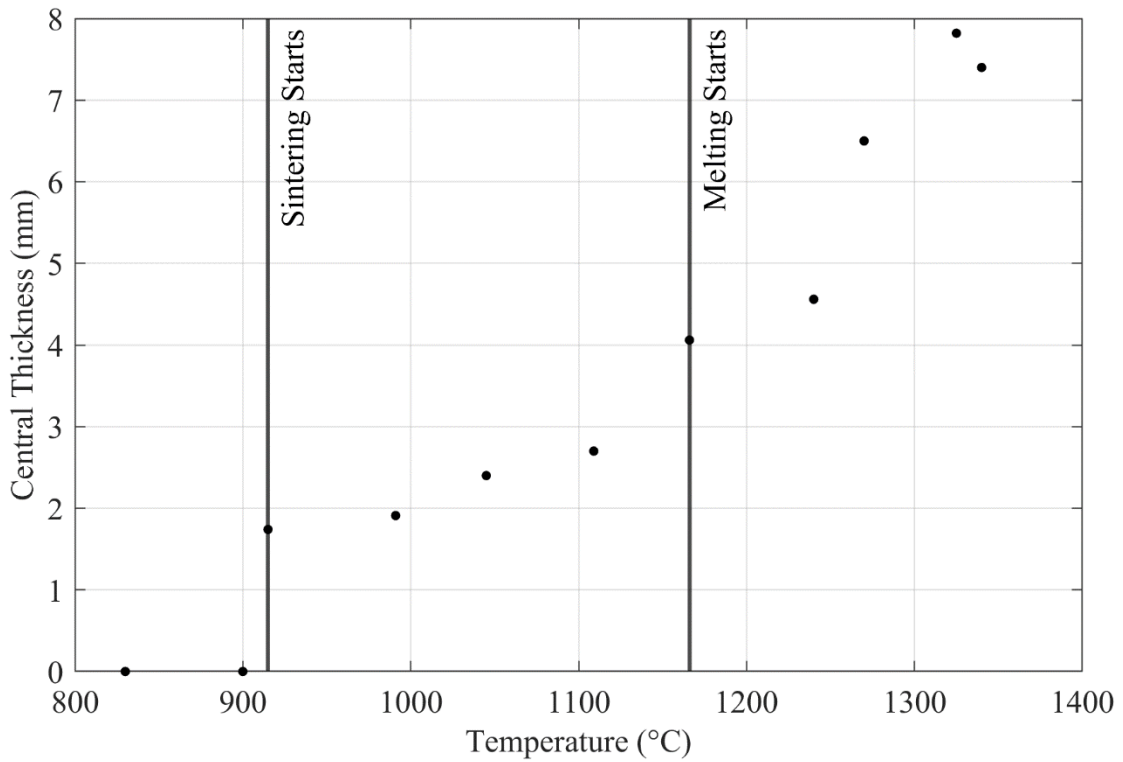
(B)

Figure 3.24. Variation of central thickness with (a) heat flux and

(b) steady state temperature of top thermocouple
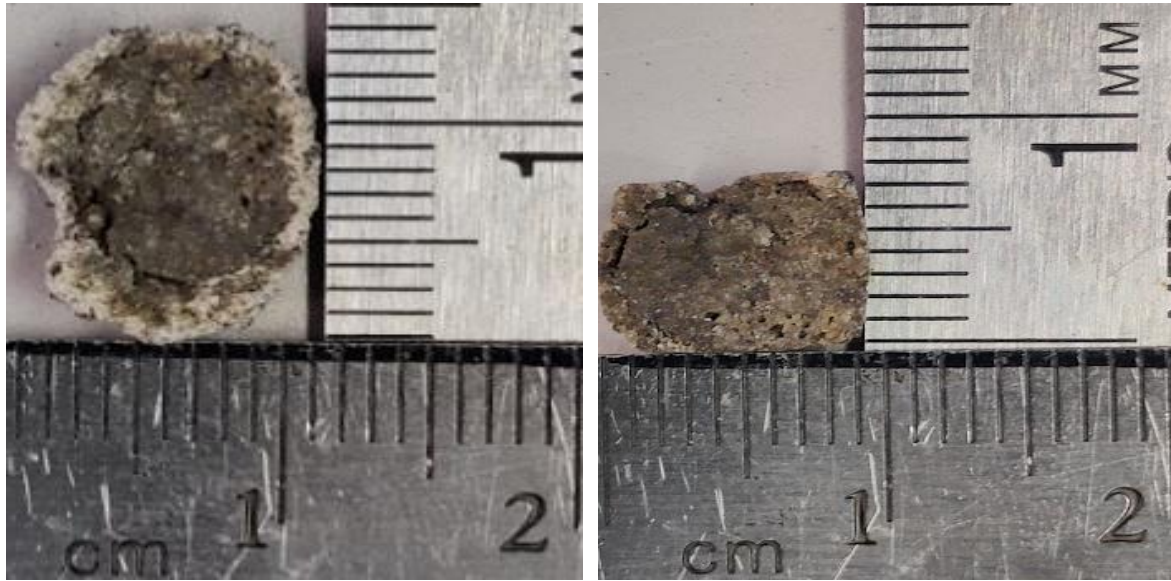
Figure 3.25. Directly sintered samples for 70 mm distance

Fig. 3.25 shows a sintered sample for 60 A current input and 70 mm distance from the focus, the most significant distance where melting is first seen. The sintered material is shown before and after grinding to give an appropriate shape for strength testing.

3.4. Different Direct Sintering Techniques for Large Lunar Brick

LHS-1 lunar soil simulant is a mixture of oxide minerals that naturally have poor thermal conductivity. Also, the bed of particles has poor conductivity because the spaces between the particles are filled with poor conductive gas or vacuum, limiting the ability to sinter large pieces of lunar bricks. In addition, the concentrated irradiation impinges over a small area, making the cross-section area very small. Constructional use requires large lunar bricks, and different approaches are experimented with to sinter large lunar bricks. This section presents the outcomes of various techniques to sinter comparatively larger bricks with LHS-1 lunar soil simulant.

3.4.1. Single Point Sintering with Flipping

The first experiment was conducted following the same procedure of sintering, focusing the concentrated solar irradiation on the top surface of the lunar soil simulant bed. 30 gm of

lunar soil simulant was measured and poured inside the crucible to make it compact. In this experiment, the distance between the focal point and the top surface of the lunar soil simulant was 95 mm with an input current of 60 A. After sintering for 40 minutes, the sintered piece was removed and weighed. The sintered mass was 1 gm. Some simulants was removed from the simulant bed to place the sintered part after flipping. Then another layer of lunar soil simulant was placed on top of the sintered part and sintered for another 40 minutes. The sintered piece is removed, and after flipping, the total mass becomes 2.4 gm in 80 minutes. The same experiment was run twice, and the same amount of sintered material was produced. Fig. 3.26 shows the final product with a grooved joint in between.

Figure 3.26. Flipped single point sintered lunar brick

After the flip, a thinner lunar soil simulant layer can produce a better brick with a larger joint cross-section area and less depression, increasing the strength of the joint and the sintered brick. The challenge of this technique is positioning the concentrated light at the center after flipping.

3.4.2. Multi-Point Sintering

For single-point sintering with concentrated sunlight, the sintered top surface area was not large enough. A multipoint sintering approach was followed to sinter the top surface of the

poured LHS-1 thoroughly. It was a rough simulation of a 3-D printing process where the light moves to different points on a larger surface. Experimentally to test this, the distance between the top surface and focal point was set for 95 mm with 60 A current input. After pouring the LHS-1 inside the crucible, it was placed under concentrated irradiation. After sintering the center, four sides of the center were sintered by moving the crucible to impinge the irradiation on these sides, creating a plus-shaped piece with four pockets near the edges. Then these four points were sintered again focusing the incoming irradiation by moving the crucible. A total of nine spots were sintered all over the top surface, changing the crucible's position. Each operation was run for 40 minutes, totaling 6 hours to sinter the top surface of the lunar soil simulant bed, Fig. 3.27. The total sintered mass was 2.9 gm.
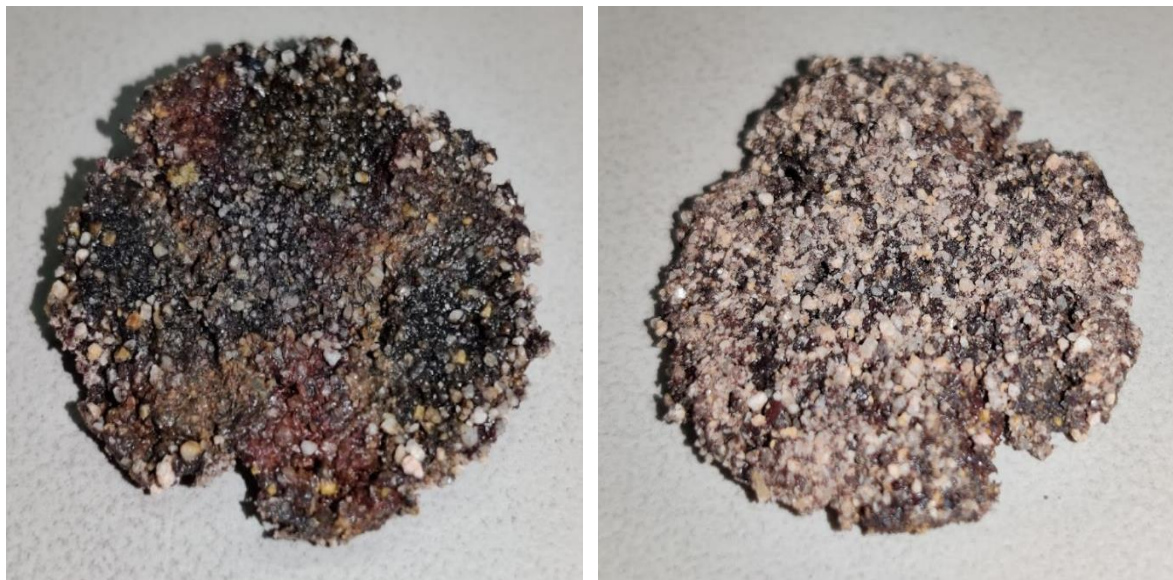
Figure 3.27. Multipoint sintered lunar brick

The limitation was positioning the crucible correctly for sintering each neighboring point. If the position of concentrated irradiation became inappropriate, two sintered pieces would have not attach to make a large brick. Also, much time and energy were wasted to sinter the other small sections after sintering the plus-like shape.

3.4.3. Three-Point Sintering with Flipping

Multipoint sintering required longer time than single-point sintering with flipping, but the sintered mass was not satisfactory. So, a sintering technique was tried by combining both the previous methods. The trial was done by sintering three linear points following a straight line, which gave a decent brick-like shape, then flipped and again sintered another straight line following the last three spots, as in Fig. 3.28. The exact configuration was followed for this experiment with a 95 mm distance and 60 A current input. Each point was sintered for 40 minutes, totaling 4 hours of operation. A total of 3 gm of material was sintered. The sintered mass before flipping was measured at 1.4 gm, so after flipping, 1.6 gm of material was sintered.

| (A) | (B) |
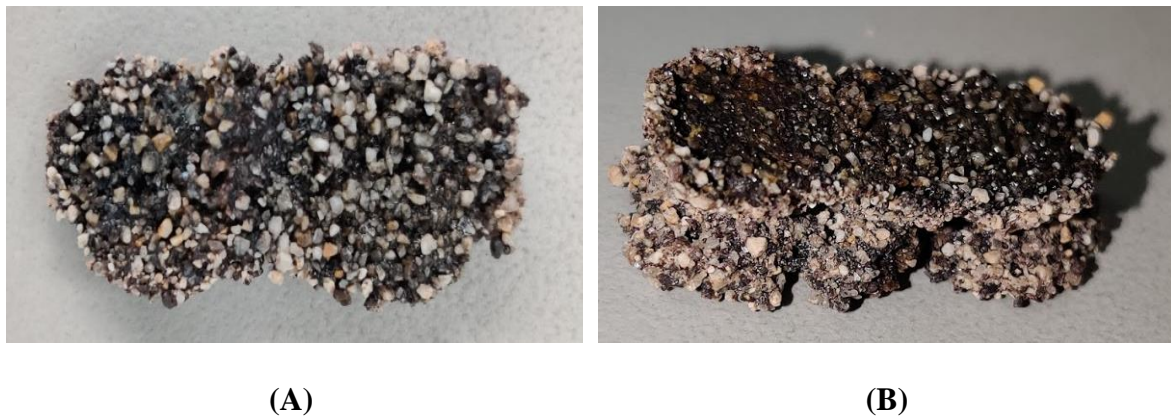
Figure 3.28. Sintered brick with three-point sintering with flipping

(a) before flipping (b) after flipping

Table 3.5. Comparison of techniques to sinter large lunar bricks

Properties	Single Point Sintering with Flipping	Multi Point Sintering on Top Surface	Three-Point Sintering with Flipping
Distance	95 mm	95 mm	95 mm
Time	2×40 = 80 min	9×40= 360 min = 6 hr	6×40= 240 min = 4 hr
Sintered Mass	2.4 gm	2.9 gm	3.0 gm

Table 3.5 shows that single-point sintering with flipping provides a better sintered mass-to-time ratio than the other techniques. The single point sintering may sinter more material in less time, but it is limited to tiny pieces. At the same time, the multi-point, in theory, could keep moving the focus to sinter a large amount of material. More layers in this technique would produce larger, sintered pieces altogether, giving the idea of layer-by-layer sintering.

3.4.4. Layer-by-Layer Sintering

Since single-point sintering with flipping was most promising compared to other techniques above, single-point layer-by-layer sintering was approached to sinter multiple layers instead of two layers in single-point sintering with flipping. Layer-by-layer sintering technique is a well-established technique [6], [24], [26], [65], which was carried out to see the performance by varying experiment time, distance, and layer thickness.

To sinter with layers, first, lunar soil simulant was measured and poured inside the crucible keeping the top of the crucible empty. For example, to make three 1 mm thick layers, 3 mm top of the crucible cylinder was kept empty. For all trials, the lamp current was held constant at 60 A, but the distance between the top surface and focal point was varied in addition with varied time duration, layer thickness, and the number of layers. The crucible cavity is approximately 25 mm deep and can hold 30 gm of lunar soil simulant; therefore, it takes 1.2 gm of material to make a 1 mm layer inside the cylindrical crucible.

Figure 3.29. Layer by layer sintering with sintered pieces of three 3 mm layers

49

For the first trial, the crucible was filled with lunar soil simulant in such a way that about 9 mm of the top was empty. The objective was to put three 3 mm layers and sinter for 40 minutes each. The distance of the top surface was kept at 95 mm after pouring each layer. After pouring a 3 mm layer, the distance was measured from the top surface, keeping 6 mm of the cylindrical crucible empty and sintered for 40 minutes. The amount needed to make a 3 mm layer was measured, which was 3.6 gm while running the experiment, and after 40 minutes next layer of material was poured. To maintain the distance at 95 mm, the crucible holder was lowered by 3 mm. Following the same process, three layers were sintered, as shown in Fig. 3.29, combining 4.8 gm of sintered brick in 2 hours. It was noticed that, during the first two layers, when the crucible's hollow top part created a cavity, the irradiation bounced back from the open crucible wall, which hit the top surface resulting in higher irradiation and a more significant sintered amount.

The second trial was with two 3 mm layers in the same configuration. In this case, the layers were sintered for 30 minutes each. 3.6 gm material was poured each time to put in a 3 mm layer and sintered for 30 minutes which was continued twice for two layers of materials that produced 2.5 gm of sintered brick. Compared to single-point sintering with flipping, the two 3 mm layers produced a similar amount of sintered brick in less time, which again sintered more material due to the cavity created by the hollow top part of the crucible.

The third trial's objective was to put a 2 mm layer and sinter for 20 minutes. 2.4 gm material was poured each time to put in a 2 mm layer and sintered for 20 minutes each which was continued three times to sinter three layers of materials altogether, making 1.3 gm sintered brick. After sintering, the measured thickness of the sintered piece was 8 mm.

For the fourth trial, five 1 mm layer was sintered for 10 minutes each to sinter five layers of materials altogether in 50 minutes which was 1.4 gm. For the fifth trial, the distance was reduced to 90 mm. Following the same number of layers and sintering time, 1.7 gm

sintered material was produced, which was better than the prior trial due to higher irradiation with reduced distance. By increasing the sintering time up to 15 minutes, for 90 mm distance, six 1 mm layer was sintered, producing 2.4 gm sintered lunar brick in 90 minutes. The thickness of the sintered piece was 10.3 mm. Since the distance was reduced to 90 mm, some balling effect was noticed during the sintering of each layer.

Table 3.6. Comparison of different combinations of layer-by-layer sintering

Properties	Trial 1	Trial 2	Trial 3	Trial 4	Trial 5	Trial 6
Distance	95 mm	95 mm	95 mm	95 mm	90 mm	90 mm
Layer Depth	3 mm	3 mm	2 mm	1 mm	1 mm	1 mm
No. of Layers	3	2	3	5	5	6
Time	$3\times40 =$ 120 min	$2\times30 =$ 60 min	$3\times20 =$ 60 min	$5\times10 =$ 50 min	$5\times10 =$ 50 min	$6\times15 =$ 90 min
Sintered Mass	4.8 gm	2.5 gm	1.3 gm	1.4 gm	1.7 gm	2.4 gm
Sintered Time/Mass	25 min/gm	24 min/gm	46.15 min/gm	35.71 min/gm	29.41 min/gm	37.5 min/gm

From Table 3.6, it is noticed that trial 1 and 2 has 3 mm layers and created the highest cavity for the first layer. In these cases, sintered time per gram of sintered material is minimum compared to other trials. It shows that the cavity directly impacts sintered amount and thickness with sintering time for the same amount of irradiation at the same distance. Trials 3 to 6 would require more time to sinter the same amount of material.

This whole set of experiments does not provide comprehensive results, rather show some initial ideas that can be studied further.

3.5. Experiments with Cavity and Flux Distribution

From layer-by-layer sintering, it is noticed that cavities have a direct impact on sintering. To verify the finding, a set of experiments was designed with the cavity. From fixed focus experiments, it was noticed that while increasing the distance, the flux distributes over the top surface of the LHS-1 packed bed. Another set of experiments was designed following this phenomenon to distribute the irradiation over the whole top surface of the lunar soil simulant bed with constant heat flux to explore any improvement in the sintered amount and central thickness of the sintered lunar brick.

3.5.1. Experiments with Cavity

A 90 mm diameter circular calcium silicate insulator was machined internally to make a cylinder of 42 mm diameter with the exact height of the crucible, 25.5 mm. Then the cylindrical cavity was placed concentrically on top of the crucible filled with LHS-1 simulant, as shown in Fig. 3.30.

Figure 3.30. Concentric cavity over LHS-1

The experiments were conducted in two segments with the same heat flux, at first without the cavity and then with the cavity, so the results could be compared to see the difference found by experiments with the cavity. The experiments were run at three different

heat fluxes. At first, the current was set at 60 A, and with the help of the thermal imager and SiC plate, the heat flux was measured at 145.7 kW/m^2 for concentrated irradiation. The heat flux was measured with the average of the top surface temperature from multiple recordings. After measuring the heat flux, the experiment without a cavity was run. Three individual experiments were run, each for 40 minutes. Then the cavity was placed on top of the packed LHS-1 for another three sets of experiments. Sintered mass, central thickness, and maximum dimension were recorded in Table 3.7 for all six experiments.

Table 3.7. Experimental data without and with cavity for 145.7 kW/m^2 heat flux

	Without Cavity			With Cavity		
Trial	Mass (gm)	Thickness (mm)	Maximum Dimension (mm×mm)	Mass (gm)	Thickness (mm)	Maximum Dimension (mm×mm)
1	0.8	4.40	14.50 ×15.15	1.5	5.60	16.58×18.33
2	0.8	4.30	12.16×15.00	1.5	5.60	16.22×18.38
3	0.8	4.45	12.90×14.40	1.6	5.81	16.37×18.90
Avg.	0.8	4.38		1.53	5.67	

From Table 3.7, it is noticeable that the sintered mass and central thickness are similar for all three sets of experiments in both cases, so an average is calculated for discussion. Due to the cavity, the sintered mass and central thickness increased, and the maximum dimension of the sintered pieces also increased for the cavity. Similarly, two more sets of experiments are conducted at 178.5 kW/m^2 and 197.2 kW/m^2 heat flux. The average of three experiments for each configuration is taken, and the central thickness and sintered mass is then listed in Table 3.8.

Table 3.8. Results of experiments with cavity when irradiation is concentrated

Flux (kW/m²)	Without Cavity		With Cavity	
	Sintered Mass (gm)	Central Thickness (mm)	Sintered Mass (gm)	Central Thickness (mm)
145.701943	0.8	4.38	1.5	5.67
178.509748	1.5	6.01	2.5	6.99
197.1988399	2.5	7.39	3.7	8.50
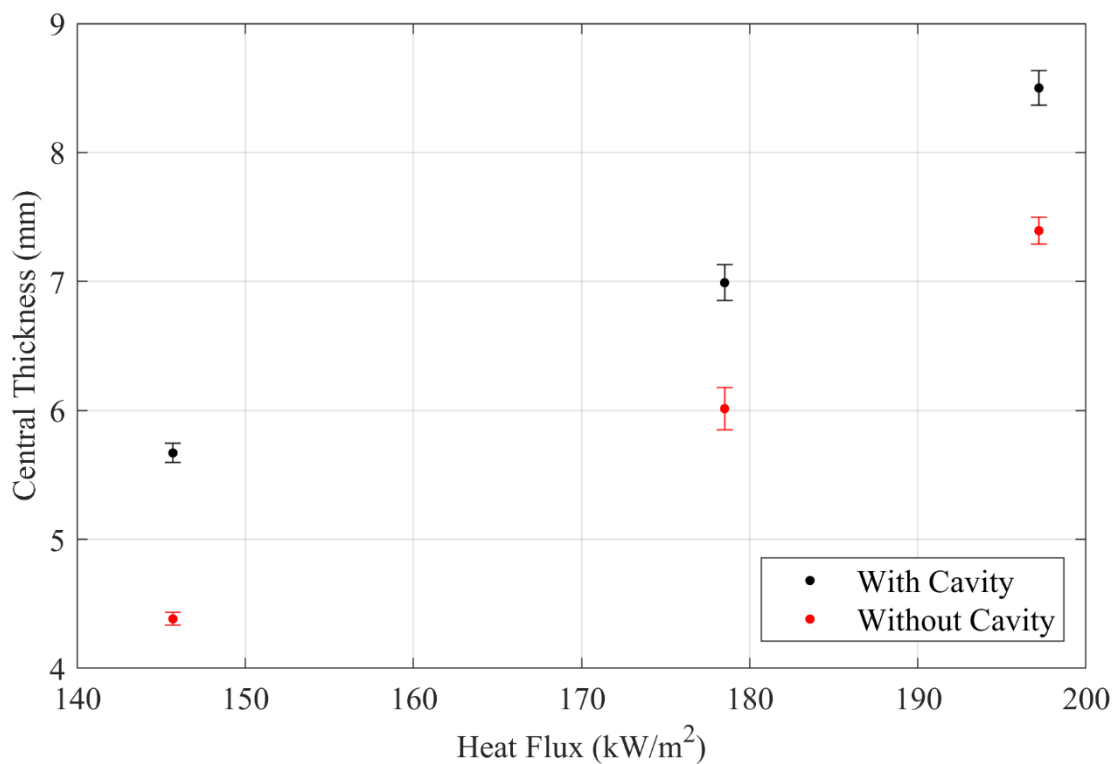
Figure 3.31. Central thickness of sintered LHS-1 for concentrated heat flux heated with and without cavity

In Fig. 3.31, the central thickness of sintered LHS-1 is plotted over the heat flux for concentrated irradiation. The trends with cavity and without cavity are linear, whereas the central thickness of cavity sintered bricks is higher with a margin over 1 mm than sintered bricks without a cavity. It is noticeable that the slopes for both trends are similar for all three data sets. Error for the average is also calculated. After getting the mean, each measurement's

deviation is calculated, squared, and added. Then the sum is divided by one less than the sample size. Taking the square root of the summation gives the standard deviation and dividing the standard deviation with the square root of the sample size gives the standard error [66]. The standard error is added with the measurement error 0.05 mm caused during measurement with slide calipers, the final error is calculated which is significantly low for all data sets, can be seen from the error bar in the plot.

From Table 3.7, it is seen that the sintered mass increased about twice with the cavity. Sintered mass over the heat flux of concentrated irradiation is also plotted in Fig. 3.32, where sintered with cavity and sintered without cavity both follow a similar trend but are not completely linear. With the cavity at higher heat flux, the slope of sintered mass is higher compared to without the cavity. The error is zero in three data points, whereas for other data points, the error is negligible, as seen in the plot.
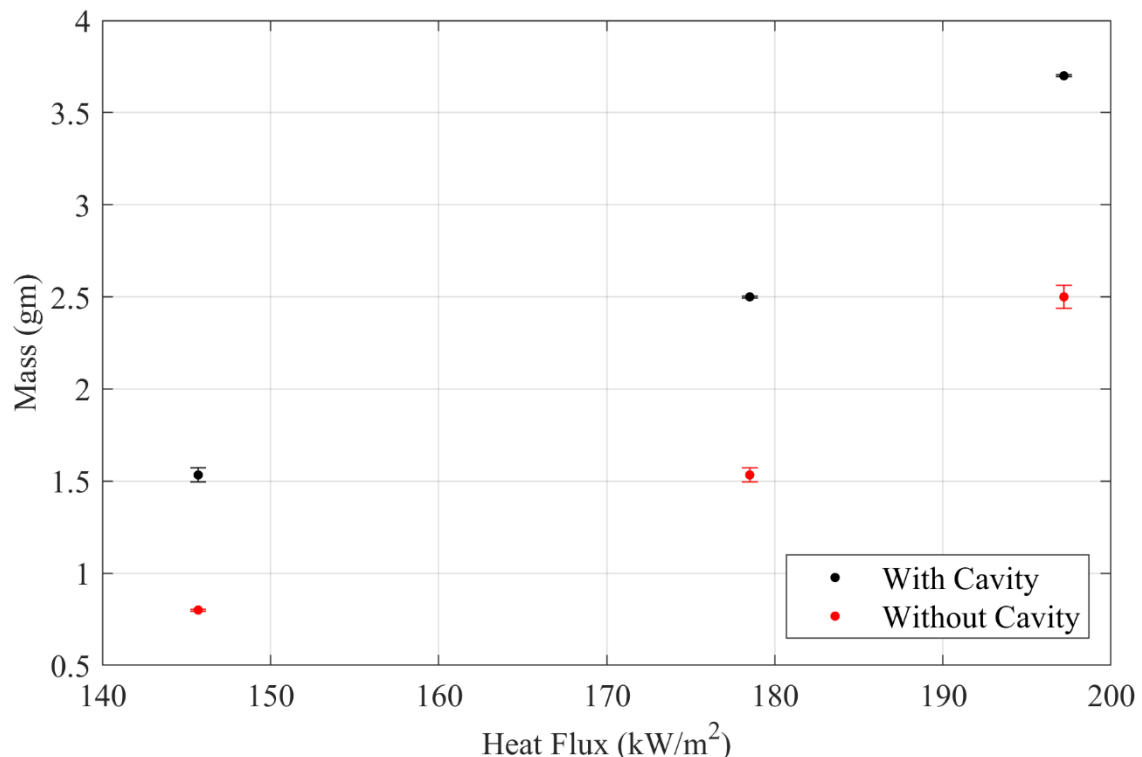
Figure 3.32. Mass of sintered LHS-1 with concentrated heat flux

3.5.2. Experiments with Flux Distribution
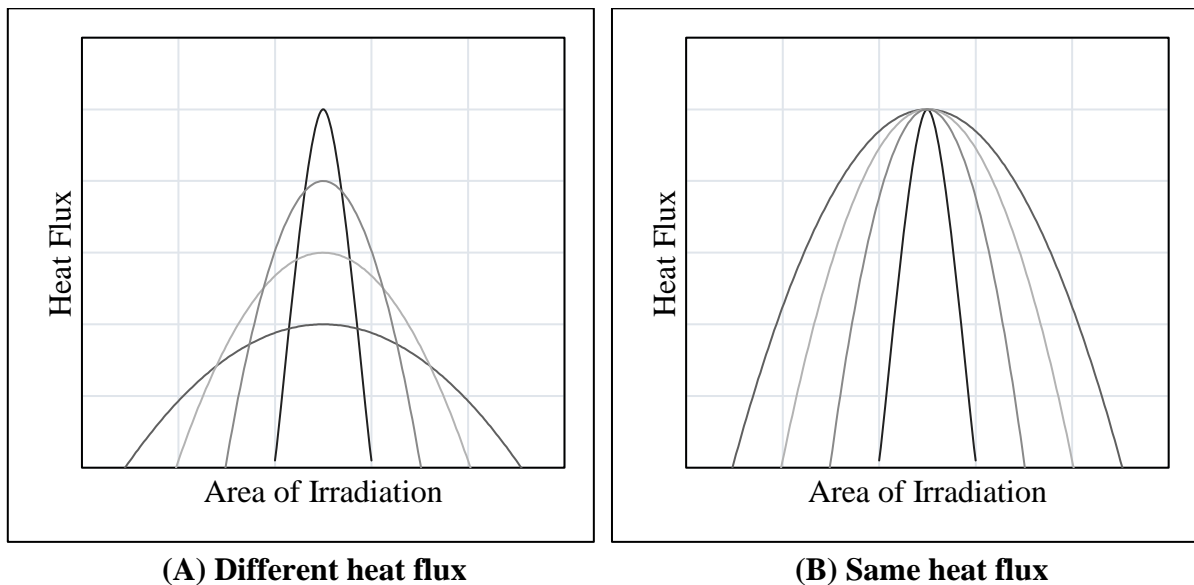
(A) Different heat flux   **(B) Same heat flux**
Figure 3.33. Area of irradiation with heat flux distribution (conceptual)

Theoretically the intensity of the same incoming irradiation reduces depending on the irradiation area, as shown in Fig. 3.33 (A). The more the irradiation is distributed, the lower the heat flux will be. During fixed focus experiments, while increasing the distance, the irradiation was spreading all over the top surface of the LHS-1 packed bed. While distributing the incoming irradiation, the heat flux reduced as shown in Fig. 3.33 (A). Since distributed irradiation covers a large area, an approach was taken, as shown in Fig. 3.33 (B), where the irradiation was distributed, but heat flux was kept the same for distributed irradiation by increasing the incoming energy. To do this experimentally higher input current was required. At first, by changing the focus, the incoming irradiation was spread all over the top surface of the LHS-1 lunar soil simulant bed. In the previous section, for concentrated irradiation, with 60 A current, a heat flux was achieved at the concentrated point. The input current was increased in distributed flux experiment to obtain the same heat flux all over the LHS-1 simulant bed. After distributing the incoming irradiation all over the LHS-1 particle bed, as shown in Fig 3.34, to obtain 145.7 kW/m^2 heat flux, the input current is increased to 74 A.
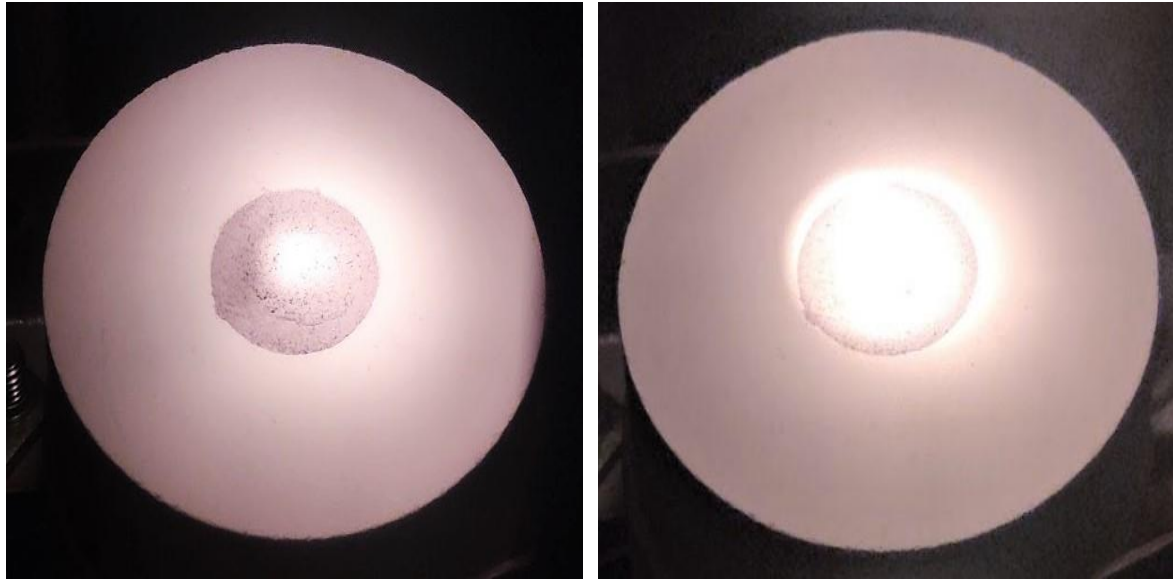
Figure 3.34. Concentrated and distributed irradiation over LHS-1 particle bed

Table 3.9 presents the comparative experimental data for 146 kW/m^2 heat flux for distributed irradiation for three individual sets of experiments, along with concentrated irradiation results from Table 3.6 without a cavity. An average is measured as before out of three experiments for discussion. It is noticeable that the maximum dimension is increased with a large margin due to the distribution of flux which increased the sintered mass and cross-section area of the sintered piece. The central thickness also increased.

Table 3.9. Data of concentrated and distributed irradiation for 145.7 kW/m^2 heat flux

Flux	Concentrated			Distributed		
Trial	Mass (gm)	Thickness (mm)	Maximum Dimension (mm×mm)	Mass (gm)	Thickness (mm)	Maximum Dimension (mm×mm)
1	0.8	4.40	14.50×15.15	2.6	7.03	19.63×22.10
2	0.8	4.30	12.16×15.00	2.7	6.86	19.84×21.60
3	0.8	4.45	12.90×14.40	2.5	6.85	19.15×21.33
Avg.	0.8	4.38	-	2.5	6.91	-

A similar result is found for 178.5 kW/m^2 and 197.2 kW/m^2 heat flux. The results of each experiment are quite identical; hence analysis is done by taking the average of the experiments. The average of all data sets is in Table 3.10.

Table 3.10. Results of experiments with concentrated and distributed irradiation

Flux Distribution	Concentrated		Distributed	
Flux (kW/m^2)	Sintered Mass (gm)	Central Thickness (mm)	Sintered Mass (gm)	Central Thickness (mm)
145.701943	0.8	4.38	2.5	6.91
178.509748	1.5	6.01	4.8	8.75
197.1988399	2.5	7.39	8.04	10.76
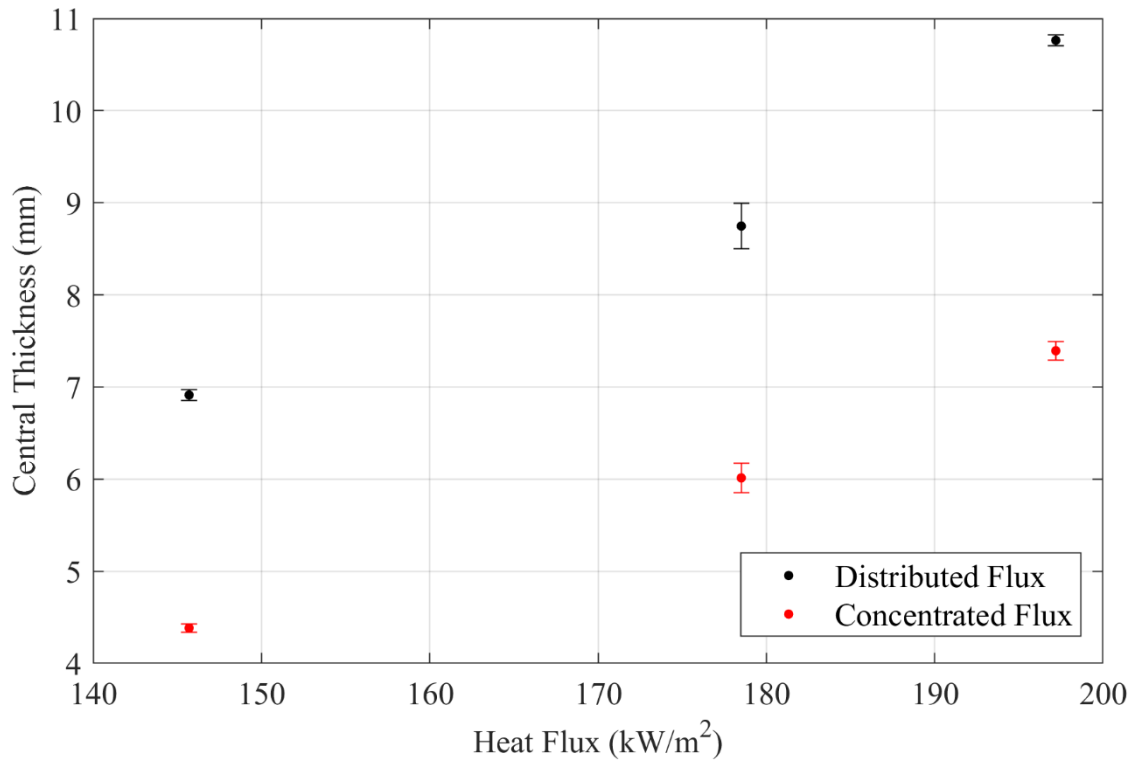
Figure 3.35. Central thickness with flux for concentrated and distributed irradiation
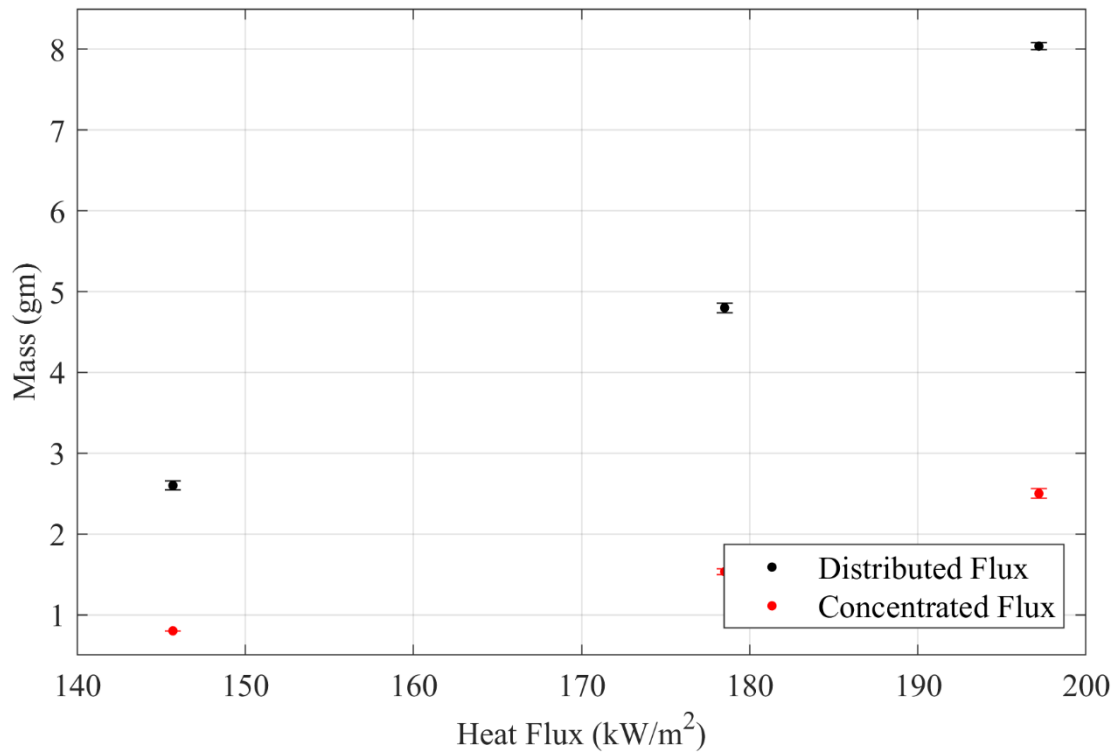
Figure 3.36. Sintered mass with flux for concentrated and distributed irradiation

From Fig 3.35, it is visible that the increment of the central thickness of sintered LHS-1 bricks with increased heat flux is non-linear. The thickness increased more than 150% by distributing the irradiation all over the lunar soil simulant bed. The increment of thickness is even greater and increased over 300% with increasing flux. Fig. 3.36 shows the increment of sintered mass with increased heat flux. The increase in mass is greater than central thickness due to poor heat conduction of lunar soil simulant that prevents heat to conduct in higher depth. Both trends are exponential, whereas the trend of distributed flux has a higher power of exponential. It is noticeable that the difference in sintered mass for concentrated and distributed irradiation gradually increases with increasing heat flux. The more the heat flux is, the more sintered material will be achieved with distributed irradiation compared to concentrated irradiation.

Table 3.11. Comparison of differently sintered LHS-1 lunar bricks at 146 kW/m^2 heat flux

Flux Type	Cavity	Sintered Mass (gm)	Central Thickness (mm)
Concentrated	Without	0.8	4.38
	With	1.5	6.01
Distributed	Without	2.5	7.39
	With	4.8	9.25

(a)   (b)   (c)   (d)
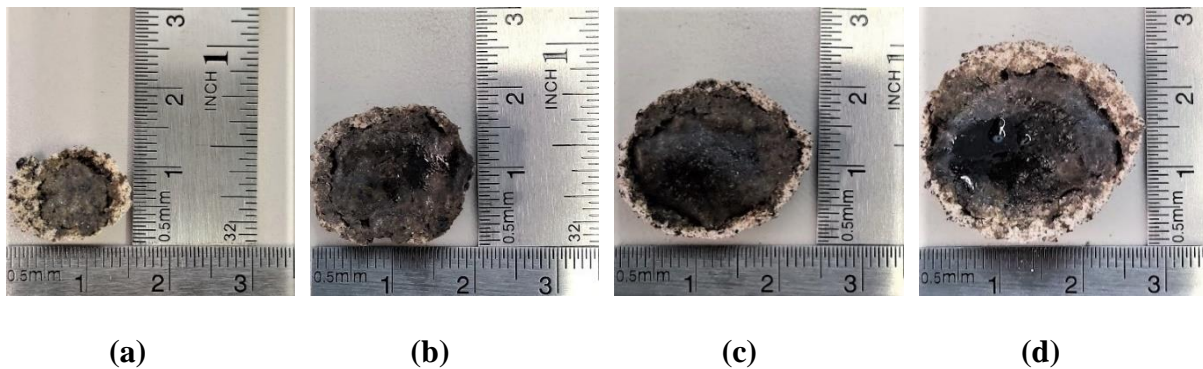
Figure 3.37. (a) Concentrated without cavity, (b) Concentrated with cavity,

(c) Distributed without cavity, and (d) Distributed with cavity

Table 3.11 compares sintered mass and central thickness of sintered LHS-1 samples with 146 kW/m^2 heat flux. Fig. 3.37 shows the sintered bricks of the configuration presented in Table 3.11. The tables and figures show the increment of size at the same heat flux but with different heating configurations. It is proved that distributed irradiation with cavity gives the most sintered LHS-1. One concern to remember is that cavity increases melting, which might make the sintered samples structurally poor. A distributed irradiation with controlled heat flux may give a wholly sintered lunar soil simulant with good structural characteristics.

3.6. Sintering Behavior of LHS-1 and JSC-1A Lunar Soil Simulant

This experiment set compares the sintering behavior of two different lunar soil simulants, LHS-1 and JSC-1A. The previous section shows that distributed flux with cavity

sinters the maximum amount of lunar soil simulant for any specific heat flux whereas, experiments with the cavity sometimes melts the simulant, which is not desired. In addition, sintering with a cavity is a more complex process than sintering without a cavity. Therefore, this set of experiments is conducted with the second-best configuration, sintering with distributed irradiation without a cavity. Both the samples are sintered with the same heating configuration consecutively. The focus of this experiment is to find the efficient time of sintering for both LHS-1 and JSC-1A and compare the thermal behavior and properties.

3.6.1. Time Series Experiments

Till now, the experiments were conducted until the system temperature reached a steady state. A time-based sintering experiment was designed to find the impact of time on the sintering of lunar soil simulant. With the same heating condition, lunar soil simulant was sintered for different time duration. This experimental set gave the mass of sintered material for different experiment time duration and the rate of sintered mass with time. The experiment was conducted with both LHS-1 and JSC-1A lunar soil simulants. Therefore, a comparative sintered mass and central thickness with time, along with the rate of sintering, was found.

(A)   (B)
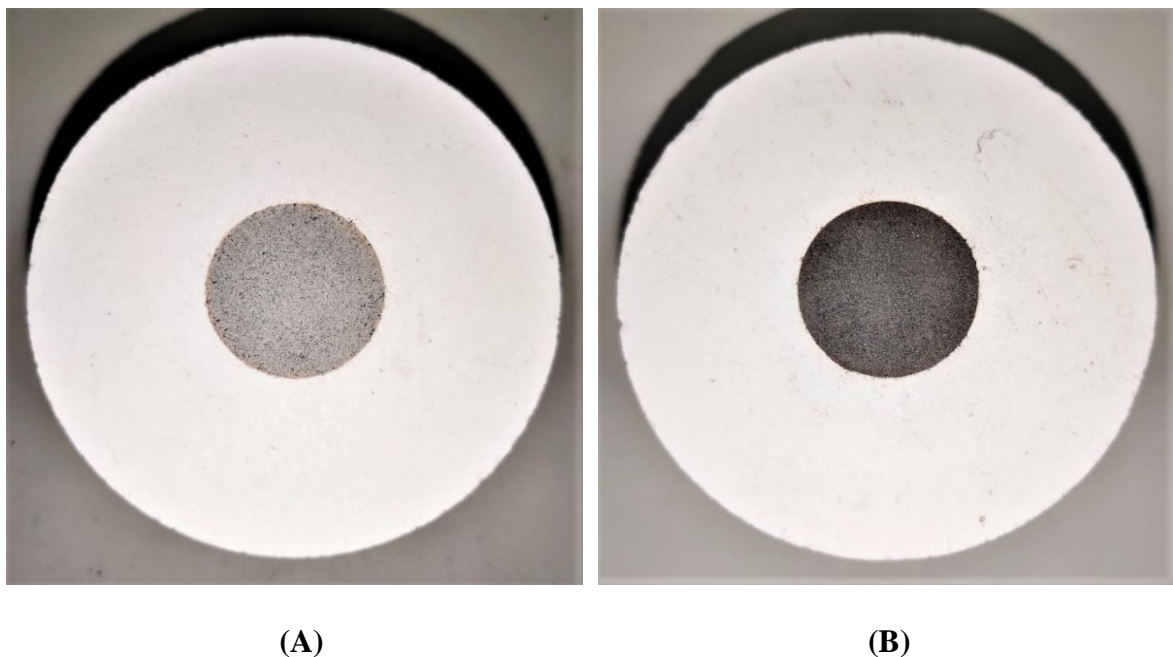
Figure 3.38. (A) LHS-1 and (B) JSC-1A lunar soil simulant beds inside crucible

At first, the required heat flux was measured at which the experiments would be conducted. The heat flux was fixed with distributed flux for sintering. Then lunar soil simulant was measured and poured inside the crucible. After filling them appropriately inside the crucible, as shown in Fig 3.38, the lunar soil simulant bed was placed in the crucible stand for the sintering of the lunar soil simulant.

The initial flux was chosen as 105 kW/m^2, the lowest value at which LHS-1 was sintered. At the beginning of the experiment set, individual experiments were run for 1 min, 2 min, 3 min, and up to 10 min at 105 kW/m^2 heat flux. Then the separate experiments continued with 5 minutes intervals until the amount of sintered material did not increase significantly. For 105 kW/m^2 heat flux, the final experiment was run for 20 minutes. At 20 minutes the increment of sintered mass and central thickness did not increase much compared to 15 minutes. Since the increment reduced, resulting steady result of sintered mass and central thickness, experiment was not conducted for more than 20 minutes. The investigation was conducted for both LHS-1 and JSC-1A lunar soil simulant. Table 3.12 presents the experimental data for 105 kW/m^2 heat flux configurations when the irradiation was distributed at the focal point. For this case, 12 individual experiments were run until the increment of sintered mass and central thickness became small. The next sets of experiments were conducted for 150 kW/m^2 heat flux and 190 kW/m^2 heat flux. For 150 kW/m^2 heat flux, the final experiment was run for 25 minutes, and, for 190 kW/m^2 heat flux, the final experiment was conducted for 30 minutes.

Fig. 3.39 presents the central thickness over time for all three fluxes configurations. It is noticeable that the increase of central thickness is rapid for the first 10 minutes. However, the slope is higher for higher heat flux. After 10 minutes, the increment slows down with time, and the thickness does not increase significantly. A similar trend is seen in Fig. 3.40, where the sintered mass is plotted over time. A critical difference in Fig. 3.39 is that, at the beginning of

sintering, the thickness of sintered JSC-1A is higher than LHS-1, but later, the thickness of LHS-1 becomes more than JSC-1A.

Table 3.12. Time series experimental data of LHS-1 and JSC-1A sintered lunar bricks at 105 kW/m^2 heat flux

Time	Mass (gm)		Thickness (mm)		Maximum Dimension (mm)			
(min)	JSC-1A	LHS-1	JSC-1A	LHS-1	JSC-1A		LHS-1	
0	0	0	0	0	0	0	0	0
1	0.13	0	1.15	0	13.4	8.75	0	0
2	0.27	0	1.46	0	15.43	12.37	0	0
3	0.44	0.11	1.77	1.41	17.13	13.23	9.60	8.28
4	0.55	0.16	2.19	2.01	18.2	14.32	11.30	9.65
5	0.64	0.20	2.22	2.11	18.14	15.22	12.70	10.11
6	0.73	0.23	2.42	2.18	18.57	15.00	12.60	11.23
7	0.75	0.27	2.49	2.27	19.00	15.31	13.50	10.80
8	0.85	0.32	2.63	2.34	19.40	15.73	14.70	12.23
9	0.85	0.32	2.69	2.42	19.18	15.5	14.30	11.54
10	0.85	0.32	2.75	2.57	18.55	15.34	14.40	11.23
15	0.97	0.40	2.95	2.94	19.76	15.76	14.70	12.95
20	0.99	0.51	3.02	3.30	19.42	15.43	15.70	13.23
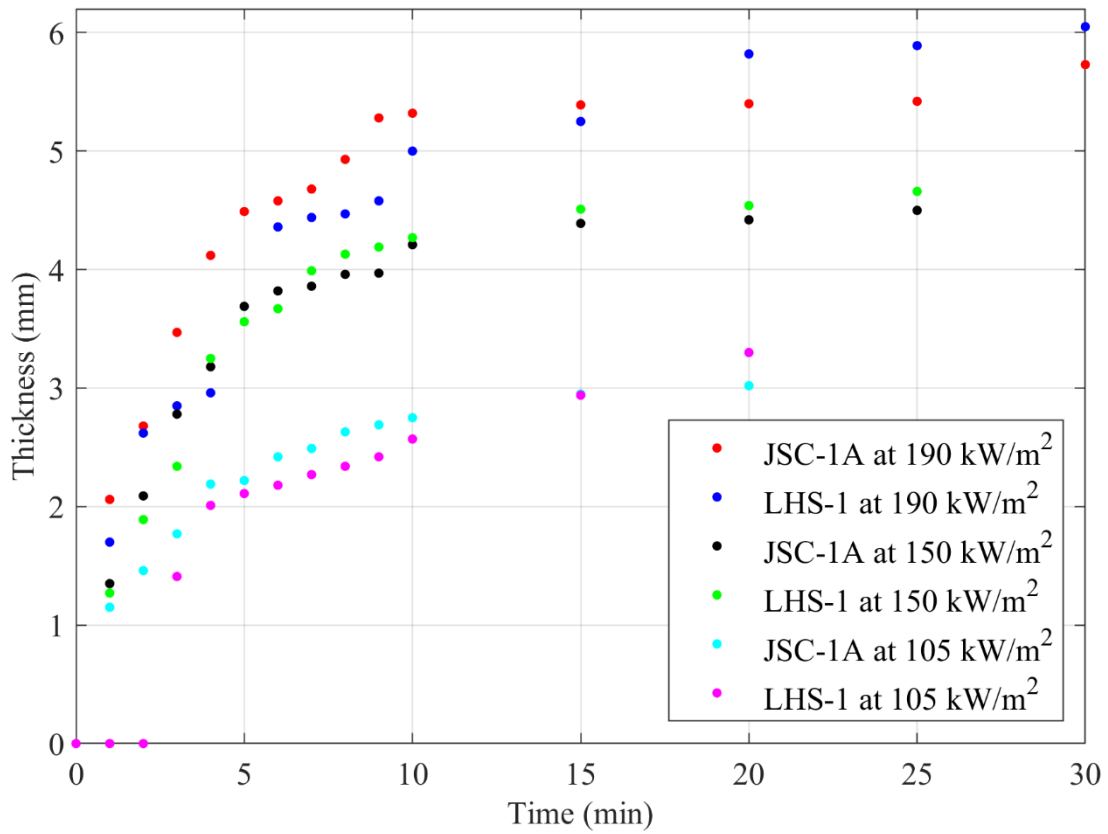
Figure 3.39. Central thickness with time at different heat flux
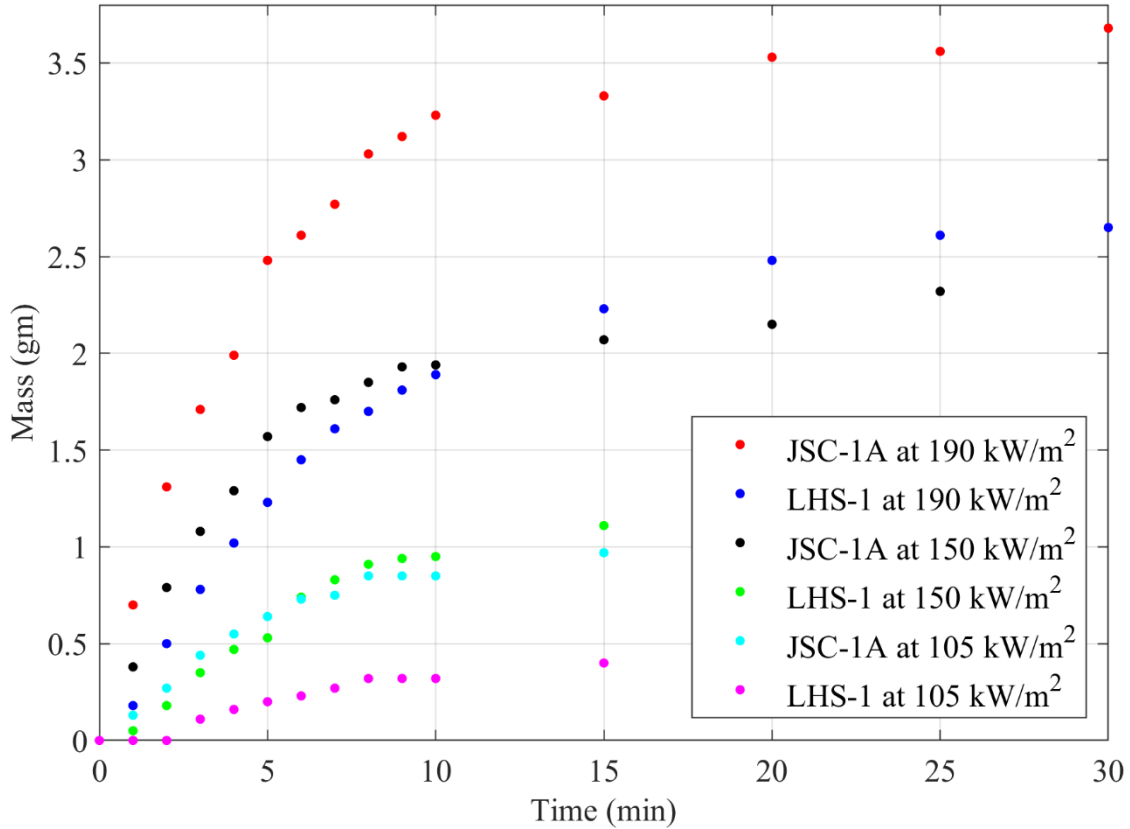
Figure 3.40. Sintered mass with time at different flux
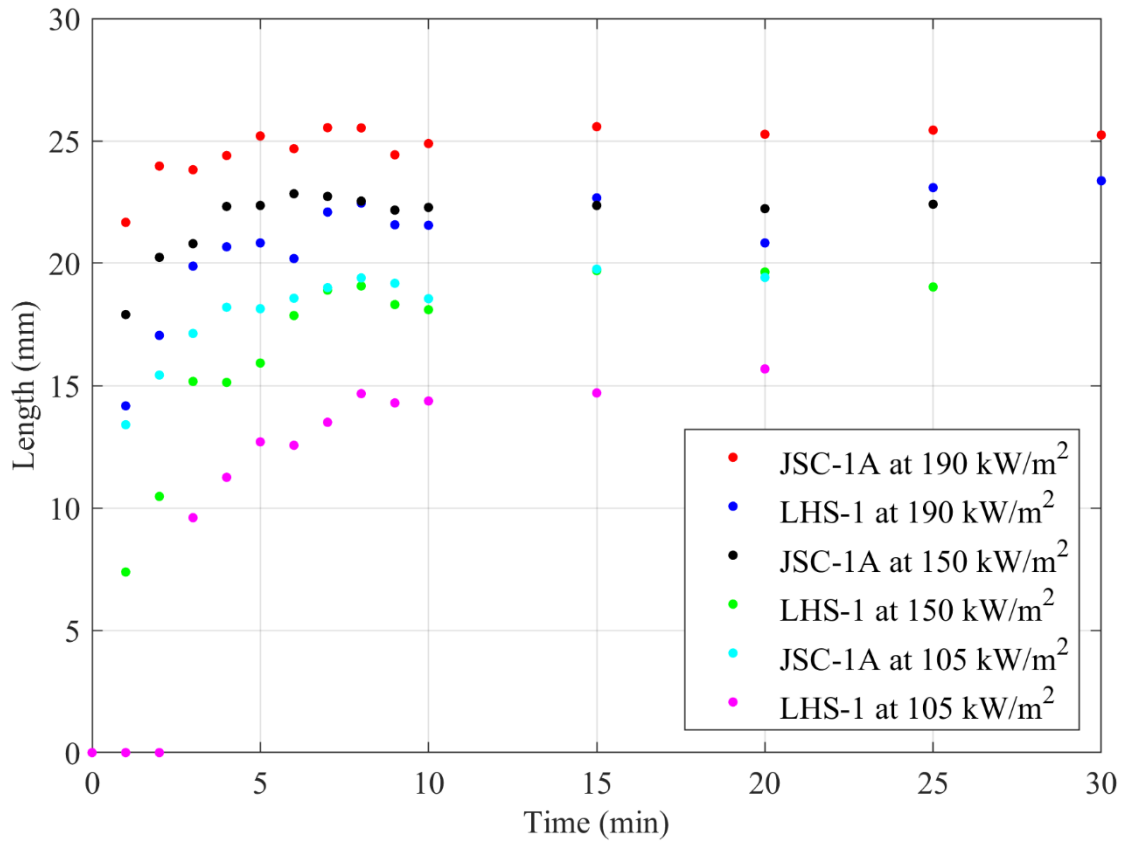
Figure 3.41. Sintered length with time at different flux
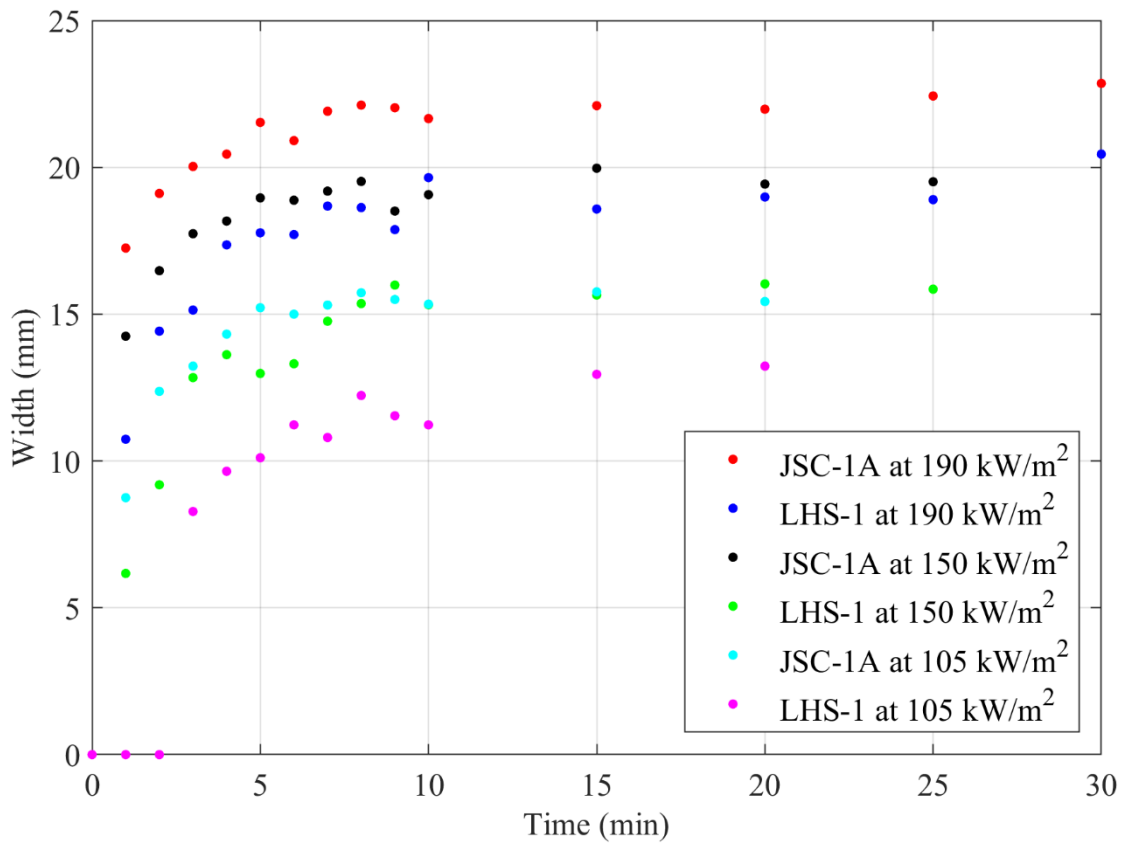
Figure 3.42. Sintered width with time at different flux

In Fig 3.41 and Fig 3.42, it is visible that the length and width of the sintered lunar bricks grow up to a specific time until the top surface area sinters which are the same as the area of incoming irradiation. After that, the length and width do not increase significantly, only the thickness increases. It is also noticeable from the figures that, at higher heat flux, the whole top surface sinters faster than at lower heat flux operation.
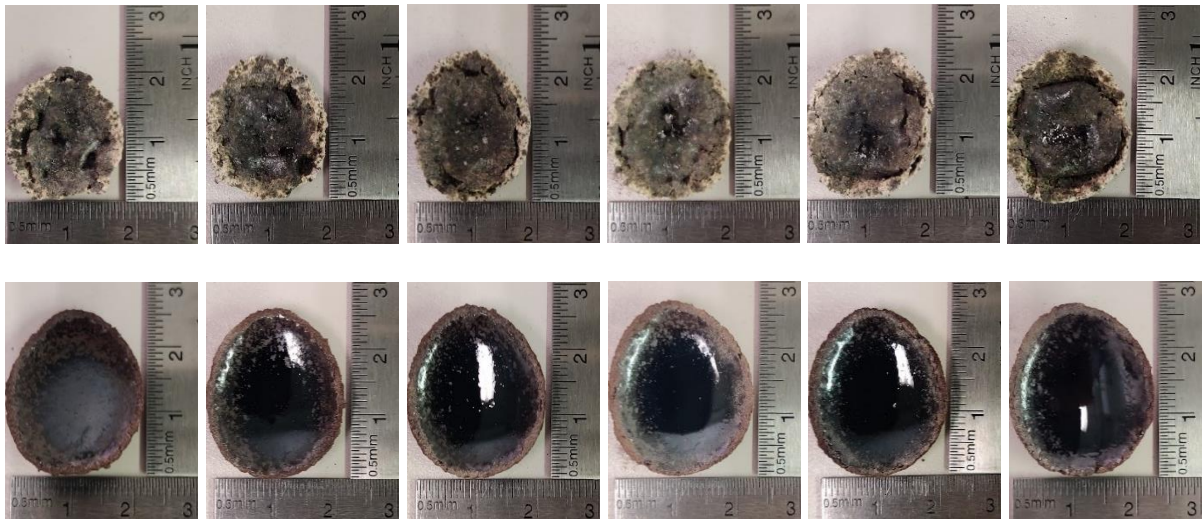
Figure 3.43. Evolution of sintered samples in 5, 10, 15, 20, 25, and 30 minutes

for LHS-1 and JSC-1A at 190 kW/m^2 heat flux

Fig. 3.43 shows the evolution of LHS-1 and JSC-1A at 190 kW/m^2 Heat Flux. From the images, it is visible that the dimension does not increase significantly after a specific time, but the thickness increases as well as the structure changes. In LHS-1, balling occurs at higher heat flux and increases with time, whereas for JSC-1A, no balling phenomena are noticed. The larger grain size of LHS-1 compared to JSC-1A affect the balling. Larger grain size makes poor inter-line bonding which can form discontinuous track of molten region and creates balling [66]. In addition, JSC-1A is darker in color than LHS-1, making JSC-1A more heat-absorbent than LHS-1. Therefore, the effective thermal conductivity is higher in JSC-1A. In contrast, low thermal conductivity in LHS-1 prevents heat from conducting inside the bed and creates a boundary between hot and cold layers to form balls. Since JSC-1A absorbs and conducts more heat, and due to finer grain size, no boundary between layers occurs to create balls. It is also

noticeable that the top surface of JSC-1A turns glacial with time. This could occur due to finer grain size and bonds between grains which need to be explored. The concave shape in the JSC-1A simulant is also noticed.

3.6.2. Difference in Sintering Behavior for LHS-1 and JSC-1A

From the time series data, it is noted that after 10 minutes, the sintered mass and central thickness do not increase significantly. Within this timeframe, a big chunk of lunar brick can be sintered. Since balling phenomenon occurs for LHS-1, and JSC-1A starts the melting phase early, a 50% mixture of both is also investigated to find the change in properties.

In this case, for all three samples, each experiment was run for 10 minutes. The heat flux was chosen as 120, 140, 160, 180, and 200 kW/m^2. Three individual experiments were run for each configuration and sample, and the average of the sintered mass and central thickness were calculated for analysis. Table 3.13 presents the experimental data for LHS-1, Mix, and JSC-1A lunar soil simulant at 120 kW/m^2 heat flux.

Table 3.13. Experimental data for LHS-1, mixed (50% LHS-1 and 50% JSC-1A), and JSC-1A lunar soil simulant at 120 kW/m^2 heat flux

Simulant	JSC-1A		Mix		LHS-1	
Trial	Mass (gm)	Thickness (mm)	Mass (gm)	Thickness (mm)	Mass (gm)	Thickness (mm)
1	1.08	3.2	0.68	2.6	0.35	2.24
2	0.92	2.84	0.73	2.5	0.31	2.57
3	1.01	3	0.67	2.4	0.32	2.6
Avg.	1.003	3.01	0.693	2.5	0.327	2.47

The central thickness is plotted against the heat flux in Fig 3.44. It is prominent that all three trends are linear. It is noticed earlier in Fig. 3.39 that the central thickness of LHS-1

increases with increased heat flux. Hence, the slope of the thickness trend here is higher for LHS-1 than JSC-1A, which increased notably at higher heat flux. The error is also relatively higher for higher heat flux.

From Fig. 3.45 (A), it is seen that for 200 kW/m^2, the top surface of sintered JSC-1A is concave, whereas the top surface of sintered LHS is slightly convex due to balling. This happens with higher heat fluxes. The central thickness was measured from the center of the sintered samples. This different structure at higher heat flux created the difference in thickness and sintered LHS-1 became thicker than JSC-1A at the center. However, during indentation at higher heat flux, the distance between the top surface of JSC-1A and the focal point of incoming irradiation increases, which might impact further sintering with time. From Fig 3.45 (B), it is noticeable that the size of sintered JSC-1A is larger than LHS-1, which is reflected in the trend of Fig 3.46.
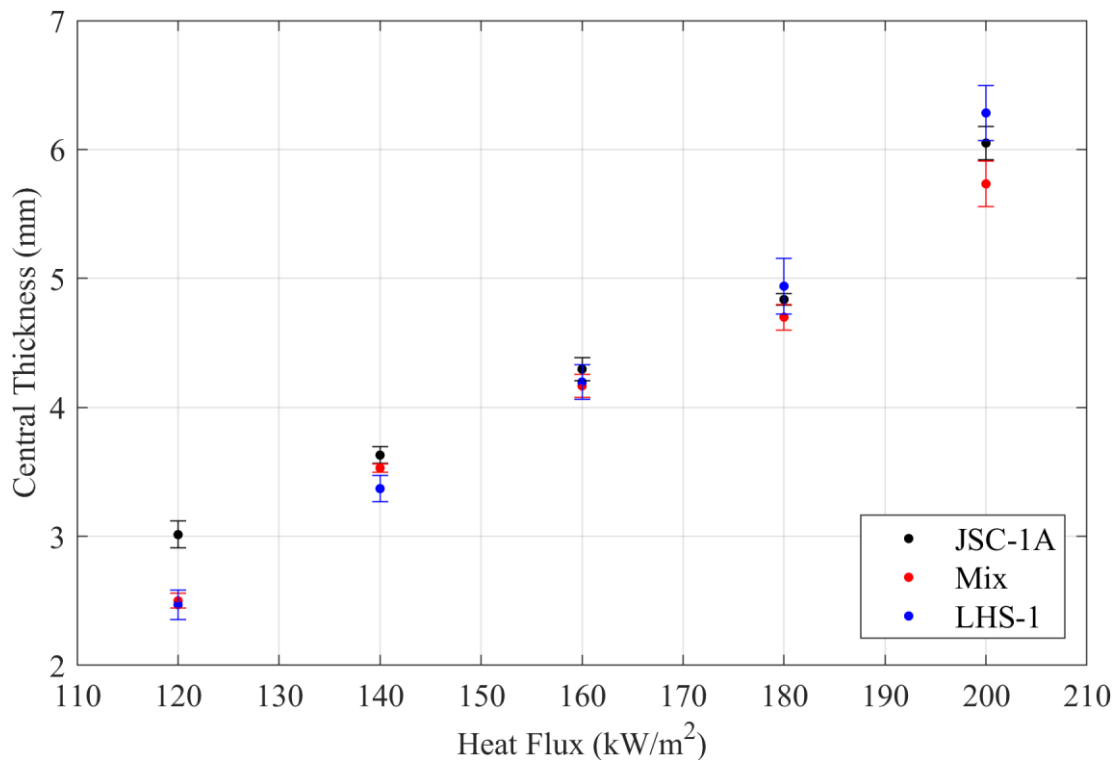
Figure 3.44. Central thickness with heat flux

(A)   **(B)**
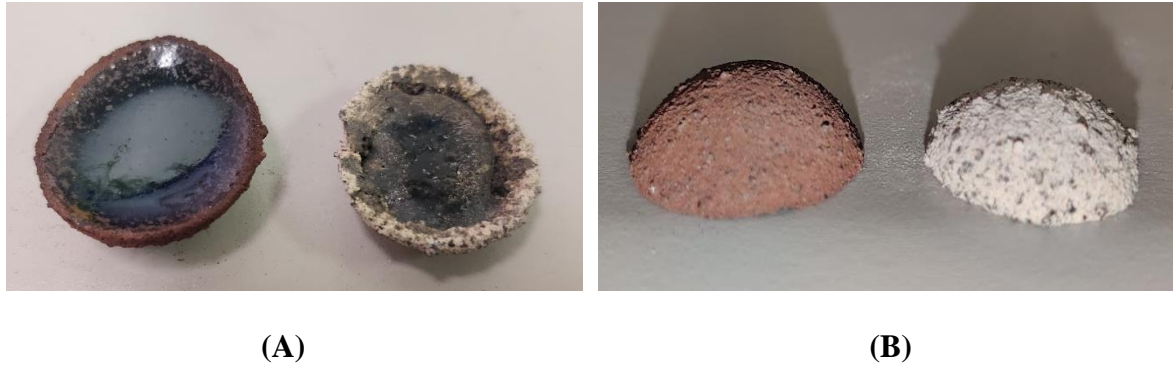
Figure 3.45. Central thickness comparison of JSC-1A and LHS-1 at 200 kW/m² flux

In Fig. 3.46, the sintered mass is plotted over the heat flux. Here all three samples follow a non-linear trend where sintered mass increases with heat flux. The increment of JSC-1A is higher than the other two samples. Since the mass of sintered material is more for JSC-1A, the increased distance due to indentation at the center did not reduce the mass of sintered material at higher heat flux.
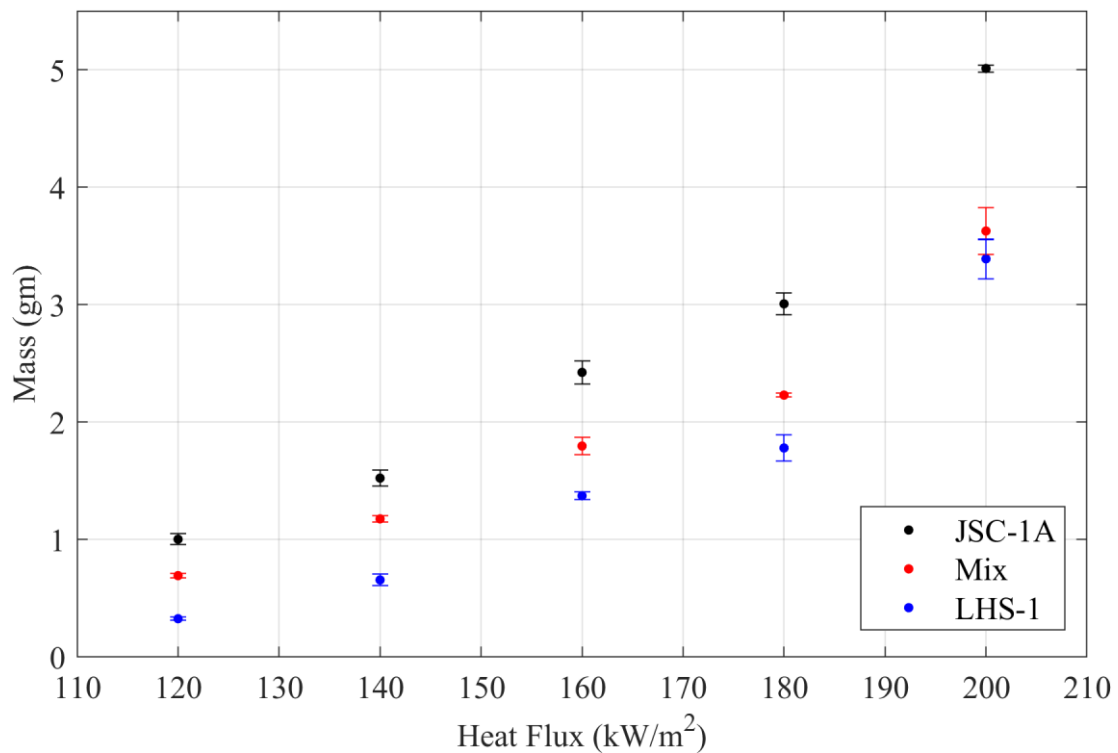
Figure 3.46. Sintered mass with heat flux

Table 3.14. Sintered samples of LHS-1, mixed (50% LHS-1 and 50% JSC-1A), and

JSC-1A lunar soil simulant with different heat flux
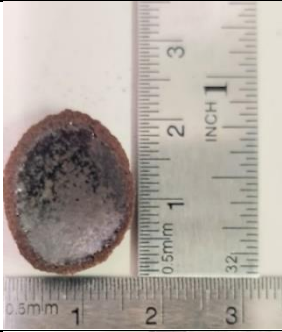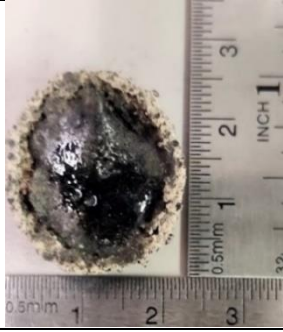
Heat Flux	LHS-1	Mix	JSC-1A
120 kW/m^2			
140 kW/m^2			
160 kW/m^2			
180 kW/m^2			
200 kW/m^2			

Table 3.14 presents all the samples sintered with different configurations. Horizontally the difference in the size and top surface structure of sintered pieces for all three samples is visible at the overmentioned specific heat flux. Vertically, the evolution of each type of sintered lunar soil simulant with increasing heat flux is noted. It is seen that both the length and width increase with increased heat flux through the irradiation, hitting the same amount of surface area. This happens because, at higher heat flux, more heat is transferred sidewise, which takes more surface area to sintering temperature. Since JSC-1A is more heat absorbent and heat conductive than LHS-1, the temperature of the lunar soil simulant bed increases both inwards and sidewise to sinter larger pieces of lunar brick compared to LHS-1 samples. With increased heat flux, the top surface structure changed. LHS-1's evolution from sintering to melting with ball formation is noticed where the surface is rough. With increasing heat flux, the concave shape started to be prominent for the mixed lunar soil simulant, but the surface is rough to represent the presence of LHS-1. For JSC-1A, the surface becomes concave with increased heat flux, and the surface is smooth and glacial compared to the other two samples.

CHAPTER 4

INDIRECT SINTERING

The idea of indirect sintering follows the need to sinter large and uniformly thick lunar bricks. A material with high thermal conductivity can uniformly distribute the heat from concentrated irradiation over the top surface of the lunar soil simulant. In the following experiments, indirect heating is applied only on the top surface of the lunar soil simulant bed. Experimental findings can be used to inform the construction of molds to sinter complex shaped lunar bricks based on requirements. The uniformity of the top surface temperature maintained by the high heat conductive intermediate material helps maintain constant heat flux over the top surface. For this purpose, a silicon carbide (SiC) plate is used. The size of the SiC plate is 20 mm × 20 mm, and the thickness of the plate is 2 mm. Manufacturer specifications list the material to have a thermal conductivity of 130 W/m·K at 25°C and an emissivity of 0.9.
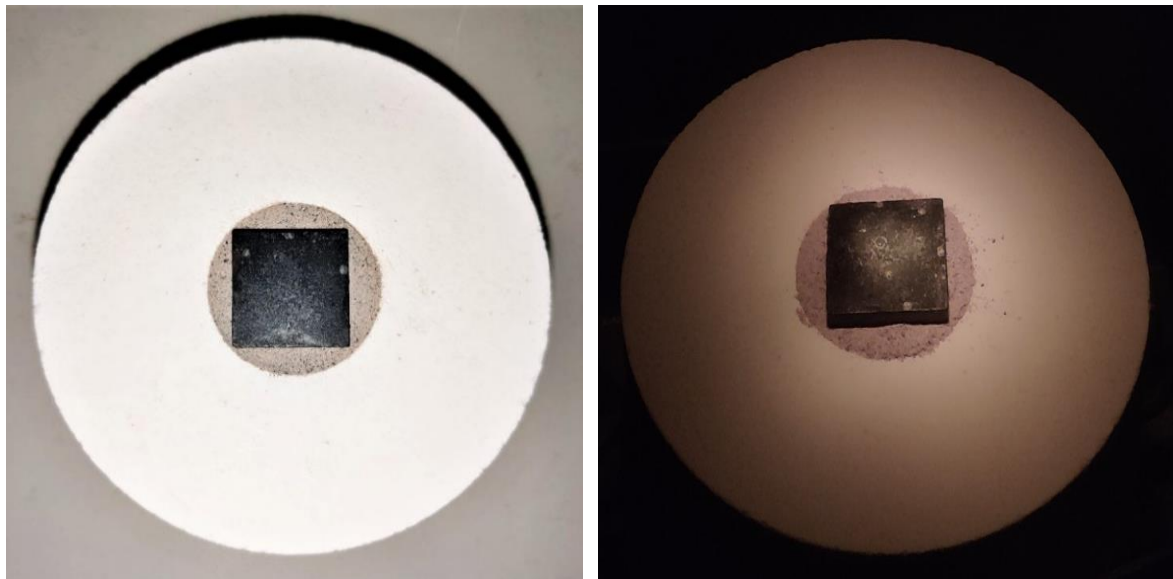
(A)   (B)

Figure 4.1. Lunar soil simulant bed with SiC for indirect sintering

(A) Shutter closed and (B) Shutter open

For all indirect sintering experiments, LHS-1 lunar soil simulant was used. The investigation was conducted following the same procedure as direct sintering. First, 30 gm of

LHS-1 was measured, poured, and compressed inside the crucible. Then the SiC plate was placed on top, as shown in Fig 4.1 (A). The crucible was then placed on the crucible holder for the experiment. Three thermocouples were set at 2 mm, 6 mm, and 10 mm beneath the top surface as done in direct sintering. The concentrated irradiation was focused on the center of the SiC plate as Fig 4.1 (B) to spread the heat all over the top surface.

4.1. Initial Experiments with SiC Plates while Adjusting Focus

For the first indirect experiment set, the input current was set at 60 A. The focus was continuously varied to concentrate the irradiation for this set of experiments to obtain the maximum amount of sintered material at each distance. Since the sintering configuration was unknown, the investigation started from 100 mm distance. This is the distance where 0.9 gm of sintered lunar brick is achieved during varying focus direct sintering experiments. The distance was reduced by 5 mm each time and each experiment was run for 50 minutes.

From 100 mm distance to 55 mm distance, no sintering was recorded. At 50 mm distance, negligible amount of LHS-1 was sintered, which was then attached to the SiC plate, as shown in Fig 4.2 (A). At 45 mm distance, the mass of sintered material was less than 0.1 gm, but the grains were sintered together and stuck with the SiC plate. At 40 mm distance, 0.1 gm of lunar soil simulant was sintered through indirect sintering, shown in Fig 4.2 (B).

Up to 30 mm distance, it was impossible to detach the sintered LHS-1 from the SiC plate without breaking due to its smaller size and low strength. At 25 mm distance, over 0.3 gm of material was sintered and was successfully detached without breaking the sintered lunar brick, as shown in Fig 4.2 (C). With the reduction of height, the heat flux increased, and more LHS-1 was sintered. At 0 mm distance, a maximum of 1.3 gm of sintered material was achieved with a thickness of 3 mm, as shown in Fig 4.2 (D).

Figure 4.2. Indirectly sintered LHS-1 at (A) 50 mm, (B) 40 mm, (C) 25 mm and

(D) 0 mm distance for 60 A current input

Table 4.1 records the top thermocouple temperature for all the experiments after 50 minutes. The top thermocouple steady state temperature is also noted, along with the sintered mass and central thickness.

Table 4.1. Experimental data of indirect sintering experiments at 60 A current and adjustment of focus

Distance (mm)	Top Thermocouple Steady State Temp (°C)	Steady State Time (min)	Sintered Mass (gm)	Central Thickness (mm)
100	900.05	24:47:00	-	-
95	916.09	26:43:00	-	-
90	951.04	27:36:00	-	-
85	952.02	24:30:00	-	-
80	962.01	24:31:00	-	-
75	928.00	34:00:00	-	-
70	926.00	22:55:00	-	-
65	960.01	27:53:00	-	-
60	967.01	23:25:00	-	-
55	976.02	24:51:00	-	-
50	996.05	20:09:00	> 0	-
45	1018.10	28:13:00	> 0	-
40	1039.08	22:20:00	0.1	-
35	1032.02	25:18:00	0.1	-
30	1066.08	30:56:00	0.2	-
25	1071.00	25:20:00	0.3	1.0
20	1175.08	25:39:00	0.9	2.5
15	1113.07	23:25:00	1.1	2.8
10	1082.02	20:18:00	1.1	2.9
5	1107.05	22:58:00	1.2	3.0
0	1155.96	25:05:00	1.3	3.0
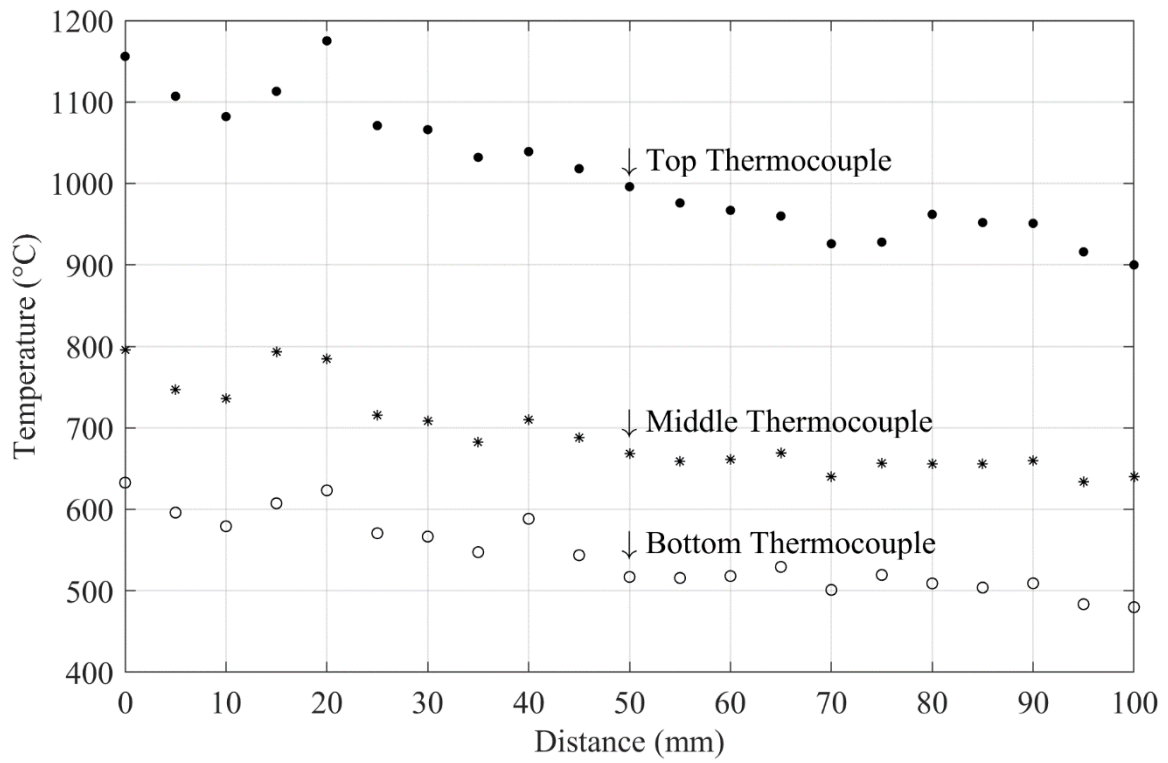
Figure 4.3. Variation of steady state temperature over distance
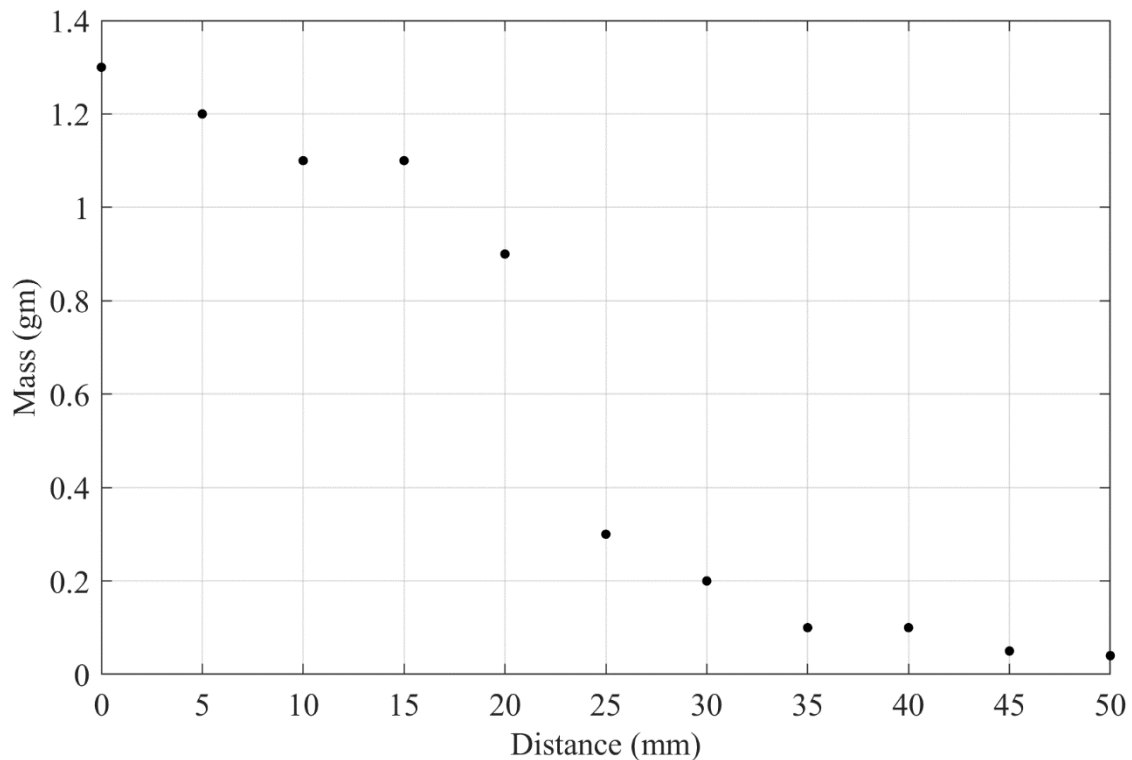
Figure 4.4. Variation of sintered mass with distance

Fig. 4.3 shows that; the middle and bottom thermocouples follow the trend of top thermocouple temperature. The top thermocouple steady state temperature for distances 0 mm

to 15 mm is not behaving as expected. Inappropriate variation of the focus could be a reason behind this. If the irradiation at 20 mm distance is concentrated, then reducing the distance would distribute the irradiation. Therefore, if the focus is not concentrated at these smaller distances, a lower top thermocouple steady state temperature compared to 20 mm distance would happen. There is a temperature drop after 15 mm distance, whereas the temperature is expected to go up until 0 mm distance. The mass of sintered material is also not uniform, as shown in Table 4.1 and Fig. 4.4.

4.2. Experiment with SiC Plate Without Adjusting the Focus

Unlike the previous section, this set of experiments was designed with fixed focus, like fixed focus direct sintering experiments. Since the sintering zone was known for 60 A current from the previous set, the first experimental set was run for 60 A current.

Table 4.2. Experimental data of indirect sintering experiments at 60 A current with fixed focus

Distance (mm)	Top Thermocouple Temperature(°C)	Steady State Temperature of Top Thermocouple (°C)	Steady State Time (min)	Sintered Mass (gm)	Central Thickness (mm)
25	1034.07	1021.02	24:34:00	0.2	1.55
20	1029.64	1021.00	30:00:00	0.2	1.69
15	1066.91	1056.02	26:09:00	0.3	2.09
10	1111.43	1100.01	27:50:00	0.4	2.01
5	1106.96	1101.07	43:12:00	0.4	2.32
0	1091.52	1078.03	26:59:00	0.5	2.39

For fixed focus, the experiment started at the focal point, and with a 5 mm increment each time, sintering was conducted up to 25 mm distance from the focal point. Each experiment

was run for 50 minutes. The three thermocouples' temperature reading with the sintered mass and central thickness were recorded in Table 4.2.
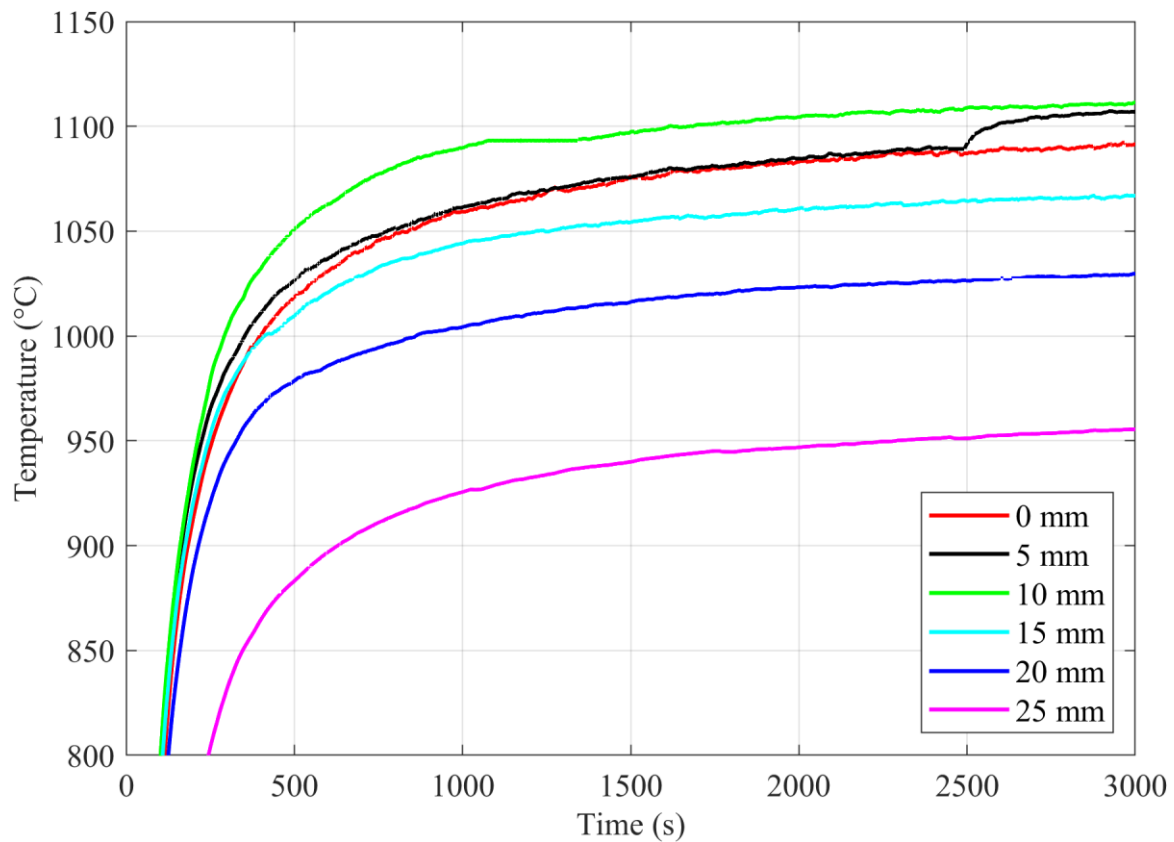
Figure 4.5. Top thermocouple steady state temperature profile for 60 A input current during indirect sintering

From Fig. 4.5, a uniform top thermocouple temperature profile is noticed. The temperature profile for 0 mm, 5 mm, and 10 mm did not behave as expected. The top temperature profile for 0 mm distance was expected to be the highest temperature of all the profiles, but it is below the temperature profile of 5 mm and 10 mm distance. Also, the temperature profile of 10 mm distance goes over the temperature profile of 5 mm distance. An unusual temperature jump for 5 mm distance is also noticed after 41 minutes.

The steady-state temperature was recorded for all three thermocouples, which shows a similar trend in Fig 4.6. The increased steady-state temperature is noticed with reduced height and increased solar irradiation.
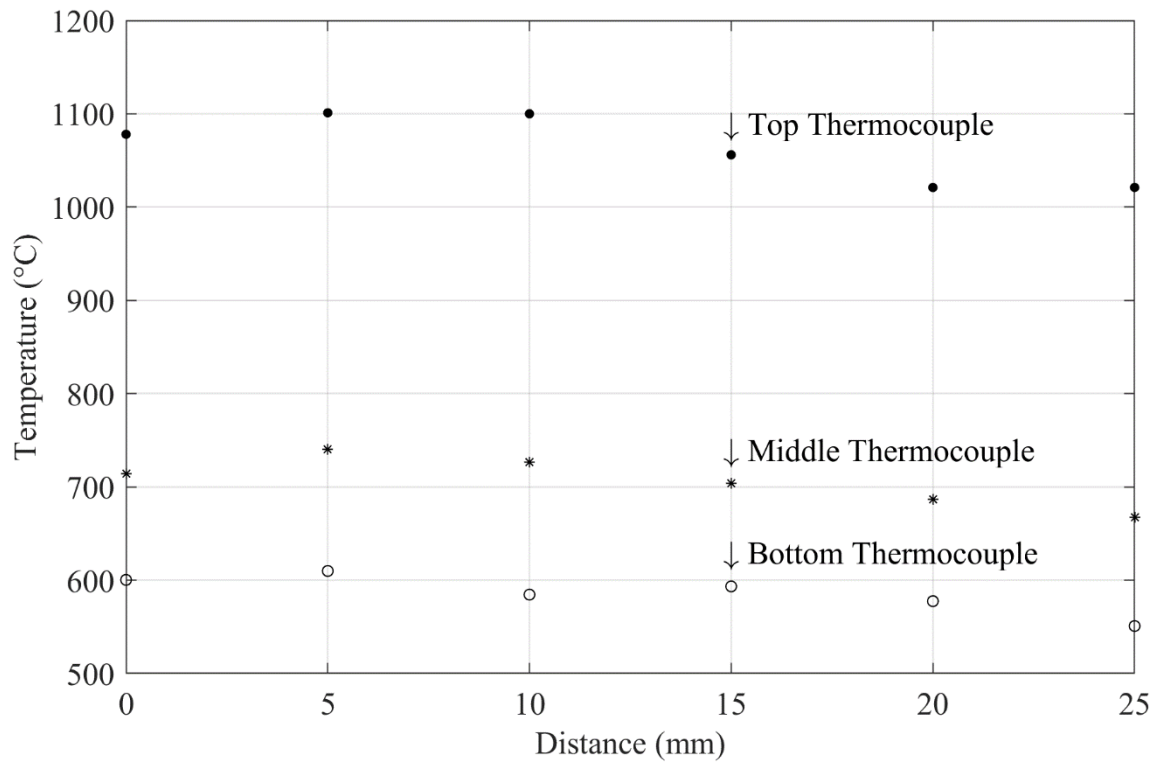
Figure 4.6. Variation of steady state temperature with distance for 60 A current
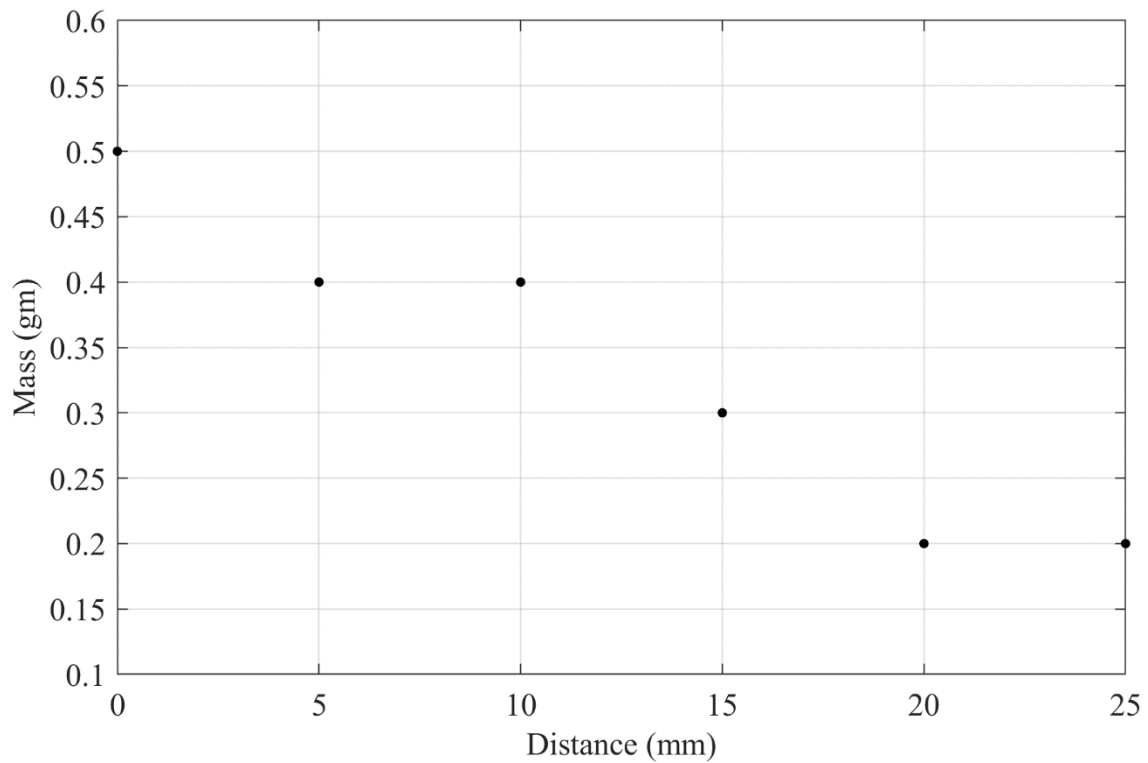
Figure 4.7. Variation of sintered mass with distance for 60 A current

Fig 4.7 shows the increased sintered mass with distance, and Fig 4.8 shows the increasing trend of central thickness for sintered LHS-1. At 0 mm distance, the sintered mass

is 0.5 gm compared to about 2 gm at 50 mm distance for direct sintering. Therefore, it is seen that for the same input current, indirect irradiation leads to less sintered material compared to direct sintering.
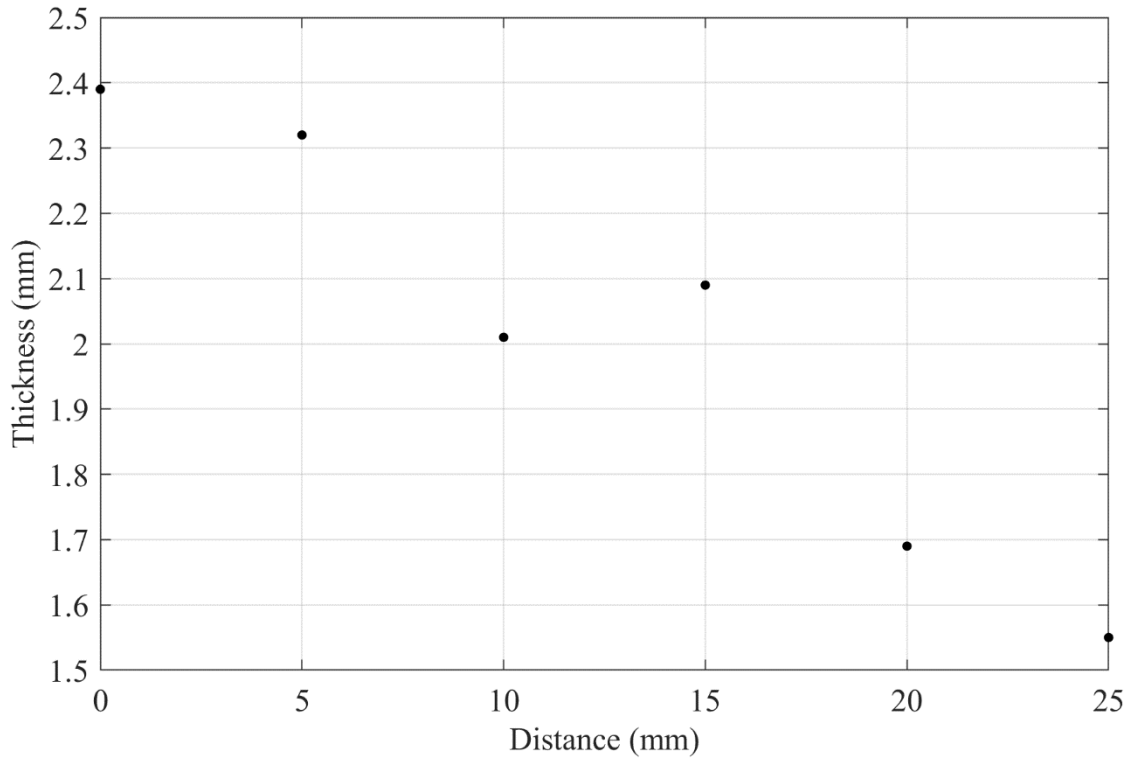
Figure 4.8. Variation of central thickness with distance for 60 A input current

The reason lay behind the use of SiC plates. The irradiation was focused on the top surface of the SiC plate, and the bottom surface of the SiC plate was attached to the top surface of the lunar soil simulant bed. The SiC plate lost heat from the four sides of the plate, which was not in contact with the simulant bed to transfer heat inside the lunar soil simulant bed. Since SiC is a very high heat conductor with high emissivity, the mass of lost heat through radiation is much higher than the mass of lost heat from the top surface of lunar soil simulant at direct sintering. Due to this heat loss, less heat was transferred to sinter the lunar soil simulant. Another reason is that the contact between the bottom surface of SiC and the lunar soil simulant was not perfect, reducing the conduction from the SIC plate to the lunar soil simulant bed. Therefore, the incoming irradiation needed to be increased to obtain a higher amount of sintered material and central thickness. Hence, to sinter more lunar soil simulant

with higher central thickness by increasing the input current from 60 A, two more sets of experiments were conducted with 70 A and 80 A input currents.
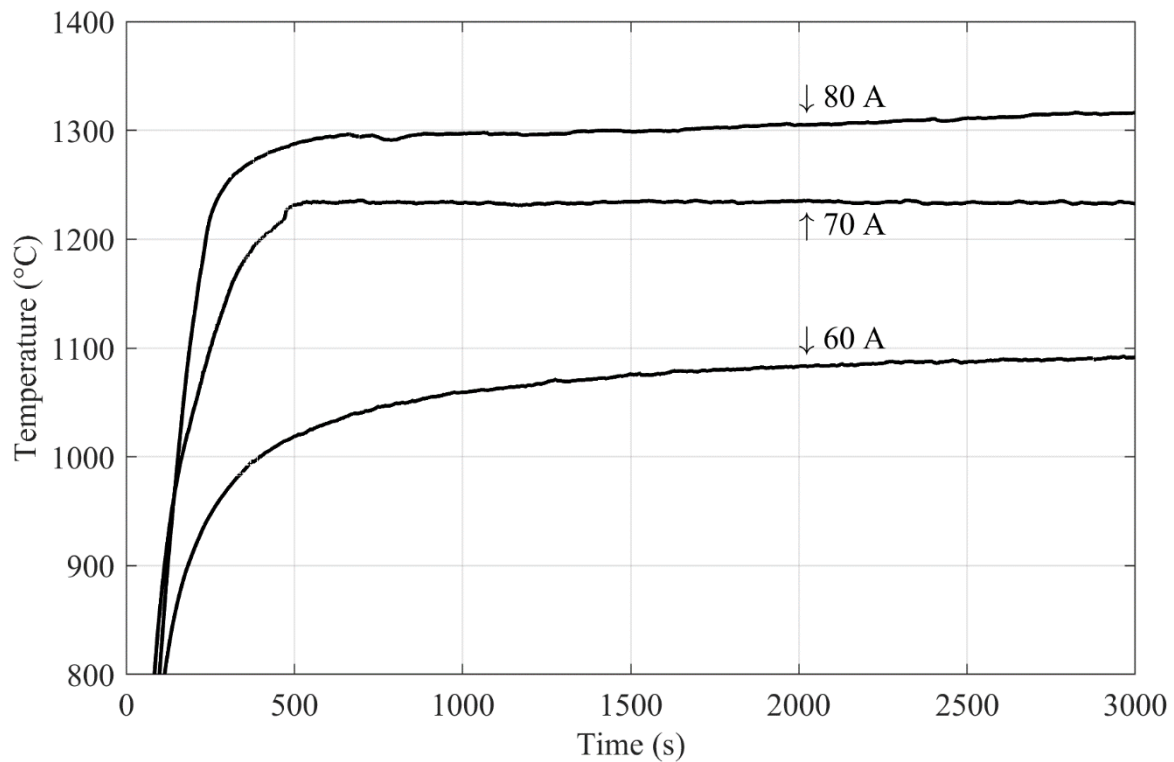
Figure 4.9. Top thermocouple temperature profile at 0 mm distance for different input currents

Figure 4.10. Sintered pieces at 0 mm distance for 80 A, 70 A, and 60 A input currents

Figure 4.9 compares the top thermocouple temperature profile based on radiation level for 0 mm distance from focus for different input currents. With high input current, incoming irradiation increased, causing more temperature raise with time compared to less input current. The higher slope also represents higher heat conduction 2 mm beneath the top surface as well.

At each approach, the steady state is different, which is due to the top thermocouple's specific placement compared to the radiation's central peak. Fig. 4.10 shows the sintered pieces at 0 mm distance for 80 A, 70 A, and 60 A input currents. For all the specific distances and three input currents, the temperature profile is similar to Fig. 4.9, with reduced top thermocouple temperature for increased distances.
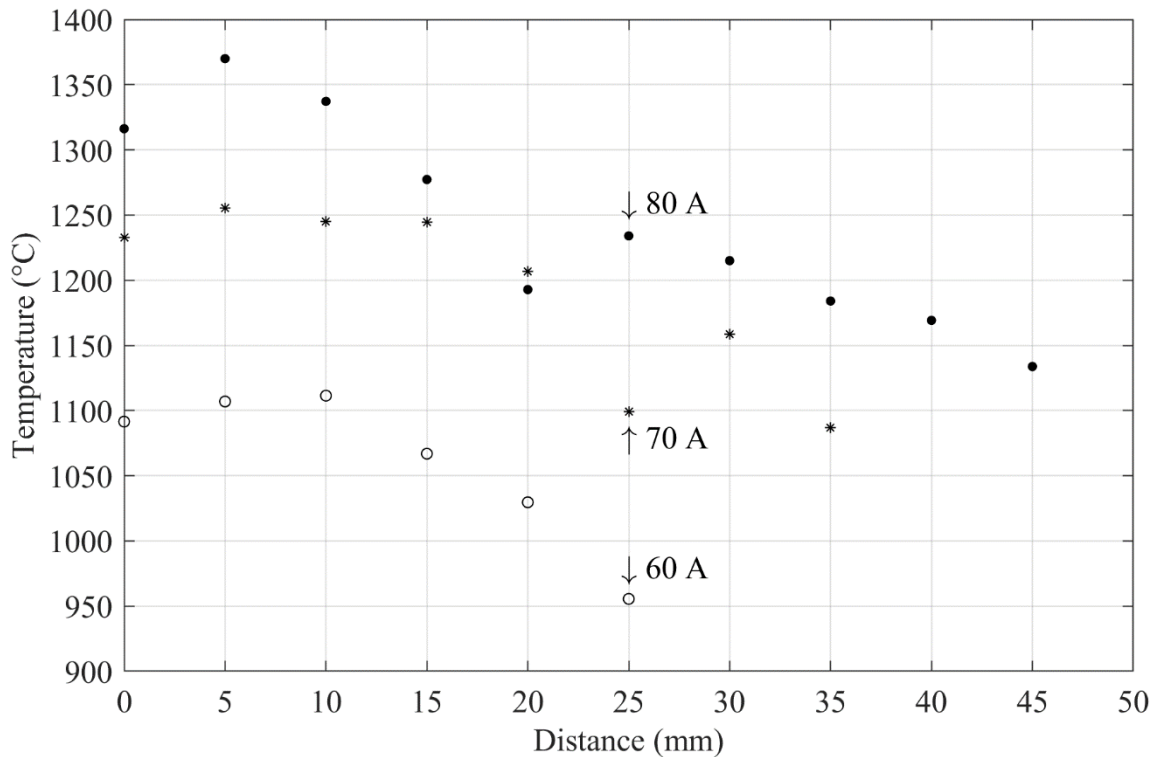
Figure 4.11. Variation of top thermocouple steady state temperatures with distance for varied input currents for indirect sintering

In Fig. 4.11 below, a comparison of top thermocouples and steady-state temperatures with distance from the focal point is demonstrated for different input irradiation with the current. All three trend is similar, increasing with decreased distance. Few irregularities are seen, which caused due to the positioning of the top thermocouple inside the lunar soil simulant bed. Since the process was manual, the top thermocouple tip was not always placed in the same place. If the top thermocouple would have been placed at the same point, the incoming irradiation might hit the top surface at different positions due to the positioning of the crucible. Another reason could be the amount of lunar soil simulant on top of the top thermocouple.

During the filling of the lunar soil simulant bed, the amount of material might vary over the top thermocouple, which could change the conducted heat to represent an inconsistent temperature rise. Higher lamp current corresponds to higher radiative flux, increased temperatures. Temperatures increased with decreasing distance until 10 mm, then thermocouple temperatures dropped. Similar steady-state temperatures were reached for much smaller distances from the focus than in direct sintering experiments. At these positions of 20 mm or less, directly heating the lunar soil simulant would melt it entirely at temperatures over 1500°C in the center. However, the high thermal conductivity of the SiC plate transferred the heat over a wide area of the lunar soil simulant, and the steady state surface temperature at the irradiated surface was significantly decreased for a given heat flux. All samples of sintered and melted soil simulant separated from the SiC plate easily.
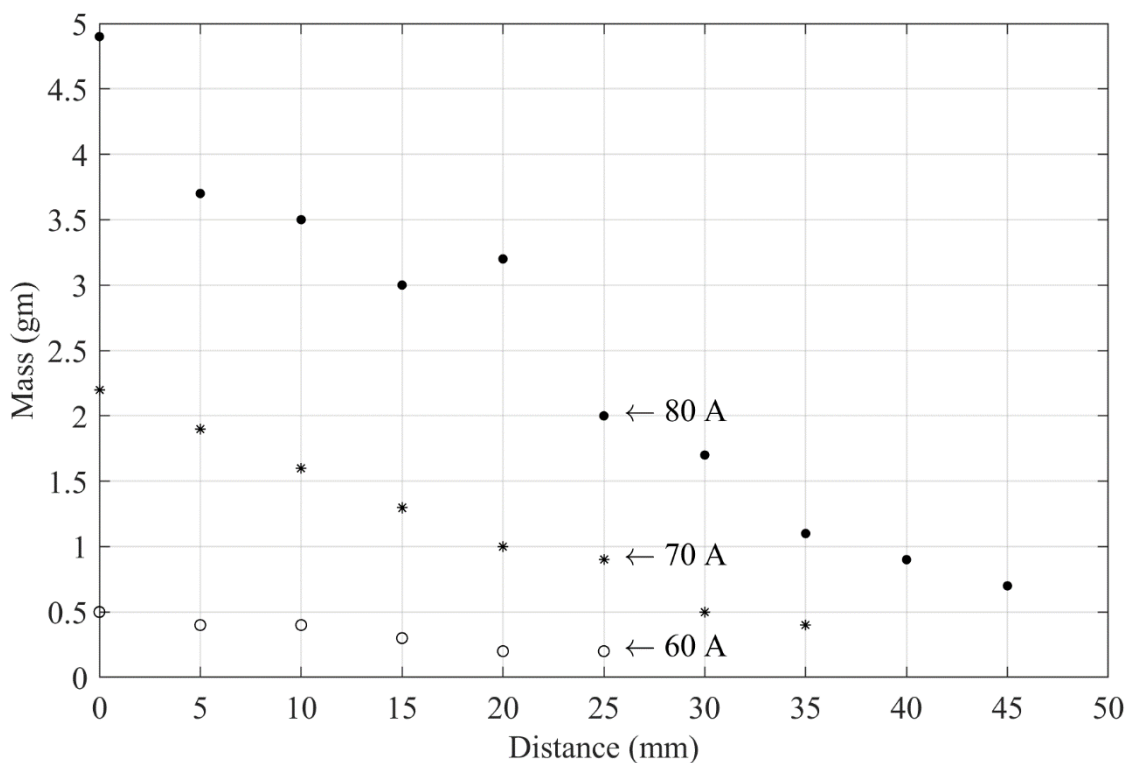
Figure 4.12. Variation of sintered mass with distance for varied input currents for indirect sintering

Fig. 4.12 shows that, with increased thermal radiation at a reduced height, the mass of sintered lunar simulant increased. A similar trend is seen in Fig. 4.13 for the central thickness

of the sintered piece. Central thickness increases with higher thermal radiation for higher input currents. Maximum thickness is about 8 mm, similar to maximum thickness in direct sintering experiments, but nearly 5 gm of material is fully sintered compared to 2 gm for direct sintering.
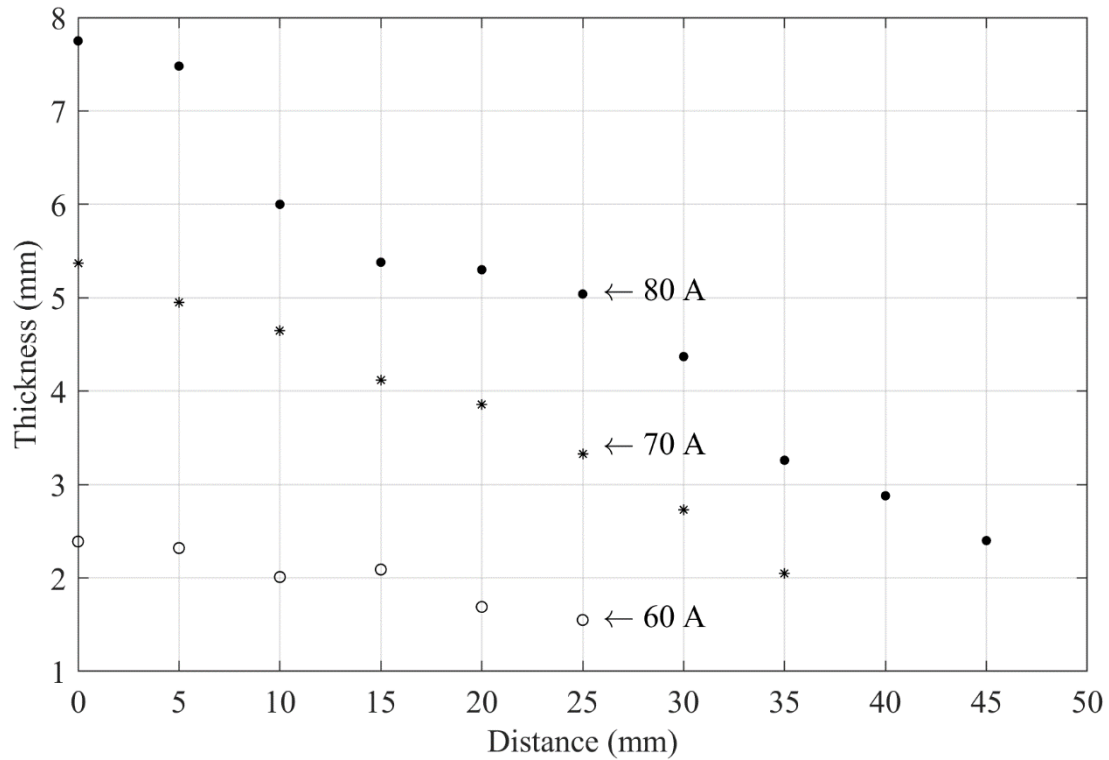
Figure 4.13. Variation of central thickness with distance for varied input currents during indirect sintering

The indirectly heated sample displays a much smaller area of melted material for these two samples. As a disadvantage, a steady state was reached in indirect heating at approximately 20:09 minutes compared to 3:19 minutes in direct heating for comparable cases of 60 A and 50 mm height. Indirect sintering may be a valuable tool to sinter lunar soil simulant more uniformly if using concentrated solar radiation highly focused to a point. However, it holds the downside of longer processing times.

For repeatability, three identical experiments were performed at 0 mm height with 80 A input current; for three individual experiments, the maximum sintered mass was 4.8 gm with a central thickness of 7.23 mm, whereas the minimum was 3.9 gm with a central thickness of

7.11 mm. For this configuration, the maximum variation is 18.75% for the sintered mass and 1.66% for the central thickness. Similar variations were found for the other configurations.

4.3. Indirect Sintering Special Case Analysis

A high heat flux with high input current in the simulator leads to faster heating but melts the simulant. It may be advantageous to vary the solar input to rapidly heat lunar soil simulant with high flux, then reduce the flux when the soil simulant approaches sintering temperature to avoid melting. To apply this approach, indirect sintering cases were analyzed.

From Fig. 4.12 and 4.13, it is visible that for 0 mm distance and 80 A current, 4.9 gm of simulant was sintered with a central thickness of 7.25 mm, but the lunar soil simulant top surface melts. For 70 A current, the steady state sintering temperature is 1232°C, and 2.2 gm of simulant was sintered with a central thickness of 5.37 mm without melting the top surface. Therefore, the lunar soil simulant initially would be heated with 80 A input current, and then the input current would be reduced to 70 A as the simulant would approache the sintering temperature.

For 70 A current steady state temperature 1232°C achieved after 8 minutes. With 80 A current the same temperature can be achieved faster and then reducing the input current to 70 A would keep the temperature constant. For 0 mm distance, to do this experimentally, several attempts were taken to see how to reach steady state temperature faster and maintain the temperature there. The experiments were done with the initial mirror setup and with no flux measurements from the thermal imager.

Trial 1: The experiment started with 80 A current input. Since steady state for 70 A comes after 8 minutes, the input current was reduced instantly to 70 A after 4 minutes. In this case, the temperature risen much higher than 1232°C in the first 4 minutes, and after lowering the input current, a rapid temperature fall was noticed in Fig. 4.14. After a particular time, the

top thermocouple temperature went to steady-state, and after 50 minutes, 2 gm of lunar soil simulant was sintered.

Trial 2: The experiment started with 80 A current input. When the temperature reached 1232°C after 3 minutes, the input current was reduced to 70 A. In this case, for 70 A input current, the temperature fallen and took longer to reach steady state temperature, as seen in Fig. 4.14, and after 50 minutes, 2 gm of lunar brick was sintered.

Trial 3: At first, the experiment was started with 80 A current input. When the temperature was at the steady state temperature of 70 A current, the input current was reduced to 70 A gradually. The current reduction started after 3 minutes when the temperature of the top thermocouple reached 1232°C and continued up to 10 minutes to keep the temperature steady until the system went to steady state temperature for 70 A current. In this case, 2.1 gm of LHS-1 lunar soil simulant was sintered.
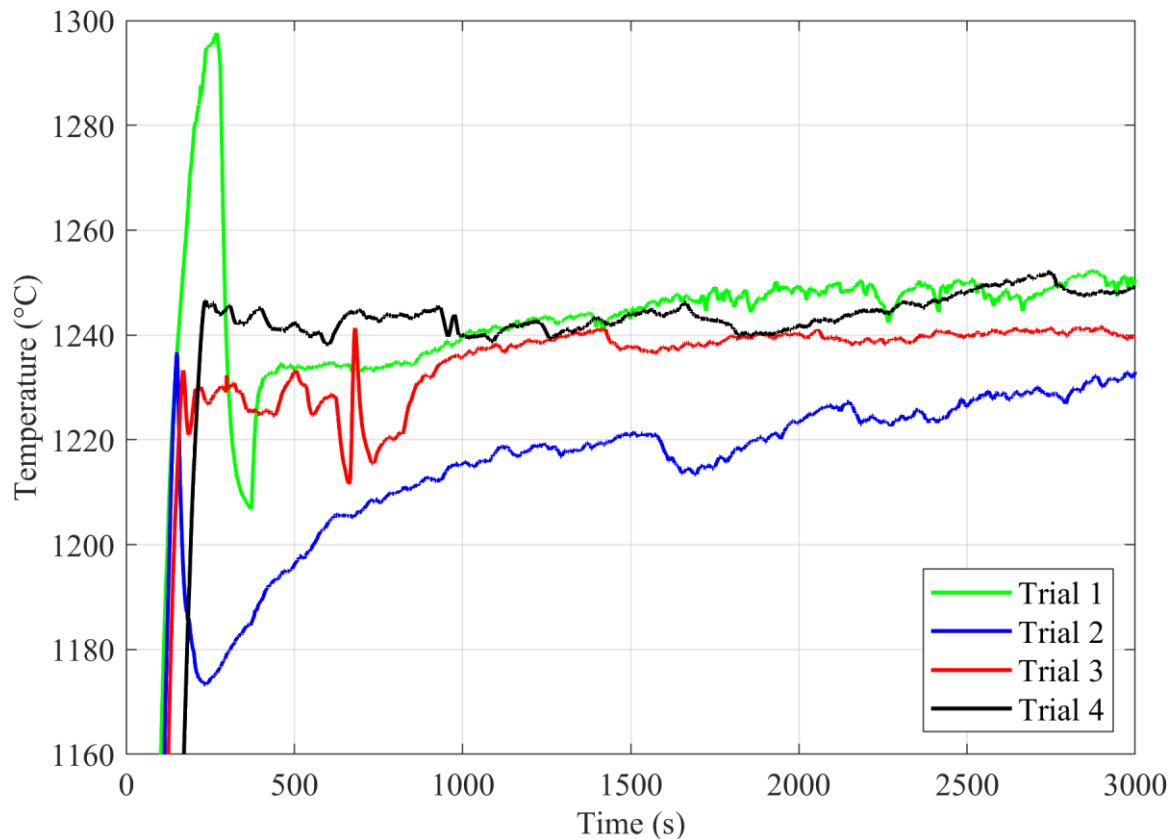
Figure 4.14. Variation of Top thermocouple temperature for 0 mm distance with varying current input (80 A to 70 A)

Trial 4: At trial 3 some irregularity was seen in the first 10 minutes due to an uneven gradual decrease of input current. Another more controlled attempt was taken to reduce the noise, which holding the temperature at 1232°C from 3 minutes to 8.5 minutes. The experiment was stopped after 50 minutes, maintaining the steady state temperature. The top thermocouple temperature remained steady from the beginning without any further fluctuation. In this case, 2.2 gm of LHS-1 lunar soil simulant was sintered. The comparison of the top thermocouple temperature in Fig. 4.14 gives a fine visualization of the temperature profile during the trials along with the constant 70 A and 80 A input current experiments. In all cases, the final sintered mass is similar.
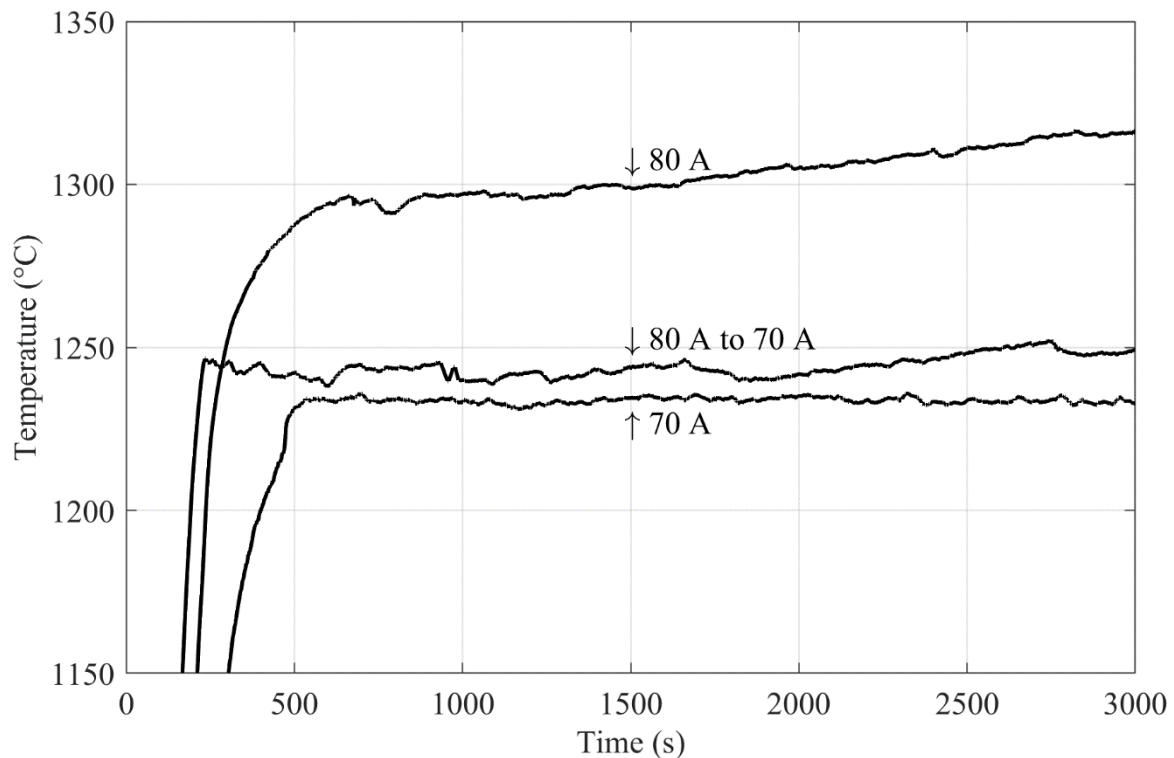
Figure 4.15. Variation of top thermocouple temperature for varied input currents at 0 mm distance from the focal point during indirect sintering

Fig. 4.15 shows that, temperature profile for 80 A to 70 A reaching a temperature of 1240°C in approximately half the time as a constant current of 70 A would take. Fig. 4.16 shows three cut and sanded sintered lunar bricks from the experiment set described.
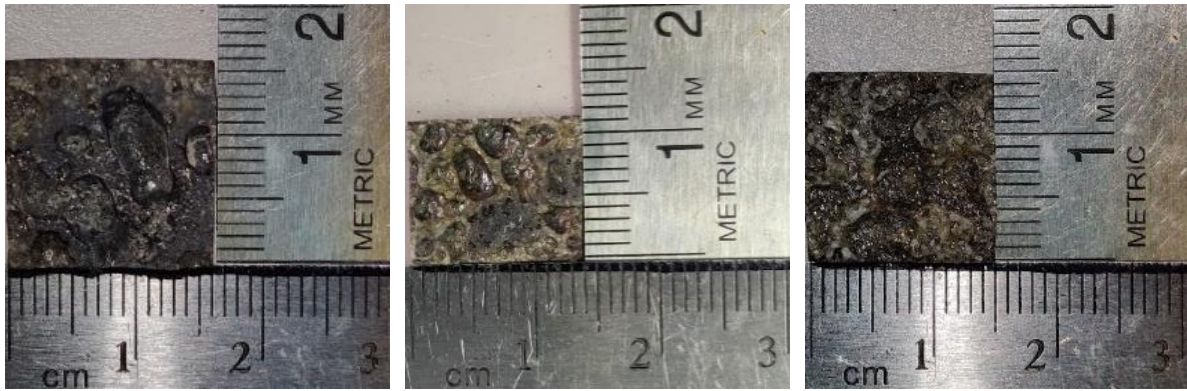
<div style="text-align:center">(A)   (B)   (C)</div>

Figure 4.16. Indirectly sintered pieces for different input currents at 0 mm distance from focus for (A) 80 A (B) 70 A and (C) 80 A to 70 A

With the thermal imager, SiC plate, and new mirror, another set of experiments were conducted by measuring heat flux for three different input currents. Fig. 4.17 shows the indirect experiment in the thermal imager window. In this experiment, three flux configurations were chosen. The input current was converted to incoming heat flux, and the flux was varied by varying the input current.
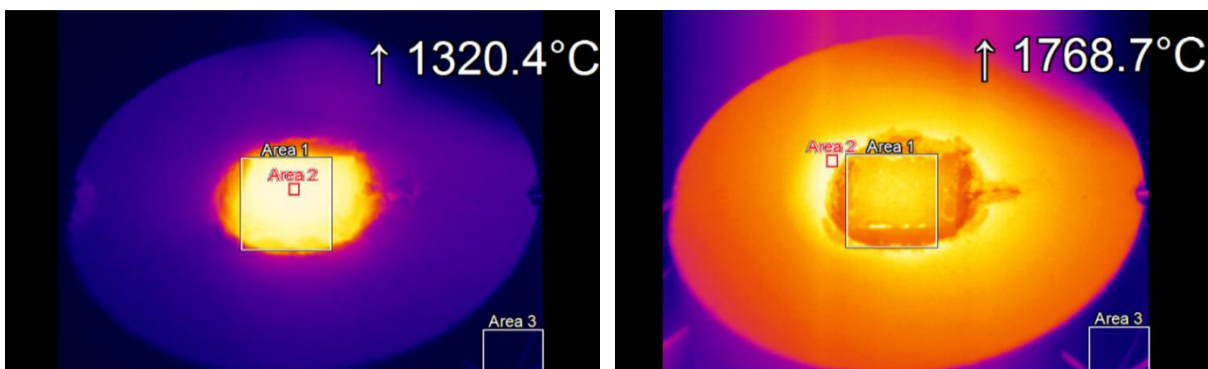
Figure 4.17. Indirect experiment with thermal imager

After experimenting with the new setup, at the focal point of incoming irradiation, with 80 A current input, the flux was measured as 276.37 kW/m^2. The system's steady state was reached after around 30 minutes at about 1180°C top thermocouple temperature. The average sintered mass found in six individual trials was 2.4 gm, with an average central thickness of 4.86 mm. With 90 A current, the flux was measured at 281.71 kW/m^2. Steady state was reached

after around 10 minutes at about 1290°C. After about 4 minutes, the temperature became 1180°C, the steady state temperature for 276.37 kW/m^2 heat flux. For 100 A input current, the flux was 304.92 kW/m^2. and the steady state came after around 27 minutes at about 1360°C. At around 2 minutes, the temperature became 1180°C, the steady-state temperature for 276.37 kW/m^2 heat flux; at around 3 minutes, the temperature became 1290°C, the steady state temperature for 281.71 kW/m^2 heat flux.
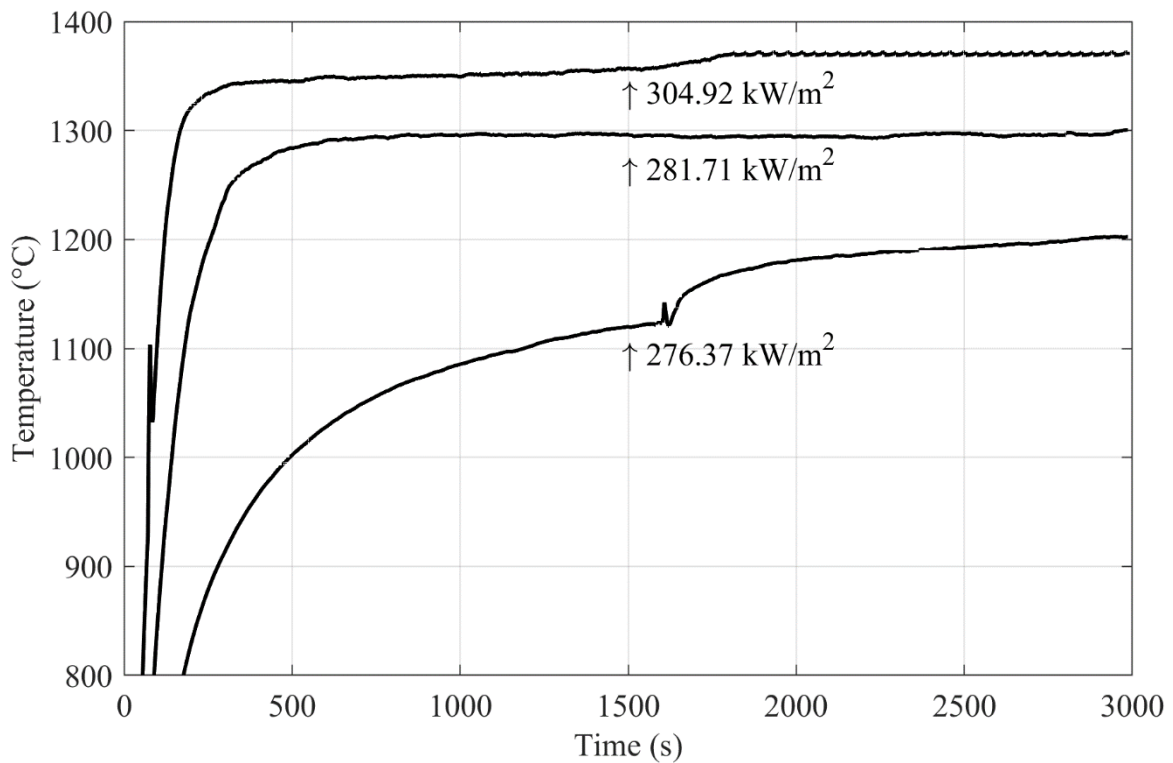
Figure 4.18. Top thermocouple's temperature profile at different heat flux

| (A) 276 kW/m^2 | (B) 281.71 kW/m^2 | (B) 304.92 kW/m^2 |

Figure 4.19. Top surface of sintered lunar bricks for different heat flux
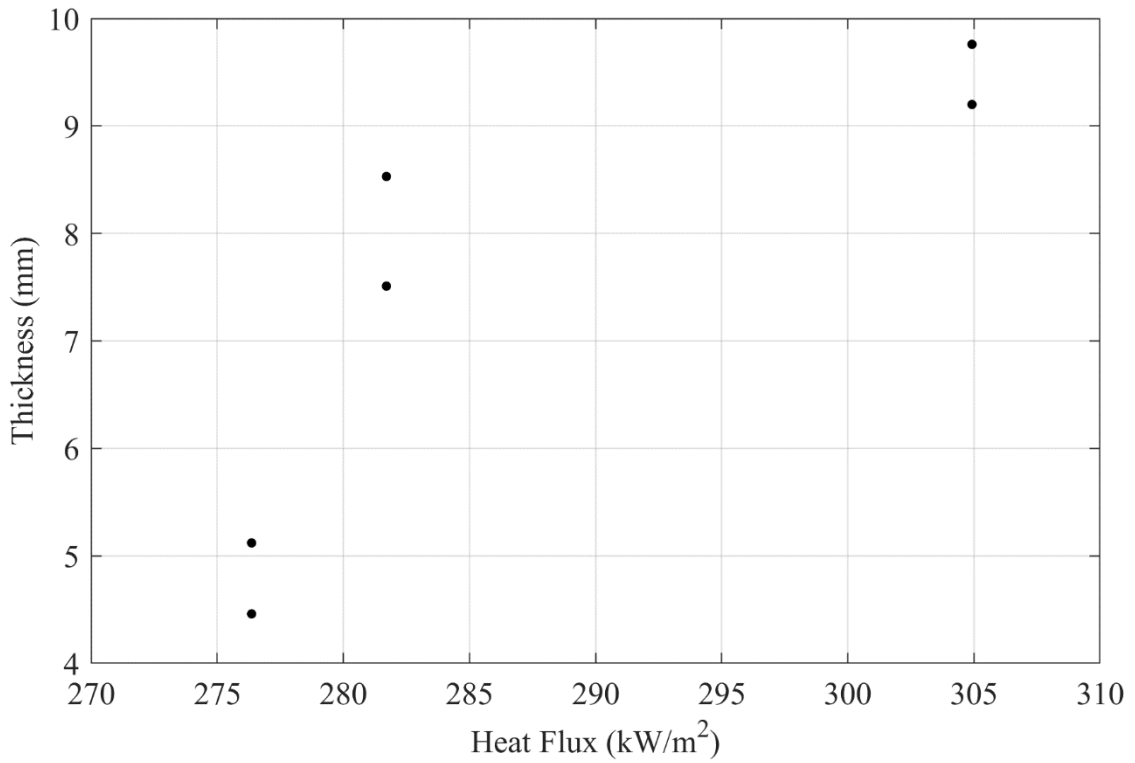
Figure 4.20. Central thickness of indirectly sintered LHS-1 with varying flux
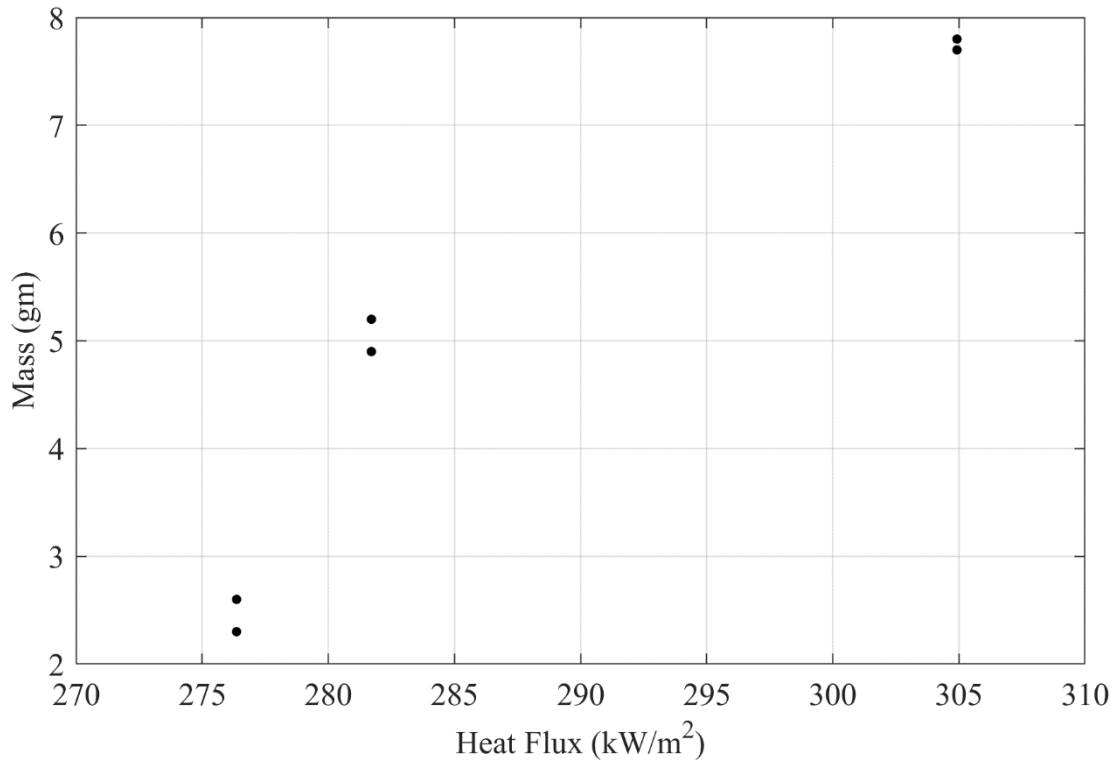
Figure 4.21. Sintered mass of indirectly sintered LHS-1 with varying flux

Fig. 4.18 represents the temperature profile with three different fluxes. Fig. 4.19 shows

the sintered material's top surface with these specific heat fluxes.

Fig. 4.20 and Fig. 4.21 consecutively represent the central thickness and sintered mass with heat flux. Two data points are plotted from several experiments showing the range of the thickness and mass. From both the trends, it is visible that the slope of central thickness and sintered mass decrease with the increase of heat flux.

From Fig. 4.19, it is seen that for 281.71 kW/m^2 and 304.92 kW/m^2 heat flux the top surface was melted. To obtain sintered material without melting, the steady state temperature of 276 kW/m^2 heat flux can be reached faster with 281.71 kW/m^2 or 304.92 kW/m^2 heat flux and by reducing input current to reduce the heat flux, as explained before. Fig. 4.22 shows the top surface of the sintered lunar bricks from these special experiments where reduced melting is noticeable on the top surface. In contrast, it took less time to reach the sintering temperature.

| (A) | (B) | (C) |
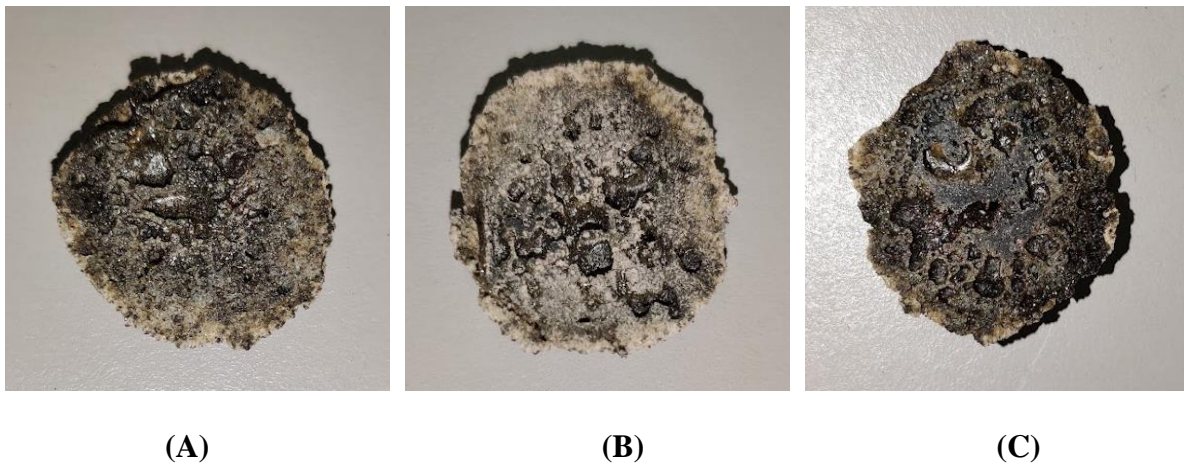
Figure 4.22. Top surface of sintered lunar bricks with (A) 276 kW/m^2, (B) 281.71 kW/m^2 to 276 kW/m^2, and (C) 304.92 kW/m^2 to 276 kW/m^2

Specimens resulting from experiments are irregular, roughly hemispherical, and granular. Reliable strength testing of such samples necessitates post-processing to ensure regular shape and flat surfaces. A diamond-coated ceramic saw was used to shape the specimens, and sheets of various grit sandpaper were used gradually to smooth the surfaces by hand. Digital calipers were used to ensure uniformity and measure face area for compressive strength calculations. The post-processed samples were then tested using an MTS vertical load frame to determine maximum compressive strength. Each specimen was compressed at 1 mm

per minute until fracture using an MTS 50 kN load cell. Force (N) and deflection (mm) data were gathered for each sample. Maximum compressive strength was calculated using the maximum endured force before fracture and sample dimensions. Table 4.4 presents the average sintered mass, central thickness, and strength of the sintered pieces with different fluxes described above.

Table 4.3. Experimental results of indirect sintering special cases

Current (A)	Flux (kW/m^2)	Avg. Sintered Mass (gm)	Avg. Central Thickness (mm)	Avg. Strength (MPa)
80	276.37	2.4	4.864	24.273
90	281.71	5.05	8.02	30.237
90-80	281.71 - 276.37	2.5	4.875	34.276
100	304.92	7.75	9.48	22.914
100-80	304.92 - 276.37	2.2	4.545	21.489

Table 4.3 shows that the special experiments go to sintering temperature faster, but a similar result is achieved for central thickness and sintered mass. Finally, the compressive strength was calculated for several samples. At 276.36 kW/m^2, strength varied from 18 to 68 MPa, and similar variation was found for six sets of experiments. With this behavior in strength data, no conclusion was achieved.

CHAPTER 5

THERMODYNAMIC ANALYSIS

Both the construction material and oxygen can be extracted from the same lunar soil simultaneously from a single process which will be economical [18]. Since both the sintered lunar brick and water can be produced from the same process, a developed reactor is required to sinter lunar soil for making construction material and extract water for oxygen production. The water will be removed and transported for electrolysis to obtain oxygen simultaneously. During the whole sintering and oxygen extraction process the input and output energy of the system can be found out through a thermal analysis [73]. For the calculation a thermal energy balance system needs to be developed for the sintering furnace and water extraction module by considering all the input and output energies of the lunar soil reduction system.

5.1. Oxygen Production

Oxygen can be extracted from lunar soil through various kinds of processes. Most approached techniques are based on chemical reduction, acid treatment, electrolysis, pyrolysis, etc. Some methods to be mentioned are- reduction with hydrogen, reduction with methane, sulphuric acid reduction, electrolysis of molten lunar soil simulant, electrolysis of solid lunar soil simulant, electrolysis of water, and vapor phase pyrolysis [18].

The most straightforward and efficient process is the reduction of oxides using hydrogen gas. It is a two-step process where the ilmenite in the lunar soil simulant is reduced by hydrogen and forms water. The water is electrolyzed to obtain oxygen and hydrogen. Hydrogen can be re-used in the reaction cycle, showing a high conversion efficiency [16]. But to release oxygen from the ilmenite, through ilmenite reduction by hydrogen, it requires a very high temperature like 800-1000°C [14], [17]. The reactions associated are:

$$FeTiO_3 + H_2 + heat \rightarrow Fe + TiO_2 + H_2O$$

$$H_2O + el. \rightarrow H_2 + 0.5\ O_2$$
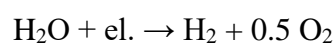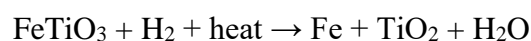
Here the efficiency of the process depends on the ilmenite content supplied. So, this process is only suitable where there is enough ilmenite present. Also, the presence of sulfide can create a problem as it can form toxic hydrogen sulfide during the reaction so the lunar soil simulant may need some purification before the hydrogen reduction processes [18].

The hydrogen reduction process requires more than a hydrogen reduction reactor to support the smooth operation cycle. A general design for extracting oxygen through hydrogen reduction may contain the following processes shown in Fig. 5.1.
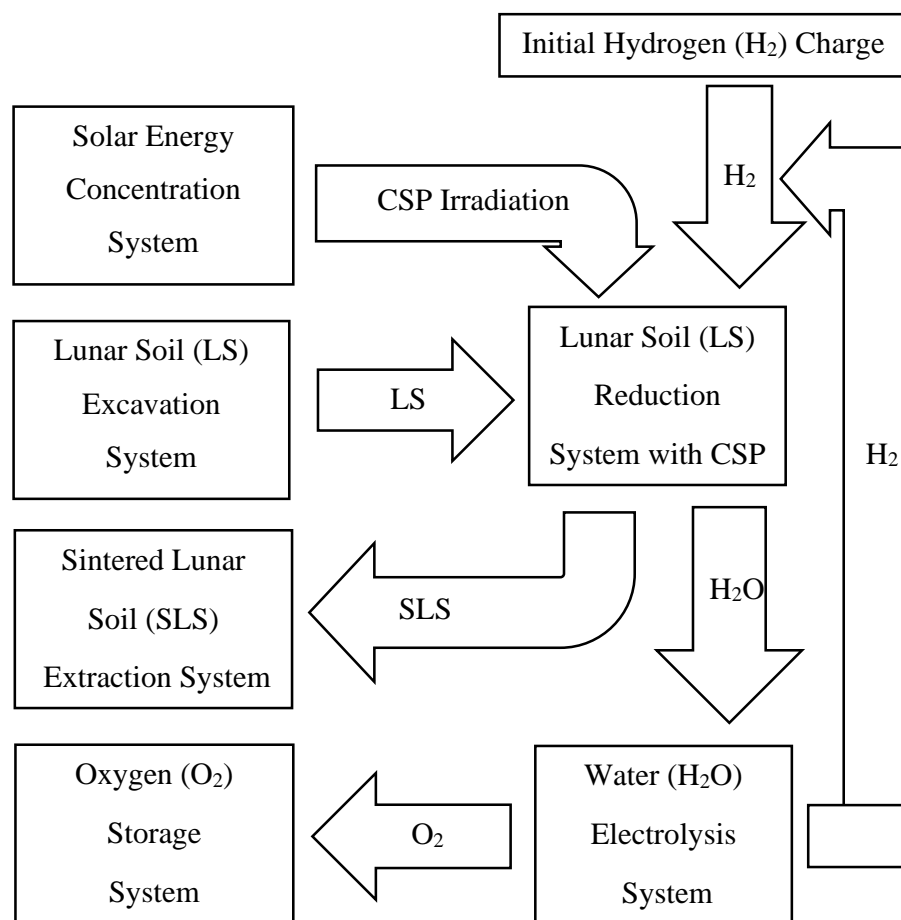
Figure 5.1. Oxygen production from lunar soil reduction system [17]

For simultaneous operation, a sealed furnace must be developed and operate at very high pressure and temperature. The chamber will be filled with hydrogen for hydrogen reduction of lunar soil simulant. A glass-sealed opening would allow concentrated sunlight to enter for the sintering operation. A feeder would supply the loose lunar soil. To trap the bi-

product gases with water vapor, an opening is required, and a mechanized mechanism is necessary to take out the sintered lunar brick. The first step is to supply enough hydrogen to prepare the environment for hydrogen reduction. Then lunar soil needs to be collected and transferred into the furnace through the feeder. After that, concentrated sunlight needs to direct inside the furnace and focused on top of the lunar soil to sinter the soil in a hydrogen atmosphere at the sintering temperature. The metallic oxides will break during the sintering process to release oxygen and other gases. Oxygen reacts with hydrogen to form water vapor at very high sintering temperatures. This water vapor is then will be removed from the furnace and transported to the electrolysis chamber to extract oxygen. The hydrogen produced during electrolysis needs to be directed to the system again to maintain the required hydrogen quantity for hydrogen reduction.

Table 5.2 shows the enthalpy of the reactants and products of the ilmenite reaction. From the ilmenite reduction reaction, energy requirement can be calculated with the help of the enthalpy of the reactants and products. The required energy found for ilmenite reduction is 374.1 kJ/mol.

Table 5.2. Enthalpy of the reactants and products of ilmenite reduction

Molecule	Enthalpy (kJ/mol)
$FeTiO_3$	-1153.9 [67]
H_2	0
Fe	0
TiO_2	-542.66 [68]
H_2O	-237.14 [69]

For JSC-1A, at 1273 K (1000 °C), about 0.68 gm water was obtained from 40 gm of lunar soil simulant, which equals 1.8 wt% of water. The system pressure does not significantly affect water production, especially under 1300°C [70]. Below 1527°C, the production of water has approximately a linear relation with temperature. However, water production rapidly increases with temperatures rising above 1527°C [70]. Based on this assumption, for 1 kg of lunar soil simulant, all the calculations are conducted in this chapter to plot the results.
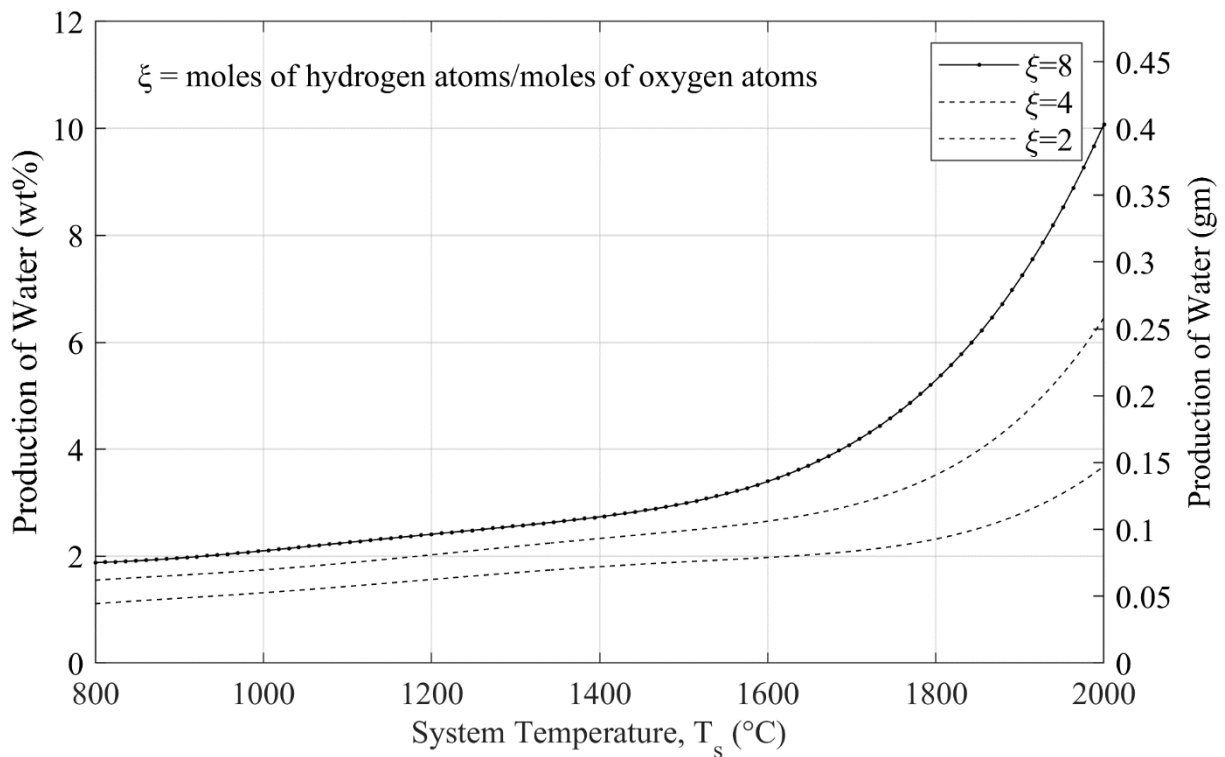
Figure 5.2. Production of water in wt%, and in gm for 1 kg LHS-1 with system temperature [70]

Fig. 5.2 presents cumulative water production with temperature from ilmenite with varied ξ where ξ = moles of hydrogen atoms/moles of oxygen atoms. Equations of water production with temperature are produced from Fig. 5.1, and through the MATLAB program, for any temperature, the mass of water produced can be found.
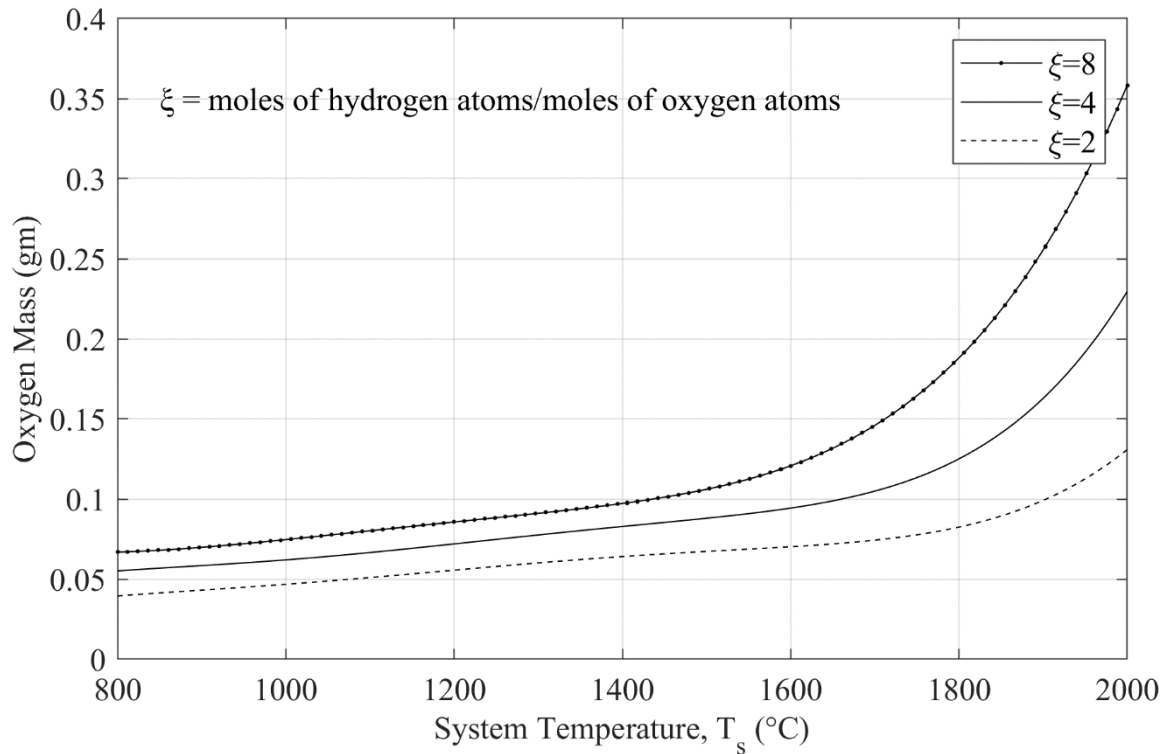
Figure 5.3. Production of oxygen with system temperature for 1 kg of LHS -1

During the sintering process, oxygen production depends on the production of water, where oxygen production is proportional to the increase in temperature [70]. Fig. 5.3 shows the mass of oxygen produced with temperature from 1 kg of LHS-1 lunar soil simulant if all of it is sintered.

Yoshida et al. shows cumulative water production from 40 gm ilmenite [71], taking ξ = 4. They got water production graph for 900°C, 950°C, 1000°C and 1050°C. For ξ = 4, from the MATLAB program, water production can be calculated for higher temperatures up to 2000°C. After calculating the water produced at any temperature, a similar water production profile with time was found and plotted in Fig. 5.4. For each graph, an equation is achieved, which helped to develop another MATLAB program to find the wt% of water produced at any time for any temperature. It can be noticed from the plot that after around 10 minutes, the production of water reduces for all the temperature plotted. As expected, with the MATLAB program, it is verified that the production rate starts decreasing after a particular time and goes to zero.
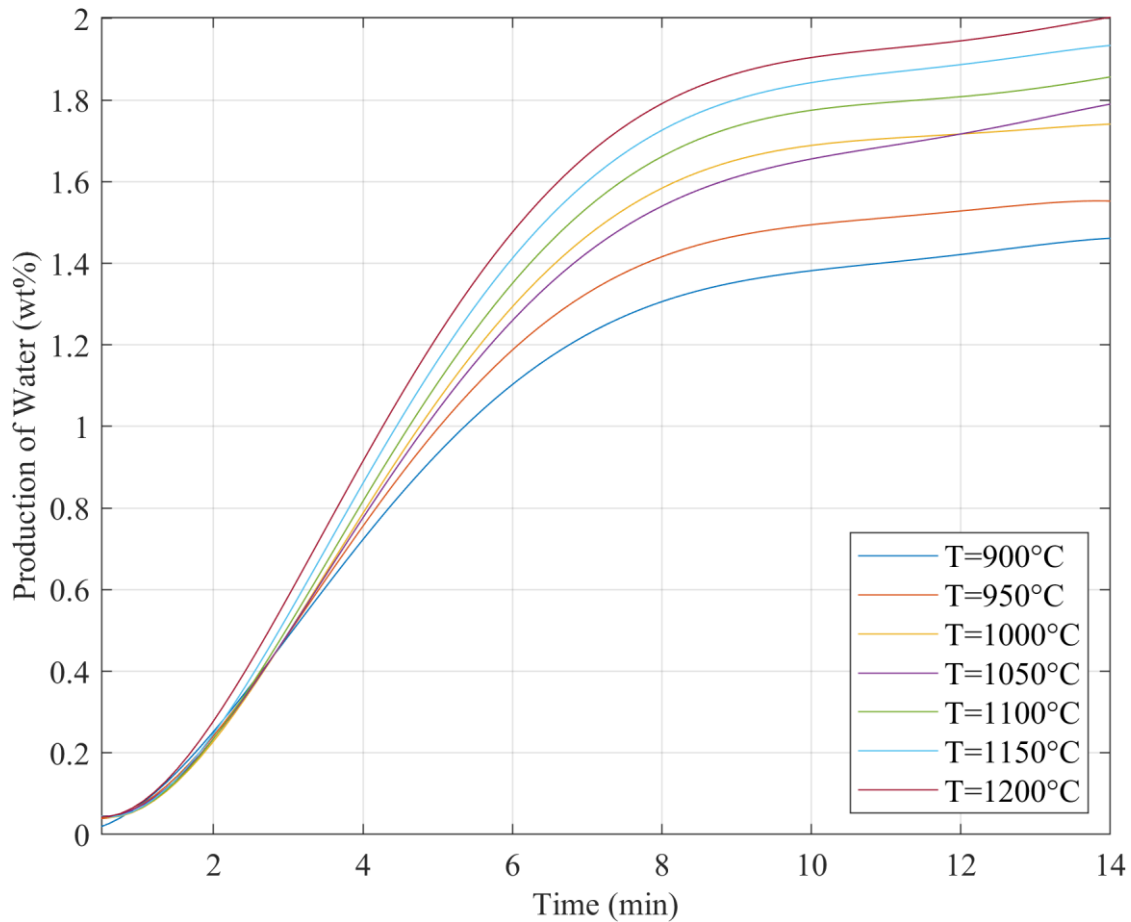
Figure 5.4. Production of water with time at different temperatures when ξ = 4 [71]

5.2. Energy Balance

The energy of input and output can be found out through thermal analysis [72]. In terms of thermodynamics, the energy requirement depends on different particle types and machinery-specific influencing factors [73].

Since concentrated solar power is used as the source of heating, with respect to that, a thermal energy balance system can be developed for the sintering furnace by considering all the input and output energies as shown in Fig. 5.5. Energy enters the system through concentrated solar power, Q_{solar} which is absorbed by the system to sinter the material and to drive the ilmenite reduction reaction. Hydrogen gas is supplied to the system to create a hydrogen atmosphere. Inside the system, the lunar soil simulant goes through an endothermic reaction in the presence of a hydrogen environment to be sintered at the sintering temperature

and radiate the excess energy as Q_{rerad} to the environment through the aperture. All other boundary surfaces lose some heat through a conduction and radiation network. Through the sintering process, water will be produced, extracted, and forwarded to the electrolysis chamber. Excess hydrogen will come out during the extraction of vaporized H_2O. At the electrolysis chamber, electrolysis will occur to produce oxygen, and retrieved hydrogen gas will be sent to the system again.
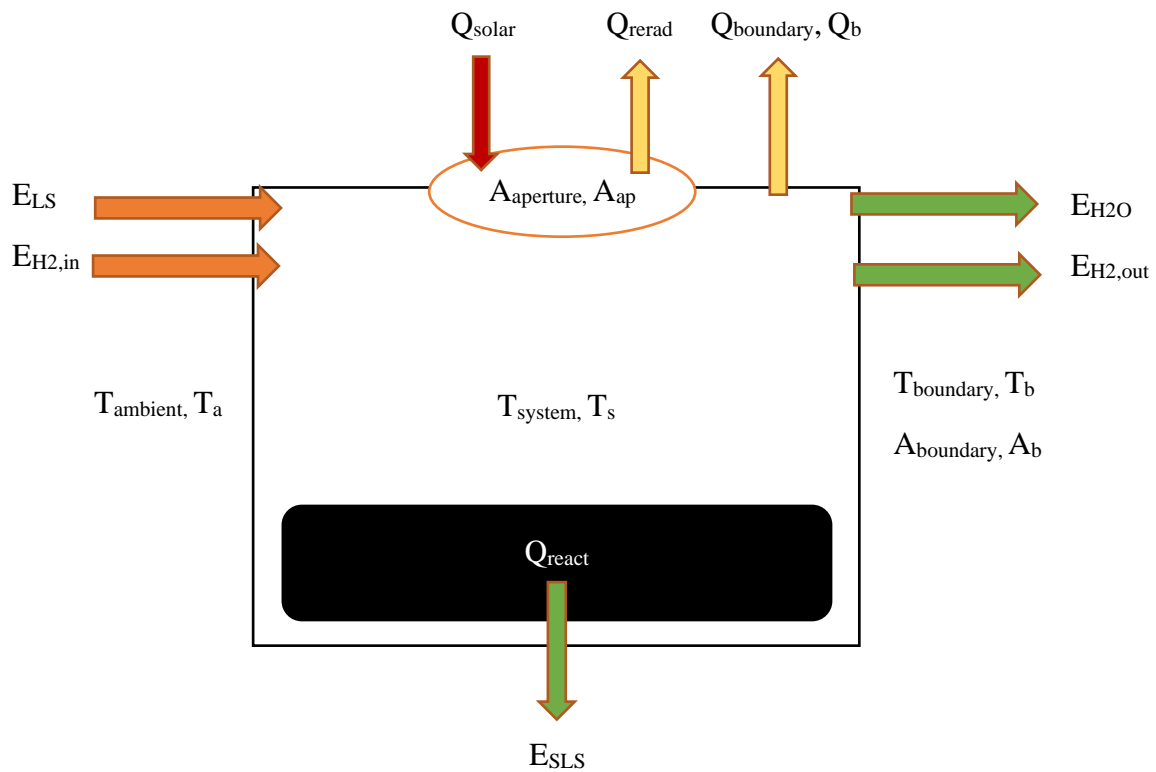
Figure 5.5. Energy input and output in the furnace

Therefore, considering all the energy entering and escaping the system, as shown in Fig. 5.5, the energy balance can be written as-

$$E_{solar} + E_{LS} + E_{H_2,in} + E_{react} = E_{rerad} + E_b + E_{H_2O} + E_{H_2,out} + E_{SLS}$$
$$\dots\dots\dots\dots\dots\dots\dots\dots\dots\dots\dots \text{(5.1)}$$

Assuming 1 kg of lunar soil simulant, the energy balance is conducted. From the experiment, it is found that the maximum achievable sintered thickness without a molten pool is 8 mm. For 1 kg of lunar soil simulant, with 8 mm thickness, the length of the uncompressed square lunar soil simulant bed is 310 mm, and the area of the top surface of the bed is 0.1 m^2.

Assuming the length of one side of the square furnace is 320 mm, and the height is 80 mm, with the irradiation angle of 45° and aperture area of 0.005 m², the inside area of the system becomes 0.3 m².

For the designed furnace, the total solar energy can be calculated from the solar flux constant on the lunar surface, I, which is 1360 W/m² [74], concentration ratio, C, area of the aperture, A_{ap}, and the time duration Δt.

$$E_{solar} = \Delta t \times Q_{solar} = \Delta t \times I \times C \times A_{ap}$$
....(5.2)

With some energy, E_{LS} will enter with the lunar soil simulant. The energy entering the system with the lunar soil simulant can be calculated with the specific heat of the lunar soil simulant and temperature rise. Since at the inlet, no temperature gain, ΔT occurs for lunar soil simulant, therefore, no energy enters the system with the lunar soil simulant.

$$E_{LS} = M \times C_p \times \Delta T = 0$$
.... (5.3)

The energy entering the system with hydrogen can be calculated by multiplying the moles of hydrogen with the specific enthalpy of hydrogen, $\bar{h}_{H2}$ at Ambient Temperature, T_a.

$$E_{H_2,in} = n_{H_2,in} \times \bar{h}_{H_2}(T_a)$$
.... (5.4)

The system will gain some energy from the ilmenite reduction reaction. With temperatures rising, more ilmenites react with hydrogen, and the endothermic reaction stores energy in the system. The reaction energy can be achieved by multiplying the reaction enthalpy with the number of moles reacted at that temperature. Fig. 5.6 shows the reaction energy at different system temperatures for 1 kg of lunar soil simulant.

$$E_{react} = n_{IL} \times \bar{h}_{react}(T_s)$$
.... (5.5)
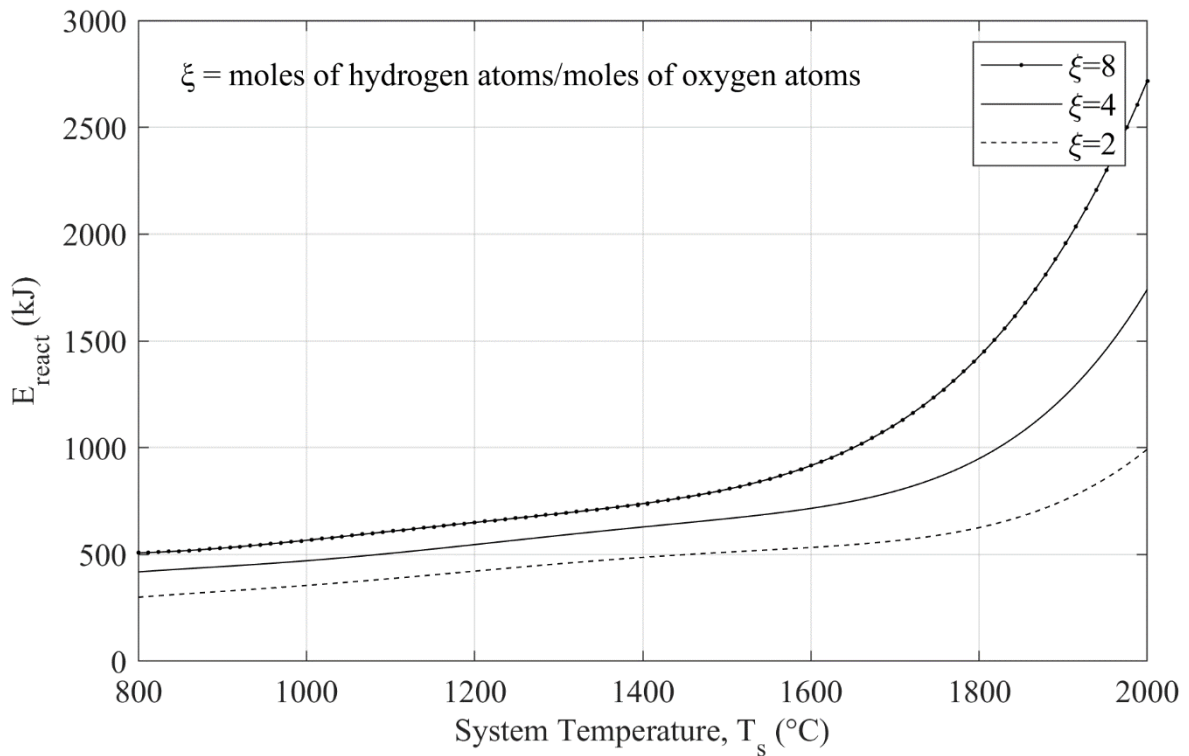
Figure 5.6. Reaction energy at different system temperatures

The system will lose energy by radiation through the aperture window. The re-radiation heat loss can be calculated by Stepfan-Boltzmann law, with emissivity coefficients, ε, Stefan–Boltzmann constant, σ, and difference of fourth power of the temperatures. Since the whole system is in constant temperature, T_s, considering it as a blackbody with $\varepsilon = 1$, radiation heat loss will be:

$$E_{rerad} = \Delta t \times Q_{rerad} = \Delta t \times \sigma \times A_{ap} \times (T_s^4 - T_a^4)$$

.... (5.6)

There will be another heat loss through the boundary wall. The heat will be conducted through the insulation and then radiated from the boundary wall. This can be shown as a resistant network as in Fig. 5.7. Since the lunar surface does not have any air, no convection heat loss will occur from the surface wall.
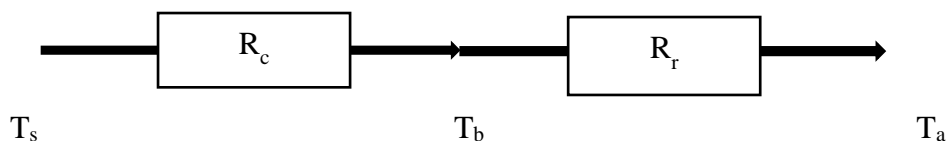
Figure 5.7. Resistance network for heat loss through boundary wall

Here resistance R_c will be present for conduction heat transfer between system temperature, T_s, and system boundary wall temperature, T_b. If the thickness of the boundary insulator is X, thermal conductivity of the insulating material is K, and system surface area is A_s, then conduction heat transfer will occur from T_s to boundary temperature T_b as:

$$Q_c = \frac{K \times A_s \times \Delta T}{X}$$

$$= \frac{\Delta T}{\frac{X}{K \times A_b}}$$

$$= \frac{T_s - T_b}{R_c}$$

Therefore,

$$R_c = \frac{X}{K \times A_b}$$

………………………………. (5.7)

Radiation heat loss will occur from boundary surface to the outside environment. If boundary surface area is A_b and emissivity of the insulating material is ε_i then radiation heat loss will occur from T_b to ambient temperature T_a as:

$$Q_r = \epsilon_i \times \sigma \times A_b \times (T_b^4 - T_a^4)$$

$$= \epsilon_i \times \sigma \times A_b \times (T_b^2 + T_a^2) \times (T_b + T_a) \times (T_b - T_a)$$

$$= h_r \times A_b \times (T_b - T_a)$$

$$[\text{here}, h_r = \epsilon_i \times \sigma \times (T_b^2 + T_a^2) \times (T_b + T_a)]$$

$$= (T_b - T_a)/R_r$$

Where,

$$R_r = \frac{1}{h_r \times A_b}$$

……………………….………. (5.8)

Finally, total insulation heat transfer resistance is,

$$R_t = R_c + R_r$$

………………………………... (5.9)

Total heat loss through the boundary wall would be,

$$Q_b = \frac{T_s - T_a}{R_t}$$

……………………………….. (5.10)

For the designed furnace, to minimize heat loss through the wall, the thickness of the insulation is assumed to be $X = 30$ mm $= 0.03$ m. With a 30 mm thick wall, excluding the aperture area, the boundary area becomes 0.35 m^2. In the experiments, the insulation used was calcium silicate. Considering the same material to make the insulation of the furnace, the heat conductivity as per the manufacturer's specification is 0.072 W/m.K, and the emissivity is 0.9. With the designed furnace and insulation material, the heat loss through the boundary wall with increasing system temperature can be calculated with eq. (5.10). Then total energy loss through the boundary wall can be calculated as-

$$E_b = \Delta t \times Q_b$$

……………………………….. (5.11)

Some energy will leave the system with the byproducts of the reaction- water vapor and hydrogen molecules. Energy leaving the system with water vapor will be calculated by multiplying the molar flow rate of water vapor with the specific enthalpy of water at system temperature, $\bar{h}$ H2O (T_s). Energy leaving the system with hydrogen will be calculated similarly, considering the molar flow rate and specific enthalpy of hydrogen. The energy loss with produced water and excess hydrogen based on system temperature can be calculated with eq. (5.12) and eq. (5.13) for 1 kg of LHS-1.

$$E_{H_2O} = n_{H_2O} \times \bar{h}_{H_2O}(T_s)$$

…………………………………..(5.12)

$$E_{H_2,out} = n_{H_2,out} \times \bar{h}_{H_2}(T_s)$$

………………………………… (5.13)
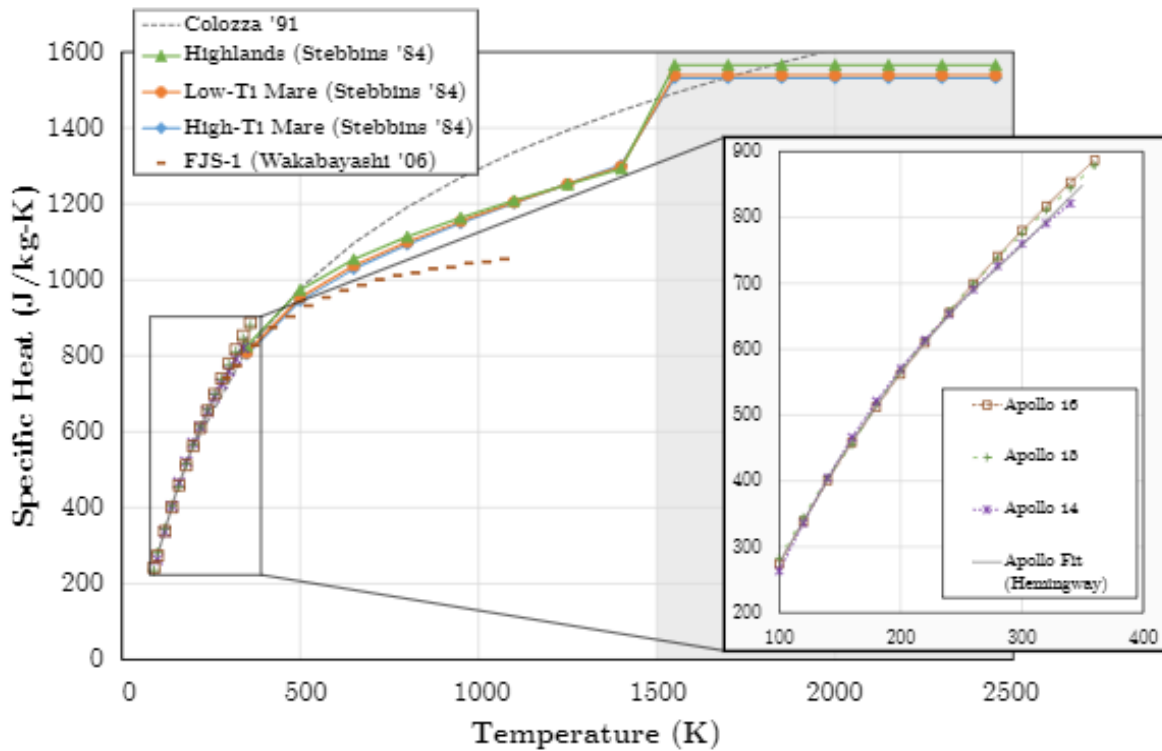
Figure 5.8. Specific heat with temperature for different lunar soil simulant [75]

After the reaction some energy will leave the system with sintered lunar soil simulant, E_{SLS}. The energy leaving the system with the sintered lunar soil simulant can be calculated with the specific heat of the lunar soil simulant and temperature gain. In Fig. 5.8, specific heat for different lunar soil simulants is plotted over the temperature in Kelvin. By converting the plot over the temperature in degrees Celsius, energy going out with sintered lunar soil simulant can be calculated. The amount of energy leaving the system with the sintered lunar soil simulant can be found by multiplying the mass of sintered lunar soil simulant by the specific heat of lunar soil simulant and the temperature rise from T_a to T_s. Fig. 5.9 presents the energy going out with 1 kg sintered LHS-1 at different system temperatures calculated with eq. (5.14).

$$E_{SLS} = M \times C_p \times \Delta T$$
………………………………….. (5.14)
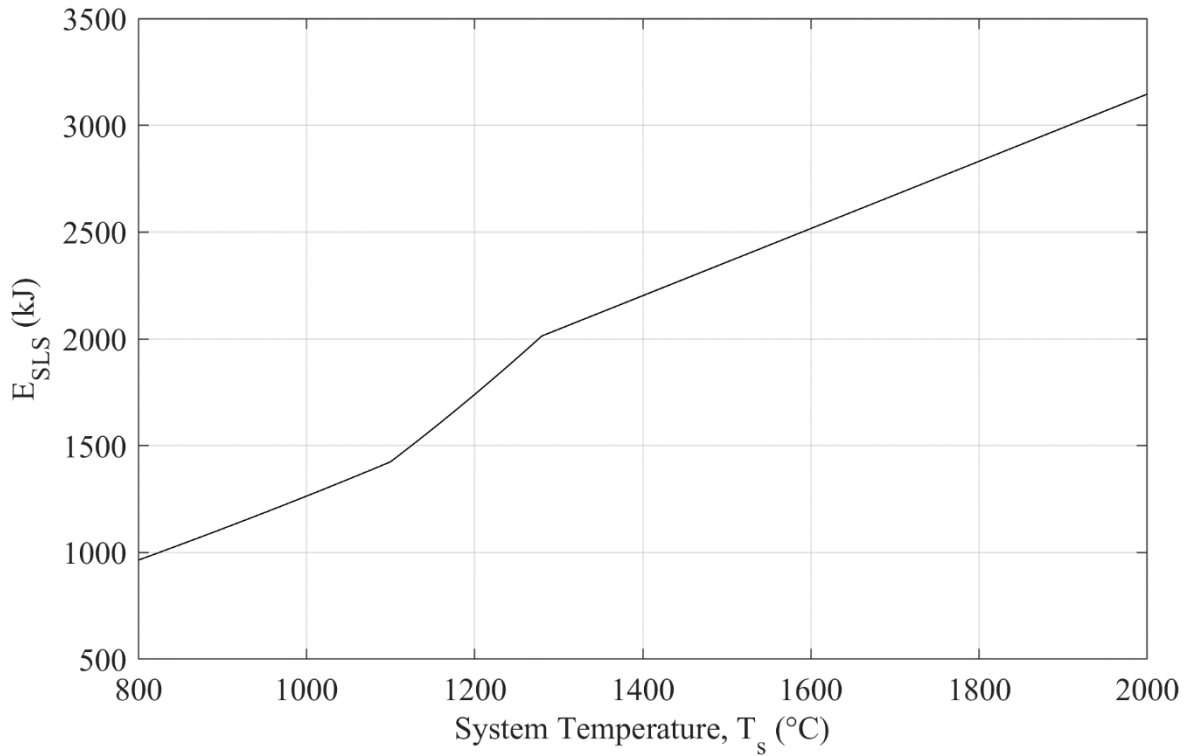
Figure 5.9. Energy going out with sintered lunar soil simulant, E_SLS

Considering all the known energy input and output, the required solar energy can be calculated. The input solar energy will depend on the concentration ratio. Again, if the concentration ratio increases, the aperture area will be reduced to keep the incoming solar energy the same to keep the system temperature constant. From the energy balance equation, the aperture area for different concentration ratios can be calculated for varying system temperatures. Based on the solar concentrator's concentration ratio, the aperture area will vary to achieve a specific temperature.

Therefore,

$$E_{solar} - E_{rerad} = E_b + E_{H_2O} + E_{H_2,out} + E_{SLS} - E_{LS} - E_{H_2,in} - E_{react}$$

Or,

$$\Delta t \times Q_{solar} - \Delta t \times Q_{rerad} = \Delta t \times Q_b + E_{H_2O} + E_{H_2,out} + E_{SLS} - E_{LS} - E_{H_2,in} - E_{react}$$

Or,

$$\Delta t \times I \times C \times A_{ap} - \Delta t \times \sigma \times A_{ap} \times (T_s^4 - T_a^4)$$

$$= \Delta t \times Q_b + E_{H_2O} + E_{H_2,out} + E_{SLS} - E_{LS} - E_{H_2,in} - E_{react}$$

Or,

$$A_{ap} = \frac{(\Delta t \times Q_b) + E_{H_2O} + E_{H_2,out} + E_{SLS} - E_{LS} - E_{H_2,in} - E_{react}}{\Delta t \times ((I \times C) - \sigma \times (T_s^4 - T_a^4))}$$

$$\text{...(5.15)}$$

From section 5.1, it is seen that, after 10 minutes, water production reduces. Experiments prove that about 10 minutes is an excellent time to finish an experiment to minimize energy loss. Therefore, considering $\Delta t = 10$ min, aperture area can be calculated with different concentration ratios with eq. (5.15), which can be used to calculate the incoming solar energy and energy loss through reradiation from the system for varying system temperatures.
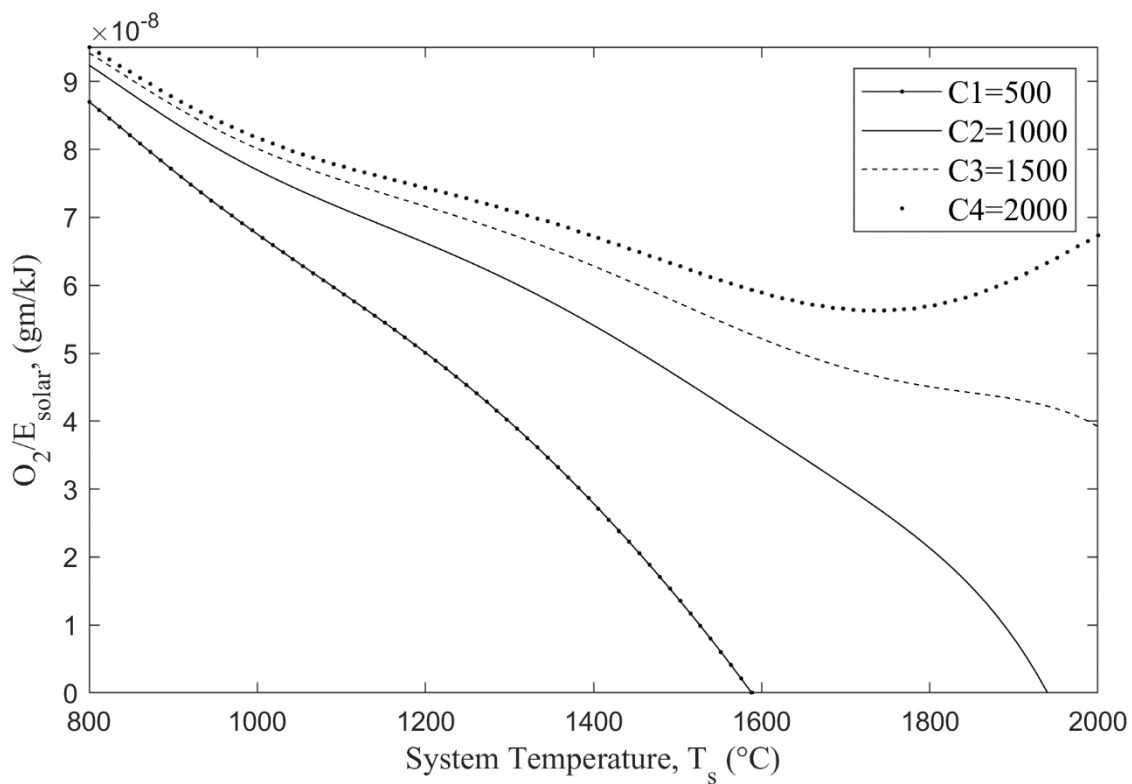
Figure 5.10. The ratio of reradiated energy loss to incoming solar energy with system temperature

Taking $\xi = 4$, the energy of solar irradiation and energy loss through solar reradiation is calculated. Fig. 5.10 presents the oxygen production per kilojoule of incoming solar energy with system temperature. The plot represents that, with an increased concentration ratio and reduced aperture area, oxygen production is higher for higher system temperature, but the production rate gradually decreases and goes to zero after all the ilmenite reacts. There is still more work need to be done with this framework of thermodynamic analysis, but it is not within the scope of this thesis.

CHAPTER 6

CONCLUSION AND FUTURE WORK

6.1. Conclusion

Sintering of lunar soil simulant with sunlight represents an energy-efficient method to utilize resources present on the moon for infrastructure. It was determined that a range of steady-state temperatures, from approximately 850 to 1150°C, corresponding to a peak heat flux of 105-120 kW/m^2, will lead to sintering for concentrated sunlight. Directly irradiated samples showed an expected increase in sintering depth and mass with increased concentration irradiation radiation. A maximum thickness of 4 mm was achieved by direct sintering even with long times at a steady state. A higher heat flux of up to 225.6 kW/m^2 has been experimented with, which melts the top surface of the simulant, but an 8 mm thick simulant brick is sintered. This value represents the upper limit of the achievable depth of the solar-sintered lunar soil simulant. Due to concentrated irradiation, the volume of sintered lunar brick was not significant. Different sintering techniques are used to increase the volume and cross-section area. Layer-by-layer sintering is one promising method to sinter large lunar soil simulant brick. Experiments with the cavity also increased the sintered mass by trapping the reradiate heat, which takes the central thickness over 8 mm for 200 kW/m^2. The mass increased by 1.2 gm from 2.5 gm at this heat flux by using the cavity. Distributing the concentrated flux over a more significant top surface area provides even greater sintered material. Though melted, the achieved central thickness is 10.76 mm for 200 kW/m^2 heat flux with 8 gm sintered/melted material. A combination of cavity and irradiation distribution gives over 9 mm thickness at only 146 kW/m^2 heat flux.

Sintering depends on time. The time series experiment showed the comparative sintering behavior of LHS-1 and JSC-1A lunar soil simulant. It offers an increment of size of the sintered piece with time, where the length and width of sintered JSC-1A are always greater

than LHS-1 for a particular heating configuration. One exciting thing is the central thickness for JSC-1A is initially higher, but with time, the central thickness of LHS-1 surpasses the central thickness of JSC-1A. An extended set of experiments proved the finding in Fig. 3.44. The reasons noticed were the concave top surface for JSC-1A and the convex top surface for LHS-1 due to balling at higher heat flux. Table 3.44 shows the evolution of directly sintered samples with LHS-1 and JSC-1A with increasing heat flux.

Indirect sintering, achieved by transferring the heat by conduction through silicon carbide (SiC), a highly conductive material, leads to slightly thicker sintered but unmelted layers of 5 mm. It also allows for much larger areas to be sintered from a point source of concentrated sunlight. Maximum achieved central thickness is again 8 mm. Indirect sintering through a thin, highly conductive material may be a viable route to addressing several limitations of direct solar sintering. The indirect method sinters significantly less lunar soil simulant for the same incoming irradiation as direct sintering. Therefore, the drawback is to sinter a large lunar brick, higher incoming irradiation requires. Special indirect sintering experiments were conducted to reach the sintering temperature faster with higher incoming irradiation, which reduces processing time. This method resulted in similar final products to the constant current method at a similar steady-state temperature. Finally, compressive strength was measured for several samples, reaching values between 20 to 30 MPa, relatively higher than terrestrial high-strength concrete. Initial results indicate that indirectly sintered samples are stronger than directly sintered samples, though more data must be collected to confirm these trends.

Finally, thermodynamic analysis is conducted for a closed system to sinter lunar soil simulant and extract byproduct water for oxygen production. The study shows that 0.26 gm of water can be produced from 1 kg of LHS-1 lunar soil simulant, with a hydrogen mole to oxygen moles ratio of 4 at 2000°C. Through electrolysis, 0.23 gm of oxygen can be separated from

produced water. This temperature is much higher than the melting temperature of the experiment. So experimentally this amount of water production is not achievable in the conducted experiments. The highest experimental temperature was achieved just below 1400°C and only 0.1 gm of water can be extracted at that temperature from 1 kg of LHS-1 lunar soil simulant for $\xi = 4$. The thermodynamic analysis calculates the total input and output energy and required solar energy to gain the operational temperature of the system, considering all the heat flow.

6.2. Future Work

The current study introduces different dimensions of concentrated solar sintering of lunar soil simulant. Each experimental research requires further investigation to improve the techniques and establish the findings. For example, indirect sintering can be conducted with distributed irradiation and cavity. In addition, time series experiments and experiments with different lunar soil simulants can be conducted with indirect sintering to learn the prospect of indirect sintering for widespread use. Similarly, special experiments to reach the sintering temperature faster can be used for direct sintering experiments. There are also scopes to improve the thermodynamic analysis by finding water production with time for different hydrogen-to-oxygen ratios at different temperatures. At last, a sintering furnace can be developed to run experiments inside the furnace to taste the feasibility of solar sintering of lunar soil simulant in the lunar atmosphere.

BIBLIOGRAPHY

[1]   A. G. W. Cameron, "From interstellar gas to the Earth-Moon system," Meteorifics & Planetary Science, vol. 36, pp. 9–22, 2001.

[2]   R. M. Canup, "Simulations of a late lunar-forming impact," vol. 168, pp. 433–456, 2004, doi: 10.1016/j.icarus.2003.09.028.

[3]   J. Zhang, N. Dauphas, A. M. Davis, I. Leya, and A. Fedkin, "The proto-Earth as a significant source of lunar material," Nat Geosci, vol. 5, no. April, pp. 251–255, 2012, doi: 10.1038/ngeo1429.

[4]   X. Zhang et al., "Spark plasma sintering of a lunar regolith simulant: effects of parameters on microstructure evolution, phase transformation, and mechanical properties," Ceramics International, vol. 47, no. 4. pp. 5209–5220, 2021. doi: 10.1016/j.ceramint.2020.10.100.

[5]   H. Benaroya, P. Metzger, and A. Muscatello, "Special Issue on In Situ Resource Utilization," J Aerosp Eng, vol. 26, no. 1, pp. 1–4, Jan. 2013, doi: 10.1061/(asce)as.1943-5525.0000282.

[6]   A. Meurisse, A. Makaya, C. Willsch, and M. Sperl, "Solar 3D printing of lunar regolith," Acta Astronaut, vol. 152, pp. 800–810, Nov. 2018, doi: 10.1016/j.actaastro.2018.06.063.

[7]   B. Imhof et al., "Advancing Solar Sintering for Building A Base On The Moon FP6-VIEW-FINDER View project Powder-based 3D Printing in Microgravity View project Advancing Solar Sintering for Building A Base On The Moon," 2017.

[8]   A. Goulas and R. J. Friel, "3D printing with moondust," Rapid Prototyp J, vol. 22, no. 6, pp. 864–870, 2016, doi: 10.1108/RPJ-02-2015-0022.

[9]   L. Thiébaut and A. Cowley, "Microwave processing of regolith - a 1D-printing cavity for enabling lunar construction technology," in 8th European Conference for Aeronautics And Space Sciences (EUCASS), 2019, p. 13. doi: 10.13009/EUCASS2019-917.

[10]   V. Srivastava, S. Lim, and M. Anand, "Microwave processing of lunar soil for supporting longer-term surface exploration on the Moon," Space Policy, vol. 37, pp. 92–96, Aug. 2016, doi: 10.1016/j.spacepol.2016.07.005.

[11]   M. Reichert, S. Lingner, W. Seboldt, S. Systems, and A. Division, "e r g a m o n".

[12]   A. Liu, Z. Shi, X. Hu, B. Gao, and Z. Wang, "Lunar Soil Simulant Electrolysis Using Inert Anode for Al-Si Alloy and Oxygen Production," J Electrochem Soc, vol. 164, no. 2, pp. H126–H133, 2017, doi: 10.1149/2.1381702jes.

[13]   K. Xie, Z. Shi, J. Xu, X. Hu, B. Gao, and Z. Wang, "Aluminothermic Reduction-Molten Salt Electrolysis Using Inert Anode for Oxygen and Al-Base Alloy Extraction from Lunar Soil Simulant," JOM, vol. 69, no. 10, pp. 1963–1969, 2017, doi: 10.1007/s11837-017-2478-4.

[14]   T. Denk, A. González-Pardo, I. Cañadas, and A. Vidal, "Design and test of a concentrated solar powered fluidized bed reactor for ilmenite reduction," SolarPACES, vol. 2, no. 2, pp. 1–8, 2017.

[15]   J. G. Chambers, L. A. Taylor, A. Patchen, and D. S. Mckay, "Quantitative mineralogical characterization of lunar high-Ti mare basalts and soils for oxygen production," 1995.

[16]   C. C. Allen, R. V Morris, and D. S. Mckay, "Oxygen extraction from lunar soils and pyroclastic glass," 1996.

[17]   K. A. Lee, L. Oryshchyn, A. Paz, M. Reddington, and T. M. Simon, "The roxygen project: Outpost-scale lunar oxygen production system development at Johnson Space Center," J Aerosp Eng, vol. 26, no. 1, pp. 67–73, 2013, doi: 10.1061/(ASCE)AS.1943-5525.0000230.

[18]   C. Schwandt, J. A. Hamilton, D. J. Fray, and I. A. Crawford, "The production of oxygen and metal from lunar regolith," in Planetary and Space Science, 2012, vol. 74, no. 1, pp. 49–56. doi: 10.1016/j.pss.2012.06.011.

[19]   M. McLean, "Encyclopedia of materials science and technology," International Metals Reviews, vol. 31, no. 1, pp. 289–290, 1986, doi: 10.1179/imtr.1986.31.1.289.

[20]   R. German, Sintering: From Empirical Observations to Scientific Principles. 2014. doi: 10.1016/C2012-0-00717-X.

[21]   R. M. German, "Fundamentals of sintering," ASM International, Engineered Materials Handbook, vol. 4, pp. 260–269, 1991.

[22]   H. E. Exner and E. Arzt, "Sintering Processes," in Sintering Key Papers, 1990, pp. 157–184. doi: 10.1007/978-94-009-0741-6_10.

[23]   M. B. Shongwe, S. Diouf, M. O. Durowoju, and P. A. Olubambi, "Effect of sintering temperature on the microstructure and mechanical properties of Fe-30%Ni alloys produced by spark plasma sintering," J Alloys Compd, vol. 649, pp. 824–832, 2015, doi: 10.1016/j.jallcom.2015.07.223.

[24]   S. K. Kumpaty, D. Cottrill, A. Hollett, J. Barrett, and S. Kamara, "An Experimental Study of Heat Transfer in Selective Laser Sintering TM process," in 9th International Conference on Engineering Education, 2006, pp. 5–9.

[25]   B. Xiao and Y. Zhang, "Advances in Thermal Modeling of Selective Laser Sintering of Single-Component Metal Powders," in 6th International Symposium on Multiphase Flow, Heat Mass Transfer and Energy Conversion, 2009, no. July, pp. 11–15.

[26]   T. Chen and Y. Zhang, "Two-dimensional modeling of sintering of a powder layer on top of nonporous substrate," Frontiers of Mechanical Engineering in China, vol. 5, no. 2, pp. 143–148, 2010, doi: 10.1007/s11465-010-0006-0.

[27]   K. I. Rybakov, E. A. Olevsky, and E. V Krikun, "Microwave sintering: Fundamentals and modeling," Journal of the American Ceramic Society, vol. 96, no. 4, pp. 1003–1020, 2013, doi: 10.1111/jace.12278.

[28]   S. D. Luo, M. Qian, and M. Ashraf Imam, "Microwave sintering of titanium and titanium alloys," in Titanium Powder Metallurgy: Science, Technology and Applications, 2015, pp. 237–251. doi: 10.1016/B978-0-12-800054-0.00014-9.

[29]   S. N. A. Shahbudin, M. H. Othman, S. Y. M. Amin, and M. H. I. Ibrahim, "A Review of Metal Injection Molding- Process, Optimization, Defects and Microwave Sintering on WC-Co Cemented Carbide," IOP Conf Ser Mater Sci Eng, vol. 226, no. 1, 2017, doi: 10.1088/1757-899X/226/1/012162.

[30]   P. Pachauri and M. Hamiuddin, "Effect of Sintering Process Parameters in Metal Injection Molding (MIM) Process on Impact Toughness of Sintered Parts," International Journal of Advanced Materials and Metallurgical Engineering (IJAMME), vol. 2, no. 1, pp. 23–33, 2016.

[31]   R. R. Rieber and M. A. Seibert, "Two Problems, One Solution – Microwave Sintering of Lunar Dust," in Joint Annual Meeting of LEAG-ICEUM-SRR, 2008.

[32]   S. Allan, J. Braunstein, I. Baranova, N. Vandervoort, M. Fall, and H. Shulman, "Computational modeling and experimental microwave processing of JSC-1A lunar simulant," J Aerosp Eng, vol. 26, no. 1, pp. 143–151, 2013, doi: 10.1061/(ASCE)AS.1943-5525.0000245.

[33]   X. Zhang et al., "Microstructure evolution during spark plasma sintering of FJS-1 lunar soil simulant," Journal of the American Ceramic Society, vol. 103, no. 2, pp. 899–911, Feb. 2020, doi: 10.1111/jace.16808.

[34]   L. A. Taylor and T. T. Meek, "Microwave sintering of lunar soil: Properties, theory, and practice," J Aerosp Eng, vol. 18, no. 3, pp. 188–196, 2005, doi: 10.1061/(ASCE)0893-1321(2005)18:3(188).

[35]   O. Guillon et al., "Field-assisted sintering technology/spark plasma sintering: Mechanisms, materials, and technology developments," Advanced Engineering Materials, vol. 16, no. 7. Wiley-VCH Verlag, pp. 830–849, 2014. doi: 10.1002/adem.201300409.

[36]   A. Ragulya, "Fundamentals of Spark Plasma Sintering," in Reference Module in Materials Science and Materials Engineering, 2016, pp. 1–6. doi: 10.1016/b978-0-12-803581-8.03654-7.

[37]   J. Wu, F. Chen, Q. Shen, J. M. Schoenung, and L. Zhang, "Spark plasma sintering and densification mechanisms of antimony-doped tin oxide nanoceramics," J Nanomater, vol. 2013, 2013, doi: 10.1155/2013/561895.

[38]   Z. H. Zhang, Z. F. Liu, J. F. Lu, X. B. Shen, F. C. Wang, and Y. D. Wang, "The sintering mechanism in spark plasma sintering - Proof of the occurrence of spark discharge," Scr Mater, vol. 81, pp. 56–59, 2014, doi: 10.1016/j.scriptamat.2014.03.011.

[39]   U. Anselmi-Tamburini, "Spark Plasma Sintering," in Reference Module in Materials Science and Materials Engineering, 2019. doi: 10.1016/b978-0-12-803581-8.11730-8.

[40]   M. B. Shongwe, S. Diouf, M. O. Durowoju, and P. A. Olubambi, "Effect of sintering temperature on the microstructure and mechanical properties of Fe-30%Ni alloys produced by spark plasma sintering," J Alloys Compd, vol. 649, pp. 824–832, Aug. 2015, doi: 10.1016/j.jallcom.2015.07.223.

[41]   O. O. Ayodele, M. B. Shongwe, P. A. Olubambi, B. A. Obadele, and T. Langa, "Hybrid Spark Plasma Sintering of Materials: A Review," International Journal of Materials, Mechanics and Manufacturing, vol. 6, no. 6, pp. 360–364, 2018, doi: 10.18178/ijmmm.2018.6.6.407.

[42]   M. B. Shongwe, S. Diouf, M. O. Durowoju, P. A. Olubambi, M. M. Ramakokovhu, and B. A. Obadele, "A comparative study of spark plasma sintering and hybrid spark plasma sintering of 93W-4.9Ni-2.1Fe heavy alloy," Int J Refract Metals Hard Mater, vol. 55, pp. 16–23, 2016, doi: 10.1016/j.ijrmhm.2015.11.001.

[43]   T. P. Mishra et al., "Field-assisted sintering/spark plasma sintering of gadolinium-doped ceria with controlled re-oxidation for crack prevention," Materials, vol. 13, no. 14, Jul. 2020, doi: 10.3390/ma13143184.

[44]   A. E. Jakus, K. D. Koube, N. R. Geisendorfer, and R. N. Shah, "Robust and Elastic Lunar and Martian Structures from 3D-Printed Regolith Inks," Sci Rep, vol. 7, 2017, doi: 10.1038/srep44931.

[45]   S. L. Taylor et al., "Sintering of micro-trusses created by extrusion-3D-printing of lunar regolith inks," Acta Astronaut, vol. 143, pp. 1–8, 2018, doi: 10.1016/j.actaastro.2017.11.005.

[46]   M. Fateri et al., "Solar Sintering for Lunar Additive Manufacturing," J Aerosp Eng, vol. 32, no. 6, p. 04019101, 2019, doi: 10.1061/(asce)as.1943-5525.0001093.

[47]   D. A. Urbina et al., "Robotic prototypes for the solar sintering of regolith on the lunar surface developed within the Regolight project," Proceedings of the International Astronautical Congress, IAC, vol. 4, no. November, pp. 2632–2641, 2017.

[48]   P. E. Hintze, "Space Manufacturing 14: Critical Technologies for Space Settlement-Space Studies Institute Building a Vertical Take Off and Landing Pad Using in situ Materials," 2010.

[49]   T. Nakamura and B. K. Smith, "Solar Thermal Power System for Lunar ISRU Applications: Result of ISRU Analog Test, Mauna Kea, HI," 2010. doi: https://doi.org/10.2514/6.2010-8902.

[50]   NASA technical report, "NASA's Lunar Exploration Program Overview," Nasa, no. September, p. 74, 2020.

[51]   Exolith Lab, "LHS-1 Lunar Highlands Simulant - Fact Sheet - 2021," 2021.

[52]   D. S. McKay, J. L. Carter, W. W. Boles, C. C. Allen, and H. H. Allton, "New lunar soil simulant," Proceedings of the 4th International Conference on Engineering, Construction and Operations in Space, pp. 857–866, 1994.

[53]   C. S. Ray, S. T. Reis, S. Sen, and J. S. O'Dell, "JSC-1A lunar soil simulant: Characterization, glass formation, and selected glass properties," J Non Cryst Solids, vol. 356, no. 44–49, pp. 2369–2374, 2010, doi: 10.1016/j.jnoncrysol.2010.04.049.

[54]   L. A. Taylor, "Status of lunar regolith simulants - An update," Lunar Exploration Analysis Group, pp. 2012–2013, 2015.

[55]   S. Weyer, "68th Annual Meteoritical Society Meeting (2005)," vol. 68, p. 5102, 2005.

[56]   "Lunar Surface Science Workshop 17 2022 (LPI Contrib. No. 2241) 5013.pdf," vol. 2022, no. 2241, p. 5013, 2022.

[57]   S. W. Perkins and C. R. Madson, "Mechanical and Load-Settlement Characteristics of Two Lunar Soil Simulants," J Aerosp Eng, vol. 9, no. 1, pp. 1–9, 1996, doi: 10.1061/(asce)0893-1321(1996)9:1(1).

[58]   K. A. Alshibli and A. Hasan, "Strength Properties of JSC-1A Lunar Regolith Simulant," Journal of Geotechnical and Geoenvironmental Engineering, vol. 135, no. 5, pp. 673–679, 2009, doi: 10.1061/(asce)gt.1943-5606.0000068.

[59]   P. Easter, J. Long-Fox, Z. Landsman, A. Metke, and D. Britt, "Comparing the Effects of Mineralogy and Particle Size Distribution on the Angle of Repose for Lunar Regolith Simulants," 53rd Lunar and Planetary Science Conference, vol. 2678, no. April, p. 1980, 2022.

[60]   C. I. Calle and C. R. Buhler, "Measurement of the Angle of Repose of Apollo 14 Lunar Sample 14163," Lunar Dust Workshop, vol. 2020, no. 2141, p. 5030, 2020.

[61]   T. Arai, K. Suzuki, R. Moriwaki, and T. Mtsui, "53rd Lunar and Planetary Science Conference (2022) 1289.pdf," 53rd Lunar and Planetary Science Conference (2022), p. 2930, 2022.

[62]   L. Sibille, P. Carpenter, R. Schlagheck, and R. French, "Lunar Regolith Simulant Materials: Recommendations for Standardization, Production, and Usage," NASA Technical Paper, no. September, p. 142, 2006.

[63]   D. Biswas, T. Cox, and J. L. Lapp, "Sintering Behavior of Lunar Soil Heated by Indirect and Direct Concentrated Sunlight." Jul. 11, 2022. doi: 10.1115/ES2022-81630.

[64]   S. A. Kalogirou, "Solar Thermal Power Systems," Solar Energy Engineering, pp. 541–581, Jan. 2014, doi: 10.1016/B978-0-12-397270-5.00010-8.

[65]   A. Goulas, R. A. Harris, and R. J. Friel, "Additive manufacturing of physical assets by using ceramic multicomponent extra-terrestrial materials," Addit Manuf, vol. 10, pp. 36–42, Apr. 2016, doi: 10.1016/j.addma.2016.02.002.

[66]   D. Gu and Y. Shen, "Balling phenomena during direct laser sintering of multi-component Cu-based metal powder," J Alloys Compd, vol. 432, no. 1–2, pp. 163–166, 2007, doi: 10.1016/j.jallcom.2006.06.011.

[67]   L. M. Anovitz et al., "The heat-capacity of ilmenite and phase equilibria in the system Fe-T-O," Geochim Cosmochim Acta, vol. 49, no. 10, pp. 2027–2040, 1985, doi: 10.1016/0016-7037(85)90061-4.

[68]   P. Kania, M. Hermanns, S. Brünken, H. S. P. Müller, and T. F. Giesen, "Millimeter-wave spectroscopy of titanium dioxide, TiO2," J Mol Spectrosc, vol. 268, no. 1–2, pp. 173–176, Jul. 2011, doi: 10.1016/j.jms.2011.04.013.

[69]   H. Sato et al., "Sixteen Thousand Evaluated Experimental Thermodynamic Property Data for Water and Steam," J Phys Chem Ref Data, vol. 20, no. 5, pp. 1023–1044, Sep. 1991, doi: 10.1063/1.555894.

[70]   Y. Lu, D. Mantha, and R. G. Reddy, "Thermodynamic Analysis on Lunar Soil Reduced by Hydrogen", doi: 10.1007/s11663-010-9411-3.

[71]   H. Yoshida, T. Watanabe, H. Kanamori, T. Yoshida, S. Ogiwara, and K. Eguchi, "Experimental study on water production by hydrogen reduction of lunar soil simulant in a fixed bed reactor," Space Resources Roundtable Inc., Golden, CO, pp. 188–704, 2000.

[72]   J. Lapp, J. H. Davidson, and W. Lipi, "Efficiency of two-step solar thermochemical non-stoichiometric redox cycles with heat recovery," 2011, doi: 10.1016/j.energy.2011.10.045.

[73]   T. Hettesheimer, S. Hirzel, and H. B. Roß, "Energy savings through additive manufacturing: an analysis of selective laser sintering for automotive and aircraft components," Energy Effic, vol. 11, no. 5, pp. 1227–1245, 2018, doi: 10.1007/s12053-018-9620-1.

[74]   X. Li et al., "Condition of solar radiation on the moon," Moon: Prospective Energy and Material Resources, vol. 9783642279, pp. 347–365, 2012, doi: 10.1007/978-3-642-27969-0_15.

[75]   S. S. Schreiner, J. A. Dominguez, L. Sibille, and J. A. Hoffman, "Thermophysical property models for lunar regolith," Advances in Space Research, vol. 57, no. 5, pp. 1209–1222, 2016, doi: 10.1016/j.asr.2015.12.035.

APPENDIX A: DIRECT SINTERING

Table A.1. Preliminary direct sintering time data set

Distance (mm)	Experiment Duration (min)	Sintering Start Time (min)	Melting Start Time (min)	Steady State Time (min)
173	20:11.1			20:11.1
160	22:22.7			22:22.7
150	33:50.5			33:50.5
140	23:00.4			23:00.4
130	35:00.3	02:29.3		35:00.3
120	32:15.8	03:04.6		32:15.8
110	39:53.3	02:51.7		39:53.3
100	30:32.3	01:41.1		30:32.3
90	30:12.2	01:19.5		30:12.2
80	30:16.2	01:29.9	02:33.3	30:16.2
70	36:04.5	01:17.8	02:42.1	36:04.5
60	33:01.5	00:55.4	02:18.8	33:01.5
50	31:40.5	01:33.1	03:41.5	31:40.5

Table A.2. Preliminary direct sintering temperature data set

Distance (mm)	Maximum Top Thermocouple Temperature (°C)	Max. Middle Thermocouple Temperature (°C)	Max. Bottom Thermocouple Temperature (°C)	Steady State Temp of Top Thermocouple(°C)
173	736.24	532.56	422.61	736.24
160	721.19	517.58	434.79	721.19
150	794.70	571.86	463.45	794.70
140	795.28	579.79	468.77	795.28
130	868.01	631.63	513.62	868.01
120	924.63	655.84	531.10	924.63
110	1027.56	729.00	562.47	1027.56
100	989.01	729.44	554.97	989.01
90	1085.06	781.70	600.61	1085.06
80	1155.055	893.64	660.60	1155.05
70	1202.148	972.49	696.22	1202.14
60	1193.72	1096.46	708.22	1193.72
50	1260.32	1150.91	657.83	1260.32

Table A.3. Experimental verification time data set with varying focus for direct sintering experiments

Height (mm)	Time (min)	Time (min)	Time (min)	Time (min)
160	36:06.9			30
155	40:00.5			30
150	40:00.5			30
145	35:14.8			30
140	45:09.5			40
135	40:00.5	4:00.0		35
130	50:00.8	4:00.0		45
125	40:01.3	3:30.3		34
120	38:00.1	3:00.6		32
115	50:13.6	2:00.4		44
110	50:01.6	2:00.4		47
105	53:08.6	2:00.4		49
100	52:53.4	2:00.4		51
95	54:03.2	1:20.3		34
90	50:32.1	1:10.6	4:00.0	45
85	54:22.4	1:00.2	4:00.0	29
80	53:02.2	1:00.2	4:00.0	42
75	52:48.5	0:45.7	3:30.3	38
70	53:43.9	0:45.7	3:30.3	40

Table A.4. Experimental verification temperature data set with varying focus for direct sintering experiments

Height (mm)	Top Thermocouple Temp (°C)	Middle Thermocouple Temp (°C)	Bottom Thermocouple Temp (°C)	Sintering Temp (°C)	Melting Temp (°C)	Steady State Temp (°C)
160	750.70	614.71	470.23			750
155	786.89	638.59	488.20			780
150	816.15	663.50	464.43			810
145	831.20	627.52	497.36			830
140	838.66	689.20	513.31			838
135	861.20	697.34	503.29	732.88		860
130	892.42	778.15	644.85	710.35		890
125	900.96	707.06	524.54	685.80		900
120	924.87	801.84	642.21	699.91		920
115	933.26	792.78	643.77	624.58		930
110	985.02	821.73	646.55	660.60		984
105	1064.04	864.97	701.58	742.14		1062
100	1078.14	814.59	571.25	795.54		1075
95	1100.41	944.95	739.87	814.12		1095
90	1122.55	815.44	607.54	571.76	914.84	1120
85	1157.12	676.96	529.97	743.15	1096.33	1150
80	1198.01	986.81	757.50	579.34	947.61	1195
75	1201.91	1002.61	772.93	523.67	919.66	1200
70	1239.96	781.45	624.85	435.23	878.13	1235

Table A.5. Top surface temperature of LHS-1 under direct sintering during experimental verification

Time	100mm	95mm	90mm	85mm	80mm	75mm	70mm
0	23.48	23.90	22.74	25.06	24.82	29.66	27.19
2	1056	985	1125	1135.5	1142	1156.8	1222.8
4	1134	1067	1183	1185.5	1223	1181.1	1253.4
6	1132	1195	1155.5	1194.3	1222	1170	1251.3
8	1139	1197	1181.4	1191.9	1189	1197.3	1204.5
10	1156	1189	1170	1162.3	1197	1227.4	1233
15	1111	1191	1198.3	1199.7	1200	1165.9	1235
20	1157	1175	1199.6	1202	1205	1108.9	1234
25	1113	1179	1200.1	1208.6	1208	1208.7	1235
30	1153	1176	1204.6	1213.7	1178	1211.1	1217
35	1184	1185	1189.3	1198.1	1202	1174.6	1220
40	1116	1189.8	1191.5	1200.3	1226	1209.3	1219

Table A.6. Conversion of distance to heat flux using SiC plate during direct sintering with fixed focus at focal point

Distance (mm)	SiC Temperature (°C)	SiC Temperature (K)	Emissivity of SiC	Constant W/m^2K^4	Flux (W/m^2)	Flux (kW/m^2)
90	863	1136	0.9	5.67×10^{-8}	84984.33	85.0
85	898	1171	0.9	5.67×10^{-8}	95951.80	96.0
80	927	1200	0.9	5.67×10^{-8}	105815.81	105.8
75	948	1221	0.9	5.67×10^{-8}	113419.63	113.4
70	988	1261	0.9	5.67×10^{-8}	129028.58	129.0
65	1039	1312	0.9	5.67×10^{-8}	151203.17	151.2
60	1055	1328	0.9	5.67×10^{-8}	158714.96	158.7
55	1111	1384	0.9	5.67×10^{-8}	187227.63	187.2
50	1177	1450	0.9	5.67×10^{-8}	225578.43	225.6

Table A.7. Experimental data with concentrated irradiation fixed at 50 mm distance with 60 A input current

Distance (mm)	Flux (kW/m^2)	Top Surface Temp (°C)	Steady State Temp (°C)	Sintered Mass (gm)	Central Thickness (mm)
90	85	861.8	830	0	0
85	96	1008.3	900	0	0
80	105.8	1121.6	915	0.01	1.74
77.5	109.6	1170	990	0.05	1.91
75	113.4	1220	1045	0.3	2.4
72.5	121.2	1229	1109	0.4	2.7
70	129	1237	1166	0.6	4.06
65	151.2	1251.5	1240	0.9	4.56
60	158.7	1362.3	1270	1.2	6.5
55	187.2	1379.6	1340	1.4	7.4
50	225.6	1390.4	1325	1.9	7.82

Table A.8. Experimental data without and with cavity for 178.5 kW/m^2 heat flux

Trial	Without Cavity			With Cavity		
	Mass (gm)	Thickness (mm)	Maximum Dimension (mm×mm)	Mass (gm)	Thickness (mm)	Maximum Dimension (mm×mm)
1	1.5	5.97	16.65×15.85	2.5	6.81	20.00×17.34
2	1.5	6.31	15.80×17.25	2.5	7.25	16.31×20.26
3	1.6	5.76	18.00×16.50	2.5	6.91	18.69×20.66
Avg.	1.5	6.01		2.5	6.99	

Table A.9. Experimental data without and with cavity for 197.2 kW/m² heat flux

	Without Cavity			With Cavity		
Trial	Mass (gm)	Thickness (mm)	Maximum Dimension (mm×mm)	Mass (gm)	Thickness (mm)	Maximum Dimension (mm×mm)
1	2.6	7.32	19.76×18.62	3.7	8.54	20.25×20.94
2	2.5	7.59	17.92×19.21	3.7	8.26	19.04×23.10
3	2.4	7.27	18.28×18.83	3.7	8.70	22.07×20.58
Avg.	2.5	7.39		3.7	8.50	

Table A.10. Experimental data of distributed irradiation for 178.5 kW/m² heat flux

	Without Cavity		
Trial	Mass (gm)	Thickness (mm)	Maximum Dimension (mm×mm)
1	4.8	8.63	23.21×25.52
2	4.7	8.39	23.27×24.72
3	4.9	9.22	23.69×24.95
Average	4.8	8.75	

Table A.11. Time series experimental data of LHS-1 and JSC-1A sintered lunar bricks at 150 kW/m^2 heat flux

Time (min)	Mass (gm)		Thickness (mm)		Maximum Dimension (mm)			
	JSC-1A	LHS-1	JSC-1A	LHS-1	JSC-1A		LHS-1	
0	0	0	0	0	0	0	0	0
1	0.38	0.05	1.35	1.27	17.9	14.25	7.38	6.17
2	0.79	0.18	2.09	1.89	20.24	16.48	10.47	9.19
3	1.08	0.35	2.78	2.34	20.8	17.74	15.17	12.84
4	1.29	0.47	3.18	3.25	22.32	18.17	15.13	13.62
5	1.57	0.53	3.69	3.56	22.36	18.96	15.92	12.98
6	1.72	0.74	3.82	3.67	22.84	18.88	17.86	13.31
7	1.76	0.83	3.86	3.99	22.73	19.19	18.9	14.76
8	1.85	0.91	3.96	4.13	22.54	19.52	19.07	15.36
9	1.93	0.94	3.97	4.19	22.17	18.51	18.31	15.99
10	1.94	0.95	4.21	4.27	22.28	19.07	18.1	15.32
15	2.07	1.11	4.39	4.51	22.36	19.97	19.7	15.65
20	2.15	1.22	4.42	4.54	22.23	19.43	19.64	16.03
25	2.32	1.28	4.5	4.66	22.41	19.51	19.03	15.85

Table A.12. Time series experimental data of LHS-1 and JSC-1A sintered lunar bricks at 190 kW/m² heat flux

Time	Mass (gm)		Thickness (mm)		Maximum Dimension (mm)			
(min)	JSC-1A	LHS-1	JSC-1A	LHS-1	JSC-1A		LHS-1	
0	0	0	0	0	0	0	0	0
1	0.7	0.18	2.06	1.7	17.25	21.67	14.17	10.74
2	1.31	0.5	2.68	2.62	23.97	19.11	17.05	14.42
3	1.71	0.78	3.47	2.85	23.82	20.03	19.88	15.14
4	1.99	1.02	4.12	2.96	24.4	20.45	20.67	17.36
5	2.48	1.23	4.49	3.69	25.2	21.53	20.83	17.77
6	2.61	1.45	4.58	4.36	24.68	20.91	20.19	17.71
7	2.77	1.61	4.68	4.44	25.54	21.91	22.09	18.68
8	3.03	1.7	4.93	4.47	25.53	22.12	22.46	18.63
9	3.12	1.81	5.28	4.58	24.43	22.03	21.57	17.88
10	3.23	1.89	5.32	5	24.89	21.66	21.55	19.65
15	3.33	2.23	5.39	5.25	25.58	22.1	22.67	18.58
20	3.53	2.48	5.4	5.82	25.27	21.98	20.83	18.99
25	3.56	2.61	5.42	5.89	25.44	22.43	23.09	18.9
30	3.68	2.65	5.73	6.05	25.24	22.86	23.37	20.45

Table A.13. Experimental data for LHS-1, mixed (50% LHS-1 and 50% JSC-1A), and JSC-1A lunar soil simulant at 140 kW/m² heat flux

Simulant	JSC-1A		Mix		LHS-1	
Trial	Mass (gm)	Thickness (mm)	Mass (gm)	Thickness (mm)	Mass (gm)	Thickness (mm)
1	1.64	3.72	1.13	3.5	0.72	3.57
2	1.4	3.5	1.23	3.5	0.69	3.23
3	1.53	3.66	1.17	3.6	0.56	3.32
Average	1.523	3.63	1.177	3.53	0.657	3.37

Table A.14. Experimental data for LHS-1, mixed (50% LHS-1 and 50% JSC-1A), and JSC-1A lunar soil simulant at 160 kW/m² heat flux

Simulant	JSC-1A		Mix		LHS-1	
Trial	Mass (gm)	Thickness (mm)	Mass (gm)	Thickness (mm)	Mass (gm)	Thickness (mm)
1	2.48	4.27	1.76	4	1.32	4.42
2	2.56	4.46	1.69	4.2	1.43	4.21
3	2.23	4.16	1.94	4.3	1.37	3.96
Average	2.423	4.3	1.797	4.2	1.373	4.32

Table A.15. Experimental data for LHS-1, mixed (50% LHS-1 and 50% JSC-1A), and JSC-1A lunar soil simulant at 180 kW/m^2 heat flux

Simulant	JSC-1A		Mix		LHS-1	
Trial	Mass (gm)	Thickness (mm)	Mass (gm)	Thickness (mm)	Mass (gm)	Thickness (mm)
1	3.05	4.76	2.21	4.6	1.62	4.9
2	3.14	4.84	2.26	4.9	1.72	4.59
3	2.83	4.91	2.22	4.6	2	5.33
Average	3.007	4.84	2.23	4.7	1.78	4.94

Table A.16. Experimental data for LHS-1, mixed (50% LHS-1 and 50% JSC-1A), and JSC-1A lunar soil simulant at 200 kW/m^2 heat flux

Simulant	JSC-1A		Mix		LHS-1	
Trial	Mass (gm)	Thickness (mm)	Mass (gm)	Thickness (mm)	Mass (gm)	Thickness (mm)
1	5.05	5.86	4.02	6	3.67	6.7
2	4.95	6.3	3.39	5.4	3.42	5.99
3	5.03	5.99	3.47	5.8	3.08	6.16
Average	5.01	6.05	3.627	5.73	3.39	6.28

Table A.17. Comparison of sintered mass and central thickness with flux

Flux (kW/m²)	JSC-1A		Mix		LHS-1	
	Mass (gm)	Thickness (mm)	Mass (gm)	Thickness (mm)	Mass (gm)	Thickness (mm)
120	1.003	3.01	0.693	2.5	0.327	2.47
140	1.523	3.63	1.177	3.5	0.657	3.37
160	2.423	4.3	1.797	4.2	1.373	4.2
180	3.007	4.84	2.23	4.7	1.78	4.94
200	5.01	6.05	3.627	5.7	3.39	6.28

APPENDIX B: INDIRECT SINTERING

Table B.1. Experimental data of fixed focus indirect sintering experiments at 70 A current

Distance (mm)	Steady State Temperature of Top Thermocouple (°C)	Sintered Mass (gm)	Central Thickness (mm)
35	1087.03	0.4	2.05
30	1158.72	0.5	2.73
25	1099.41	0.9	3.33
20	1206.52	1.0	3.86
15	1244.36	1.3	4.12
10	1244.83	1.6	4.65
5	1255.27	1.9	4.95
0	1232.81	2.2	5.37

Table B.2. Experimental data of fixed focus indirect sintering experiments at 80 A current

Distance (mm)	Steady State Temperature of Top Thermocouple (°C)	Sintered Mass (gm)	Central Thickness (mm)
45	1133.79	0.7	2.40
40	1169.21	0.9	2.88
35	1184.03	1.1	3.26
30	1214.98	1.7	4.37
25	1233.10	2.0	5.04
20	1192.81	3.2	5.30
15	1277.26	3.0	5.38
10	1337.20	3.5	6.00
5	1369.99	3.7	7.48
0	1316.24	4.9	7.75

BIOGRAPHY OF THE AUTHOR

Diprajit Biswas was born in Gopalganj, Dhaka, Bangladesh on July 2, 1995. He was raised in Gopalganj and graduated from S. M. Model Govt. High School in April 2010 and from Govt. Bangabondhu College in May 2012. He attended Ahsanullah University of Science and Technology in Dhaka, Bangladesh, and graduated in 2018 with a Bachelor's degree in Mechanical Engineering. Of his passion for teaching, he joined Kakoli High School and College as an assistant teacher of physics and mathematics and taught one year there before joining the University of Maine in 2020. After receiving his Master's in Mechanical Engineering, Diprajit will join the University of Wisconsin-Madison for his Ph.D. in Mechanical Engineering to pursue his academic goal. Diprajit is a candidate for the Master of Science degree in Mechanical Engineering from the University of Maine in May 2023.